Fluid flow and thermal analysis in induced draft cooling towers

by

Prashanth Karupothula

A thesis submitted in partial fulfillment of the requirements for the degree of

Master of Science

Department of Mechanical Engineering

University of Alberta

Abstract

Cooling towers are heat rejection devices that utilize ambient air to cool hot water. The ambient air is drawn into the tower and brought into direct contact with hot water and where the heat and vapour get transferred. Fluid flow distribution in the tower can result in better thermal performance. However, the complex nature of airflow in the tower is often neglected in cooling tower analysis that has relied chiefly on simplified 1D models using semi-empirical equations. 2D numerical models were proposed, but these models use semi-empirical equations to simplify the evaporative process in the fill. A detailed analysis of the fluid flow in the tower and the effect of the fill on the fluid flow is studied. The current study is aimed at understanding the fluid flow distribution in the tower for different fill arrangements.

A numerical model developed in an in-house open-source software, namely Fuel Cell Simulation Toolbox (OpenFCST), is used to solve the Reynolds Averaged Navier-Stokes (RANS) equations with an algebraic turbulence model for closure. Simulations were performed considering the domain on a fill testing facility built in the ESDLab. The fluid flow distribution was obtained for an empty tower both in 2D and 3D. The obtained pressure drop in the empty cooling tower was compared against experimental data. Ansys software was utilized to estimate the fluid flow distribution with the $k - \epsilon$ turbulence model. The algebraic turbulence model shows a good agreement with the experimental data.

The fill in the tower is considered as a porous media using the Darcy-Forchheimer equation. The fill permeability value is estimated based on the available experimental data, which is then utilized to estimate the pressure drop in the tower. Parametric studies were performed

with different fill heights and locations to assess their effect on the fluid flow distribution in the tower. The obtained fluid flow distribution is utilized to estimate the heat and mass transfer distribution inside the cooling tower. The fill location in the tower does not affect the overall pressure drop in the tower.

The advection-diffusion equations were employed to solve for heat and mass distribution in the tower. Transfer coefficients estimated based on the test facility predict the temperature and mass fraction in the ESDLab cooling tower. The outlet air temperature and mass fraction increase with fill height and decrease with air flowrate in the ESDLab cooling tower.

The current numerical model is used to estimate the fluid flow and temperature and mass fraction distribution in an industrial-scale cooling tower and a cross-flow cooling tower. The industrial-scale cooling tower has similar observations as that of the ESDLab test facility, except the inlet effects are lower due to the tower's larger dimension.

Keywords: counterflow cooling tower, numerical model, fill, flow distribution, airflow

Preface

The data analysis in chapters 3, 4 and the concluding analysis in chapter 5 are my original work, as well as the literature review in chapter 1. The incompressible and compressible Navier-Stokes laminar fluid flow solvers were available in OpenFCST. With the assistance of Jarauta, implemented the algebraic turbulence model into OpenFCST. The computational domains and test cases discussed in this study were designed and implemented by myself.

Acknowledgements

I would like to thank my supervisor Dr. Marc Secanell for providing me with the opportunity to pursue research in numerical modelling of the cooling tower. He was accommodating in my transition to the new role and guided me in all the ways possible. It might not have been possible for me to complete this project without his enormous interest and support.

I would like to thank Dr. Alexandra Jarauta Arabi for helping me to use OpenFCST. He was always kind enough to find time to discuss issues and had the patience to listen to my specific problems.

I would like to thank Ms. Elizabeth Claire for providing me with her experimental data. She was always willing to help me to understand any concept related to cooling towers. The current numerical study is validated against her experimental data. Her contribution is invaluable to my project.

I would like to thank all my fellow graduate students who made my life at the University of Alberta memorable. You guys were always there to discuss both official and unofficial issues. Special thanks to Micheal and Aslan, as they helped design my presentation and writing style. I will never forget how you both tried to help me with my monthly reports and essential presentations.

I would like to thank ICT for financially supporting this project and for many fruitful discussions.

Lastly, I would like to thank my family. It has been a long journey, and it would not have been possible without your support.

Table of Contents

List of Tables

List of Figures

Chapter 1

Introduction

1.1 Motivation

Cooling towers are an integral component of many refrigeration systems, industrial plants, and other process plants, providing comfort or process cooling across a broad range of applications. They dissipate low-grade heat by bringing hot water in direct contact with the cold ambient air where both sensible and evaporative cooling occurs.

Cooling towers are large structures where air and water flow distribution depends on the cooling tower's geometry. Air is drawn at the bottom of the tower and exits at the top while it passes through the different zones in the tower, simultaneously interacting with hot water. The underlying physics in the tower, hence, depends mainly on the extent of water and air distribution in the tower, and it has been noted that the uniform distribution of both air and water leads to the good thermal performance of the tower [6].

Cooling towers have been an area of interest since the mid of 1950s; however, earlier models primarily relied on simplified one-dimensional models that did not account for fluid flow distribution. The fill-zone in these models is modelled with a semi-empirical equation, and the nature of the flow is not studied. Air enters the tower horizontally and changes direction to flow vertically up. This sudden change in direction results in a vena-contracta, a low-pressure region that might result in a recirculation zone along the inner tower wall. The presence of the recirculation zone leads to an uneven distribution of airflow across the tower cross-section, which is known to affect the tower performance [7]. Few recent models have considered a two-dimensional (2D) and three-dimensional (3D) numerical approach. However, they did not focus on fluid flow behaviour on the final performance of the tower. Moreover, the flow behaviour in the rain zone is affected by the fill characteristics [8, 9]. A quantitative approach with regards to a CFD model lacks in this aspect.

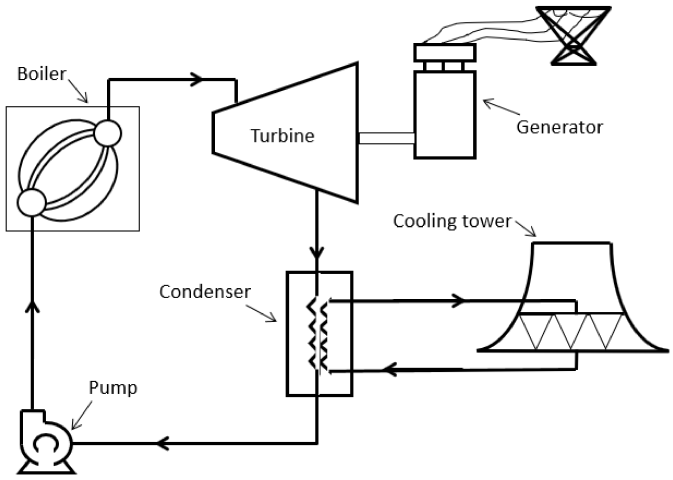

Figure 1.1 – Schematic of a steam power plant with a cooling tower. Remade based on the schematic in reference [1]

The main objective of this thesis is to analyze the fluid flow in the cooling tower using an in-house numerical software package. The aim is to understand the flow behaviour for different cooling tower geometries and fill configurations in the tower. The obtained fluid flow model is then coupled with heat and mass transfer equations to understand the transport dynamics in the tower.

1.2 Background

The main objective of a cooling tower is to provide a system with the necessary amount of cooling. Fig. 1.1 shows a simple schematic of a steam power plant, including a cooling tower where the cooling tower cools the water coming from the condenser. The condenser cools the process liquid using the cold water from the cooling tower. Based on the requirement, cooling tower structures vary greatly in size and design, but they all function to achieve the same objective: the liberation of waste heat extracted from a process or building system through evaporation. Cooling towers are engineered and designed based on the amount of heat that needs to be extracted from a given process. The cooling tower must be adequately sized to reject the required amount of heat into the atmosphere. Other aspects, such as atmospheric conditions and available sites, are considered to design a cooling tower.

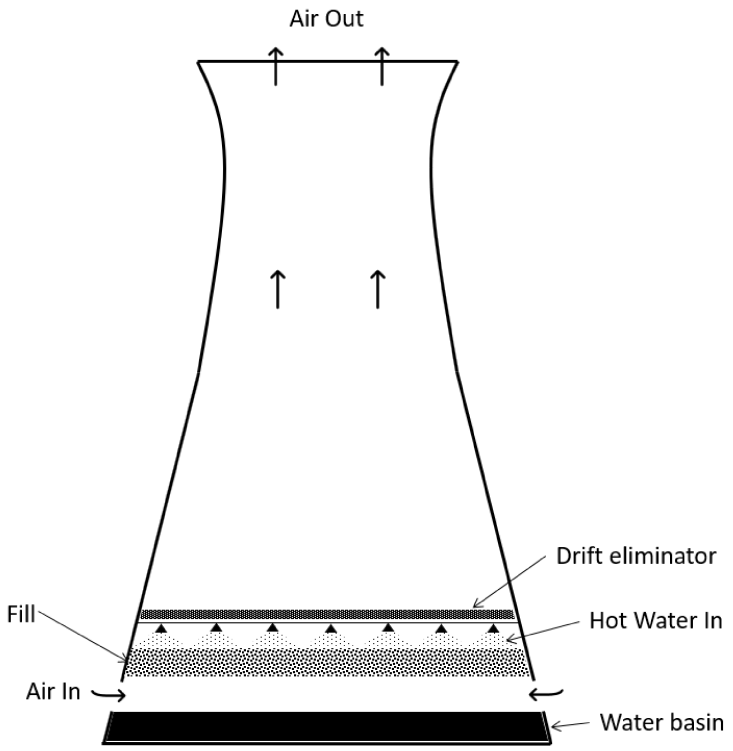

Figure 1.2 – Natural draft cooling tower. Remade based on the schematic in reference [2]

1.2.1 Types of cooling towers

Cooling towers are classified based on their heat transfer mechanism as dry cooling towers and wet cooling towers. In dry cooling towers, the air does not come into direct contact with the hot water, which is circulated through finned tubes forming a heat exchanger. As a result of non-contact, only sensible heat transfer is possible in this type of tower. In wet cooling towers, air comes into direct contact with the hot water. The hot water is injected into the tower in the spray zone. The water vaporizes as it flows down the tower, and hence there will be both sensible and latent heat transfer. Wet cooling towers, therefore, have better thermal performance. A drawback of wet cooling towers is that they might result in visible plumes arising from water condensation. Hybrid towers were introduced to reduce the effect of plumes where the dry section is incorporated atop the wet section. These were found to reduce plume visibility but require high capital investment. This thesis aims at studying wet cooling towers due to their higher thermal performance and low capital cost.

Wet cooling tower can be classified based on the method used to draw air into the tower; i) natural draft towers and ii) mechanical draft towers. In natural draft wet towers (see Fig. 1.2 as an example), air flows due to the density difference generated by heat transfer to the air. As the air gets heated and humidified, its density decreases, and it flows upwards to the

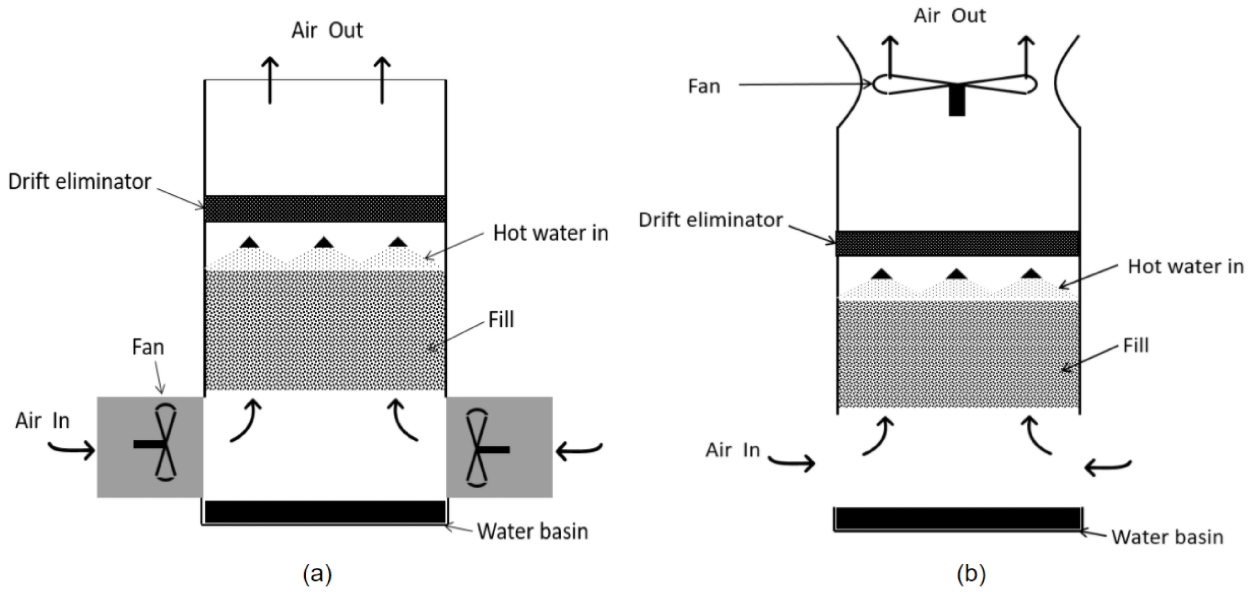

Figure 1.3 – (a) Forced draft cooling tower (b) Induced draft cooling tower

top of the tower due to buoyancy. In mechanical draft wet towers, the air is either pushed (forced draft) into the tower or is drawn (induced draft) into the tower by an external fan. In a forced draft tower, as shown in Fig. 1.3a the fan is installed at the inlet of the tower, while in the case of an induced draft tower, as shown in Fig. 1.3b the fan is installed at the exit.

Wet cooling towers are further classified based on the direction of air and water streams as counter-flow and cross-flow. In the case of counter flow, the air flows opposite to the direction of water flow as shown in Fig. 1.3 where air flows from bottom to top while water flows top to bottom. In cross-flow configurations, on the other hand, air flows at some angle to the water direction. For example, the cross-flow tower in Fig. 1.4 has one side of the fill open to the air enabling the air to enter the fill horizontally while the water flows vertically downwards, resulting in a cross-flow stream. More details about the classification mentioned above are found in references [2, 10].

Both cross-flow and counter-flow towers have their advantage, and the application alone should dictate which type of tower should be used. Cross-flow towers will serve better for maintenance access and variable flows, while counter-flow towers will serve better under tight spaces. Space is one of the main criteria in selecting the type of cooling tower as it involves much capital investment and sometimes limited space availability, for example, metropolitan cities. Moreover, the large size of the inlet in the cross-flow towers can develop icing, espe-

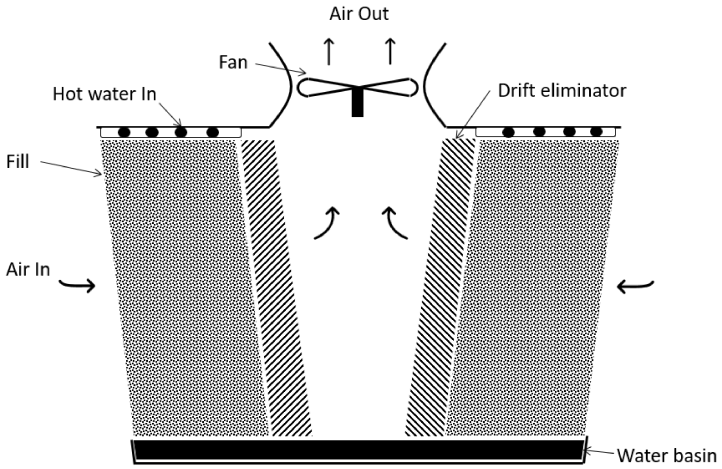

Figure 1.4 – Cross flow induced draft cooling tower. Remade based on the schematic in reference [2]

cially in a Northern country such as Canada. Unchecked icing may clog the fill, significantly reducing the inward flowrate and drastically reducing thermal performance. Considering the space and weather constraints, induced draft wet cooling towers are a good choice for many applications and, hence, this thesis aims to study such towers.

1.2.2 Cooling tower geometry and operation

A schematic of an induced draft counter-flow wet cooling tower is shown in Fig. 1.5 along with different zones inside a typical cooling tower. As shown in Fig. 1.5, a typically induced draft counter-flow wet cooling tower has the following zones: a) inlet region b) rain zone, c) fill zone, d) spray zone e) drift eliminator, f) fan, and g) collector basin. Air enters through the inlet region and leaves via the fan, while hot water enters the tower at the spray zone and is collected in the basin at the bottom.

Both water and air distribution are critical to the thermal performance of the tower. Air distribution, however, is multi-dimensional and depends on different factors, such as inlet geometry and fill location in the tower. Air enters the tower horizontally through the inlet region zone and is forced to flow upwards. This abrupt change in the direction results in a low-pressure region at the tower inlet, due to which a recirculation zone develops. The extent of the recirculation zone highly depends on the inlet geometry [11]. The recirculation zone gives rise to a non-uniform distribution of flow across the tower cross-section. An effective cooling tower model should predict the airflow profiles for the taken inlet geometry, which

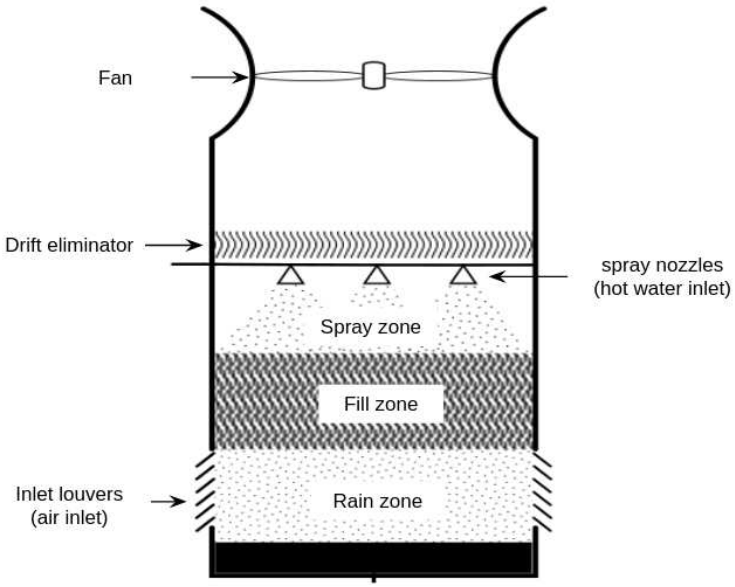

Figure 1.5 – Schematic of an induced draft cooling tower. Reproduced from reference [3] with permission

eventually shapes the flow into the rain zone.

The ambient air encounters water droplets for the first time in the rain zone as it enters the tower through the inlet. Water exiting the fill drops through the rain zone as it passes by the air inlet to the collection basin. In wet cooling towers, about 10-20% of the total heat transfer occurs in the rain zone [12]. Air, possessing the maximum momentum in this region, experiences resistance by the water drops as it changes its direction. Due to the inertial effects, air tends to move towards the center of the tower, resulting in a non-uniform distribution of the airflow across the tower cross-section. This flow behaviour continues until the air encounters the fill. Moreover, the air with low temperature and low moisture content come into contact with the relatively hotter air in the rain zone. Hence, the flow behaviour becomes vital as an uneven distribution can result in uneven mass and thermal transport across the rain zone. Such an uneven distribution of airflow across the tower cross-section makes the rain zone critical for analyzing the fluid flow behaviour.

Fill zone is considered as the heart of the cooling tower as about 60-70% of the total heat transfer is achieved in this zone [13]. It is a complex grid-like structure with multiple passages provided for the flow of water and air. These passages enable direct contact between the liquid and the gas phase. Enhanced heat and mass transfer can be achieved by increasing the residence time and the interface area between the gas and liquid phases. There are three types of fills: 1) splash, 2) film, and 3) film-grid. A splash type fill is a layer of horizontal

Figure 1.6 – Brentwood OF21MA Film fill. Reproduced from reference [3] with permission

bars or slats and grids that break up the falling water, reducing the average velocity and generating water drops of varying sizes. Smaller drop sizes and lower drop velocities resulted in increased interface area and increased drop residence time in the tower, respectively. A film-type fill comprises thin corrugated sheets of plastic where water is allowed to spread and form a film as it flows down the fill, increasing the interfacial area. The corrugated shape of the fill results in higher residence time. These two effects aid the heat and mass transfer between air and water. An example of a film type of fill is shown in Fig. 1.6. Film-grid falls between fil-type and splash-type fills.

The hot water is introduced into the tower in the spray zone through nozzles. Uniform distribution of water is paramount for the overall performance of the tower. Non-uniform distribution of water will result in dry parts of the fill which would provide less resistance to the airflow, thus resulting in non-uniform heat and mass transfer in the tower and reduced thermal performance. Hence, nozzles are used to evenly distribute hot water over the fill. As the water droplets fall from the nozzle, they lose energy which constitutes up to 5-15% of the total heat transfer in the tower [12]. The heat transfer in the spray zone depends on the diameter of the water droplets and the airflow distribution across the cross-section.

The drift eliminator shown in Fig. 1.7 is installed above the spray zone and is designed to reduce the drift, i.e., the undesirable loss of liquid water in the form of droplets caught in the air stream. It uses a series of plastic sheets arranged such that the exiting air stream is forced to take a sudden change in the direction. The sudden change in direction results in the relatively heavy water droplets hitting the sheets' surface and fall back into the tower.

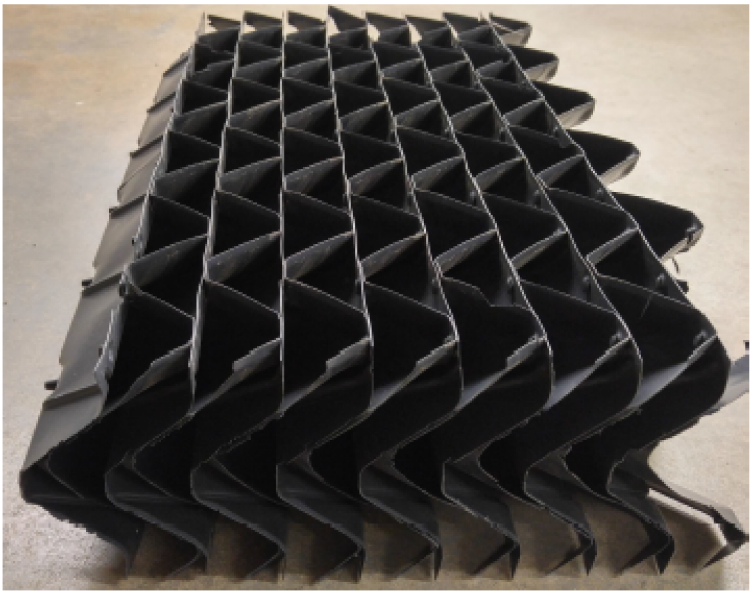

Figure 1.7 – Brentwood CF150MAx drift eliminator. Reproduced from reference [3] with permission

The fan installed at the top of the tower is responsible for maintaining the airflow in the tower. It overcomes the pressure drop due to different zones and maintains a specific airflow rate such that the thermal transfer is possible between the water and air. The fan power can control the airflow rate in the tower; however, an optimum value is needed as lower airflow rate results in higher water outlet temperature, whereas a higher flow rate requires higher fan power.

1.3 Literature Review

Computational fluid dynamics models have been developed for studying cooling towers in 2D [11, 14–16] and in 3D [17, 18]. These models have utilized the N-S equations to study the fluid flow over which the transport equations are applied to predict the heat and mass transfer. The water flow is modelled as a 1D flow, and predominantly Merkel's model [19], or an extension of it such as Poppe model [20] or Jaber and Webb's model [21] is used to estimate the outlet water temperature.

1.3.1 Computational fluid dynamics studies of airflow in cooling tower

One of the first computational fluid dynamics models of a cooling tower was introduced by Majumdar et al. [5, 14] where they developed a general, axisymmetric, finite difference

model applicable to natural and mechanical draft towers with counter-flow or cross-flow arrangements. In their analysis of fluid flow profiles in a cooling tower, the velocity distribution showed a non-uniform profile approaching the fill, a uniform flow in the fill, and a smooth turning and acceleration towards the exit. Vander Merwe and du Toit [6] studied the fluid profiles considering fill as a porous media and observed a similar profile as of Majumdar's [5] at the fill inlet. Milosavljevic and Heikkila [16] developed a three-dimensional model using ANSYS FLUENT to analyze the flow profile at the inlet of a forced draft cooling tower. They observed a non-uniform distribution of the air across the fill inlet. The vertical distance from the fill inlet to the tower inlet is varied, and the flow distribution improved with increasing vertical height. It was noted that the flow distribution is also improved by either having a flow straightener or having a bell-shaped air spreader at the tower inlet. Williamson et al. [7] in his 2-dimensional study of a natural draft cooling tower, studied the non-uniformity nature of the flow in a cooling tower and observed that the flow in most cases is uniform in both fill and spray region but has a considerable non-uniformity in the rain zone. The non-uniformity has a significant effect on the cooling load of the rain zone; however, it is dependant on multiple factors like the droplet size, fill height, water flow rate, and to some extent, the inlet height.

A good numerical model that estimates the fluid flow distribution in a cooling tower must include an accurate representation of the inlet losses as they constitute a significant portion of the overall pressure loss [22]. Inlet losses are the pressure drops traditionally associated with the entrance effects to duct flows. The sudden contraction of flow as it enters the tower and high shear stresses on the molecules adjacent to the wall just inside the entrance causes the separation of the accelerating fluid downstream of the entrance. One of the first attempts at modelling cooling tower inlet losses was studied by Lowe and Christie [23]. Terblanche and Kroger [8] in their experimental study, showed that inlet losses highly depend on the fill resistance. Du Preez and Kroger [9] arrived at a similar conclusion with their experimental study where they investigated the inlet losses at the base of a circular natural draft cooling tower. De Villiers and Kroger [22] experimentally obtained an inlet loss coefficient and showed that it decreased with an increasing inlet rounding radius, suggesting that the inlet geometry affects the flow profile and can be used to control the flow distribution in the rain zone. The study was extended by Reuter and Kroger [11] who used a CFD model to analyze the flow profiles. They reported that the inlet geometry affects the flow distribution. Keeping this in consideration, in the current study, the domain of the cooling tower is extended to include a zone connecting the tower inlet with the ambient zone.

Turbulence modeling

Numerical models that have studied airflow in cooling towers have estimated the velocity and pressure distribution by solving the Reynolds Averaged Navier-Stokes (RANS) equations as the flow in the cooling tower domain is turbulent. Majumdar et al. [5, 14] and Hawlader and Liu [15] have used an algebraic turbulence model to estimate the effective viscosity, while other numerical studies have used the $k-\epsilon$ turbulence model [16, 17, 24–26].

These turbulence models aim to predict the turbulence viscosity that appears in the RANS equations due to turbulent mixing. In algebraic turbulence models, the turbulent viscosity is evaluated based on an empirical relation, and, hence, it is a fixed value throughout the domain. On the other hand, in the $k-\epsilon$ turbulence model, turbulent viscosity is evaluated based on the turbulent eddies. A turbulent eddy can be thought of as a local swirling motion of fluid that encompasses the kinetic energy associated with the turbulent flow. Turbulence features a cascading effect, i.e., the kinetic energy transfers from a large eddy to a more miniature eddy that eventually dissipates into heat at a micro-scale. The turbulent viscosity is higher at the zones where the turbulent eddies are strong and is almost equal to zero where the turbulent eddies are negligible [27].

The $k-\epsilon$ turbulence model provides a good approximation for most flows, however, it has been observed to perform poorly when flow separation is present [28]. In the rain zone, the flow undergoes a sudden change in direction resulting in flow separation. Therefore the applicability of the $k-\epsilon$ model to cooling towers must be assessed. Majumdar et al. [14] noted that sophisticated models such as the $k-\epsilon$ turbulence models might not be useful unless the cells dimensions are smaller than the pitch of the fill element.

A mesh refinement of the order of the lowest turbulence scale (Kolmogorov length scale) increases the computational cost and might become prohibitive for three-dimensional modelling. To overcome this computational cost, Guermond et al. [29] introduced an artificial viscosity concept called an entropy viscosity model that is based on the numerical residual of the energy (entropy) equation. The artificial viscosity is defined such that it vanishes in low turbulent eddy regions and becomes active in high turbulent eddy regions. Though the entropy viscosity model is observed to have better control over the system, it has not been explored for steady-state conditions. Hence, an algebraic turbulence model suggested in the literature [14, 15] is utilized in the current study.

Air flow in the fill

The fill is the primary pressure drop region in the cooling tower. The air and water flow through the splash bars or the film-type sheets in opposite directions. The airflow distribution entering and leaving the fill depends on the water loading and fill characteristics [11, 25]. Hence, it is imperative to have a good understanding of the fill such that the airflow distribution in the tower is aptly predicted.

The fill is modelled as a momentum sink in the majority of the models in literature where the resistance offered is estimated based on the equation

$$\Delta p = k_f \frac{1}{2} \rho v^2 \tag{1.1}$$

where k_f is the loss coefficient of the fill [14, 17, 24, 25, 30]. Hawlader and Liu [15] utilized a slightly modified equation where the power to the velocity is a dependant parameter specific to the fill. Empirical relations estimate the loss coefficient. A comprehensive summary of empirical loss correlations available in the literature is provided in reference [12].

The flow inside a fill undergoes a complex path which is not captured by having it as a pressure drop zone. Becker et al. [31] in his study of flow around an induced draft mechanical cooling tower, assessed the pressure prediction inside a cooling tower by considering fill as a porous media. A viscous resistance is considered for pressure prediction, which is known as Darcy's law, shown below

$$\nabla p = \mu \hat{\boldsymbol{K}}^{-1} \boldsymbol{v} \tag{1.2}$$

where $\hat{\boldsymbol{K}}$ is the permeability matrix of the medium, a measure of resistance to the fluid, and $\boldsymbol{v}$ is a velocity vector. His study was mainly focused on the external flow, and hence the flow profiles inside were not analyzed. Vander Merwe [6] extended the study of Becker et al. [31] to study the flow profile inside a mechanical draft cooling tower and compared the results to those in Majumdar et al. [5]. The overall profile in both cases was similar; however, van der Merwe and du Toit observed a difference of profiles near the walls and a more significant recirculation zone. No other flow behaviour was analyzed inside; however, the study was limited in the sense that the turbulence effects that arose by the fill were not considered. In this regard, Burchart [32] suggested to have an inertial term along with the viscous term, which is known as Forchheimer estimation.

The fills, as mentioned before, can be a film type and splash or can be both. The permeability value of the fill can be adjusted based on the directional flow of the fill. For orthotropic

fill resistance, such as film type, the oblique flow entering the fill is forced into the vertical direction by the fill sheets [11]. The splash fill can be considered as an isotropic porous medium having the same permeability in principle directions. To better capture flow and flexibility to adapt to different cases, the fill zone is modelled as a porous media.

Computational domain

The fluid flow in a cooling tower is decided by the geometry of the cooling tower. Most of the past CFD studies have focused on natural draft cooling towers, while mechanical draft cooling towers remain least explored [7, 15, 18, 24, 33]. The fluid flow in mechanical draft towers is different as these towers usually have a rectangular cross-section contrary to the circular cross-section of natural draft cooling towers. Further in mechanical draft towers, while a fan is used to induce/force the flow in a mechanical draft cooling tower [12]. Most mechanical cooling towers are comparatively smaller in size and do not have a hyperbolic shape. Because of this reason, the external draft is necessary to drive the flow as the geometry does not aid the acceleration of the flow as in a natural draft tower. Considering all these differences, the fluid flow in mechanical draft towers is very different from natural draft towers and, hence, is the focus of this study.

Unlike spray and fill regions, the fluid flow behaviour in the rain zone is influence by many factors such as inlet effects, fill characteristics, its location in the tower, and to some extent, the tower inlet height. Due to the multiple factors, the fluid flow in the rain zone results in non-uniform distribution, significantly affecting the tower's thermal performance. Analyzing the flow behaviour becomes more prominent in a mechanical draft tower due to its geometrical and space constraints. All these factors emphasize the need to study fluid flow. Most studies in the literature were focused on the thermal performance [7, 14, 15, 33] while few [16–18] have tried to analyze flow profiles in the tower. Most have analyzed the flow profiles in the natural draft cooling tower, while flow behaviour in the mechanical draft cooling tower is least explored. Hence, this study aims to analyze the fluid flow and the main factors that affect the fluid flow behaviour in a mechanical draft cooling tower.

1.3.2 Heat and mass transfer in the tower

The thermal performance of a cooling tower can be estimated by incorporating a heat and mass transfer model into the above-established airflow model. Upward flowing air comes into direct contact with hot water as it travels through the spray, fill and rain zones under the

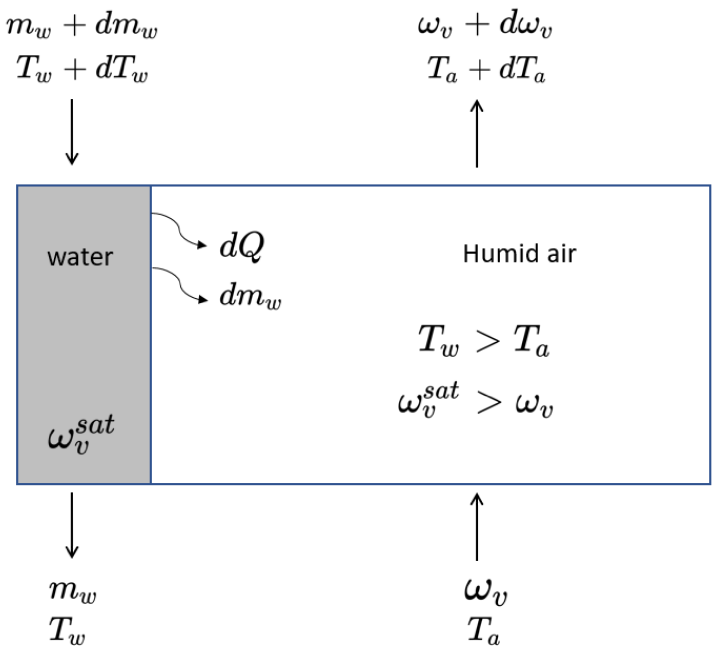

Figure 1.8 – Control volume for transport variables

influence of gravity. Water is sprayed in droplets with certain velocities in different directions and may either break into many droplets or form a film over a fill, depending on the type of fill used. This flow of water is complex and is usually modelled as a one-dimensional flow [14, 15, 17]. The transfer of mass and energy from the water to air as shown in Fig. 1.8 are, however, coupled with the fluid flow model of the air where the exchange of mass and energy from liquid to air is associated with the respective source term.

The source terms are evaluated based on the empirical equation proposed by Merkel [19], where a semi-empirical equation was used to accommodate the mass and energy balance in the tower. The semi-empirical equation is widely accepted due to its simplicity in computation as in equation (1.3)

$$\text{Me} = \frac{KaV}{m_w} = \int_{T_{wo}}^{T_{wi}} \frac{c_w \mathrm{d}T}{h_{as} - h_a} \tag{1.3}$$

where Me is dimensionless Merkel number, K is mass transfer coefficient, kg/m^{2}s, a is surface transfer area per unit volume of fill, m^2/m^3, V is the volume of the fill, m_w is water mass flowrate, T_{wo} is outlet water temperature, T_{wi} is inlet water temperature, c_w is the specific heat of water, h_{as} is the saturated enthalpy of vapour at water temperature and h_a is the enthalpy of vapour at air temperature. The thermal performance of the tower, hence, can be evaluated by the Merkel number for which fill specific empirical numbers are generated. Once the Merkel number is known, the mass transfer coefficient Ka in Eq. (1.3) is known

by which the source term in the advection-diffusion equation can be calculated.

The empirical relations related to the fill mass transfer coefficients are derived from laboratory tests. Kloppers and Kroger [1, 12] in their detailed test procedures measured the water inlet and outlet temperatures along with the air inlet temperature. The Merkel can then be used to find the Merkel for the fill. The data is correlated to give an empirical equation of the Merkel number as a function of the dependent variables. Different formats for the empirical equations have appeared in the literature. Lowe [23] proposed the empirical equation as shown in eq (1.4) while Kroger [12] proposes eq (1.5):

$$\frac{Me}{L_{fi}} = c_1 \left(\frac{G_w}{G_a}\right)^{c_2} \tag{1.4}$$

$$\frac{Me}{L_{fi}} = c_1 G_w^{c_2} G_a^{c_3} \tag{1.5}$$

where c_1, c_2 and c_3 are the fill specific constants obtained from experiments, G_a is airflow rate per unit area, G_w is water flow rate per unit area and L_{fi} is the depth of the fill. Kloppers and Kroger [1, 12] found that the Merkel number is not dependent on air inlet temperature or wet-bulb temperature but is a function of the fill depth and the above equation is modified as:

$$\frac{Me}{L_{fi}} = c_1 G_w^{c_2} G_a^{c_3} L_{fi}^{c_4} \tag{1.6}$$

Making use of these empirical equations, the mass transfer coefficient is obtained, which is utilized to obtain the heat transfer coefficient by Lewis factor relation. The heat transfer coefficient in the tower is estimated by using Lewis factor relation as in equation (1.7). Merkel [19] assumed that the Lewis factor to be unity while Bosmjakovic [34] has reported that it may be lower than unity and provided with a formula as equation (1.8).

$$\mathrm{Le_f} = \frac{h}{c_p K a} \tag{1.7}$$

$$\mathrm{Le_f} = 0.866^{2/3} \left(\frac{\omega_s^w + 0.622}{\omega + 0.622} - 1\right) \ln\left(\frac{\omega_s^w + 0.622}{\omega + 0.622}\right)^{-1} \tag{1.8}$$

where h is the heat transfer coefficient.

Majumdar et al. [5, 14] evaluated the rate of mass transfer from water to air based on Lowe's empirical equation (1.4). Their model provides a good estimation of the temperature on the moisture profiles; however, taking the Lewis factor to unity results in an inaccurate approximation of the heat and mass transfer. Besides, the fill depth is not considered in the evaluation of the mass transfer coefficient, which according to Klopper and Kroger [1, 12]

also affects the transfer coefficient. Razafindrakoto et al. [17] followed a similar approach where a three-dimensional airflow model is coupled with one-dimensional heat and mass transfer water-air exchange model. The coupling, however, was implemented in steps where the convection, diffusion, and pressure-continuity were solved in consecutive steps, which according to the author, needs improvement as the predicted values deviate from the experimental values. The model is also observed to have an underpredicted air flow rate due to which the thermal performance is not aptly predicted. Additionally, these models have only considered fill as heat and mass sources when other regions like spray and rain significantly contribute to thermal performance.

Hawlader and Liu [15] extended Majumdar's model [14] to include the heat and mass transfer in the rain zone and reported that about 83% of the total heat transfer occurs in the fill zone. It is also observed that about 90 % of the heat transfer in the rain zone is through evaporation. Al-waked et al. [24] considered the one-dimensional flow of water in the fill zone as droplets, and transfer coefficients were derived based on Ranz and Marshall [35]. They reported that the droplet diameter has the most significant effect on the thermal performance of the tower. However, this approach might be valid for splash fill but may not be accurate for the case of film type fills. Williamson et al. [25] considered the film type nature of the flow and the one-dimensional heat and mass transfer inside the fill zone. The fill is divided into vertical layers, and in each layer, water temperature and its flow rate are kept constant. The volumetric mass transfer coefficient is estimated based on the correlation equations of Kloppers [1] and the Lewis factor is determined based on Bosjnakovics formula [20] which is then used to estimated the volumetric heat transfer coefficient. The resulted flow, in most cases, is relatively uniform through the fill but resulted in a considerable non-uniformity in the heat transfer due to the radial airflow in the rain zone.

Mass-transport analysis in literature [7, 14, 14, 24] have modelled water as a one-dimensional flow assessing the mass variation with height. Since the fluid flow in the domain was the main focus of this study, the heat and mass transport is simplified by solving the advection-diffusion equations with equivalent source terms in the fill zone without solving the water flow.

1.4 Objectives

From the above literature study, it is observed that while there have been sufficient studies on the natural draft cooling towers, the research related to mechanical draft cooling towers

is limited. The research focus was mainly directed towards the tower's thermal performance, while the effect of the fluid flow distribution is not highlighted. A three-dimensional model is necessary to study the effect of fluid flow distribution, especially in mechanical draft towers. The inlet geometry, the fill in the tower, fill height, and its parameters influence the airflow distribution, affecting the thermal performance. It is also to be noted that a three-dimensional model is computationally expensive and requires efficient models to solve the fluid flow. Since the flow is in the turbulent regime, a turbulence model is necessary to achieve a steady-state solution. Keeping the above issues in consideration, the objectives of this study are outlined as

- **To analyze the flow in a cooling tower and validate it with the experimental data**: This objective will focus on obtaining the fluid flow distribution in a cooling tower with and without fill. Fill is considered as a porous media, and the pressure drop obtained across the fill is validated with the experimental data.
- **To investigate the effect of different parameters affecting fluid flow distribution**: This objective will focus on the influence of inlet height, inlet geometry, fill location in the tower and fill parameters on the fluid flow distribution.
- **To estimate the heat and mass distribution in a cooling tower**: This objective will focus on solving the energy and moisture conservation equations based on the obtained fluid flow distribution in the tower.

Chapter 2

Theory

The fluid flow in the cooling tower is predicted by the Reynolds Averaged Navier-Stokes (RANS) equations. Advection-diffusion equations are utilized to estimate the heat and mass distribution in the tower based on the obtained fluid flow distribution.

2.1 Governing equations for empty tower case

In an empty tower, the flow has no restriction in its path, and no source of heat and mass is present, resulting in an incompressible flow, i.e., the fluid density is constant. In solving the fluid flow equations, another important aspect is to know the nature of the flow, i.e., whether it is laminar or turbulent. The characteristic length (width or breadth) of a mechanical draft tower is usually in the order of few meters, and the airflow velocity is usually in the order of a few m/s. The density and dynamic viscosity of air at standard conditions are 1.225 kg/m^3 and 1.8×10^{-5} Pa.s respectively (measured at STP). The Reynolds number of a flow is calculated by

$$Re = \frac{\rho u_{avg} D}{\mu} \tag{2.1}$$

where u_{avg} is the average velocity in the tower and D is the characteristic length of the tower. Owing to the large geometrical structures, the Reynolds number of a typical cooling tower is of the order of 10^5, suggesting the flow is well within the turbulent regime.

To solve such flows, the Navier-Stokes equations are time-averaged resulting in a steady-state equation and the turbulent effects are mapped in the final equation as Reynold stresses. The obtained set of equations are called the Reynolds averaged Navier-Stokes (RANS) equations. The final incompresible RANS equations are:

$$\nabla \cdot \boldsymbol{v} = 0 \qquad \text{in } \Omega \tag{2.2}$$

$$\rho \nabla \cdot (\boldsymbol{v} \otimes \boldsymbol{v}) = \nabla \cdot \left(-p\hat{\boldsymbol{I}} + 2\mu_{eff} \nabla_s \boldsymbol{v} \right) + \rho \boldsymbol{g} \qquad \text{in } \Omega \tag{2.3}$$

where p is pressure in Pa, ρ is the fluid density in kg/(m^3, $\boldsymbol{v}$ is the velocity in m/s, $\hat{\boldsymbol{\sigma}}$ is the Cauchy stress tensor, μ_{eff} is the effective viscosity (dynamic viscosity + turbulence viscosity) in Pa.s, ∇_s is the symmetric gradient, defined as $\nabla_s = \frac{1}{2}\left(\nabla + \nabla^T\right)$, $\hat{\boldsymbol{I}}$ is the unit tensor, $\boldsymbol{g}$ is the gravitational force and Ω is the computational domain.

The governing equations can be rewritten as

$$\nabla \cdot \boldsymbol{v} = 0 \qquad \text{in } \Omega \tag{2.4}$$

$$\rho \nabla \cdot (\boldsymbol{v} \otimes \boldsymbol{v}) + \nabla p - 2\mu_{eff} \nabla \cdot \nabla_s \boldsymbol{v} - \rho \boldsymbol{g} = 0 \qquad \text{in } \Omega \tag{2.5}$$

The gravity force is neglected as it do not provide any pressure difference that drives the flow inside the tower. The weak formulation is achieved by multiplying suitable vector valued functions to the above set of equations:

$$\int_\Omega q \nabla \cdot \boldsymbol{v} \ \mathrm{d}\Omega + \int_\Omega \boldsymbol{\omega} \cdot \left[\rho \nabla \cdot (\boldsymbol{v} \otimes \boldsymbol{v}) - 2\mu_{eff} \nabla \cdot \nabla_s \boldsymbol{v} + \nabla p \right] \ \mathrm{d}\Omega = 0 \tag{2.6}$$

The advantage of considering a weak formulation is that it automatically satisfies the natural boundary conditions. In the Galerkin method, the solution approximation functions and the test functions belong to the same vector space, i.e., both have the same basis functions.

The terms in the momentum equation can be expanded as follows:

$$\begin{aligned}
\int_\Omega \boldsymbol{\omega} \cdot \left[\rho \nabla \cdot (\boldsymbol{v} \otimes \boldsymbol{v}) \right] \ \mathrm{d}\Omega &= \rho \int_\Omega \nabla \cdot \left[(\boldsymbol{v} \otimes \boldsymbol{v}) \, \boldsymbol{\omega} \right] \ \mathrm{d}\Omega - \rho \int_\Omega \nabla \boldsymbol{\omega} : (\boldsymbol{v} \otimes \boldsymbol{v}) \ \mathrm{d}\Omega \\
&= \rho \int_\Gamma \left[(\boldsymbol{v} \otimes \boldsymbol{v}) \, \boldsymbol{\omega} \right] \cdot \boldsymbol{n} \ \mathrm{d}\Gamma - \rho \int_\Omega \nabla \boldsymbol{\omega} : (\boldsymbol{v} \otimes \boldsymbol{v}) \ \mathrm{d}\Omega \\
&= \rho \int_\Gamma (\boldsymbol{n} \otimes \boldsymbol{\omega})_s : (\boldsymbol{v} \otimes \boldsymbol{v}) \ \mathrm{d}\Gamma - \rho \int_\Omega \nabla \boldsymbol{\omega} : (\boldsymbol{v} \otimes \boldsymbol{v}) \ \mathrm{d}\Omega
\end{aligned} \tag{2.7}$$

where the following relationship has been used:

$$\hat{\boldsymbol{T}}_s \boldsymbol{v} \cdot \boldsymbol{n} = (\boldsymbol{n} \otimes \boldsymbol{v}) : \hat{\boldsymbol{T}}_s = (\boldsymbol{n} \otimes \boldsymbol{v})_s : \hat{\boldsymbol{T}}_s \tag{2.8}$$

where $\hat{\boldsymbol{T}}_s$ is a symmetric tensor of rank 2. The weak form of the viscous term reads as

follows:

$$\begin{aligned}\int_\Omega \boldsymbol{\omega}\cdot[-2\mu_{eff}\nabla\cdot\nabla_s\boldsymbol{v}]\ \mathrm{d}\Omega &= 2\mu_{eff}\int_\Omega \nabla\boldsymbol{\omega}:\nabla_s\boldsymbol{v}\ \mathrm{d}\Omega - 2\mu_{eff}\int_\Omega \nabla\cdot[\nabla_s\boldsymbol{v}\ \boldsymbol{\omega}]\ \mathrm{d}\Omega \\ &= 2\mu_{eff}\int_\Omega \nabla\boldsymbol{\omega}:\nabla_s\boldsymbol{v}_{eff}\ \mathrm{d}\Omega - 2\mu\int_\Gamma(\nabla_s\boldsymbol{v}\ \boldsymbol{\omega})\cdot\boldsymbol{n}\ \mathrm{d}\Gamma \\ &= 2\mu_{eff}\int_\Omega \nabla\boldsymbol{\omega}:\nabla_s\boldsymbol{v}\ \mathrm{d}\Omega - 2\mu_{eff}\int_\Gamma(\boldsymbol{n}\otimes\boldsymbol{\omega})_s:\nabla_s\boldsymbol{v}\ \mathrm{d}\Gamma \quad (2.9)\end{aligned}$$

The pressure gradient term reads:

$$\begin{aligned}\int_\Omega \boldsymbol{\omega}\cdot\nabla p\ \mathrm{d}\Omega &= \int_\Omega \boldsymbol{\omega}\cdot\left(\nabla\cdot p\hat{\boldsymbol{I}}\right)\ \mathrm{d}\Omega \\ &= \int_\Omega \nabla\cdot\left(p\hat{\boldsymbol{I}}\ \boldsymbol{\omega}\right)\ \mathrm{d}\Omega - \int_\Omega \nabla\boldsymbol{\omega}:p\hat{\boldsymbol{I}}\ \mathrm{d}\Omega \\ &= \int_\Gamma\left(p\hat{\boldsymbol{I}}\ \boldsymbol{\omega}\right)\cdot\boldsymbol{n}\ \mathrm{d}\Gamma - \int_\Omega \nabla\boldsymbol{\omega}:p\hat{\boldsymbol{I}}\ \mathrm{d}\Omega \\ &= \int_\Gamma(\boldsymbol{n}\otimes\boldsymbol{\omega})_s:p\hat{\boldsymbol{I}}\ \mathrm{d}\Gamma - \int_\Omega \nabla\boldsymbol{\omega}:p\hat{\boldsymbol{I}}\ \mathrm{d}\Omega \quad (2.10)\end{aligned}$$

The weak form of Eq. (2.6) reads:

$$\begin{aligned}&\int_\Omega q\nabla\cdot\boldsymbol{v}\ \mathrm{d}\Omega - \rho\int_\Omega \nabla\boldsymbol{\omega}:(\boldsymbol{v}\otimes\boldsymbol{v})\ \mathrm{d}\Omega + 2\mu_{eff}\int_\Omega \nabla\boldsymbol{\omega}:\nabla_s\boldsymbol{v}\ \mathrm{d}\Omega - \int_\Omega \nabla\boldsymbol{\omega}:p\hat{\boldsymbol{I}}\ \mathrm{d}\Omega = \\ &-\rho\int_\Gamma(\boldsymbol{n}\otimes\boldsymbol{\omega})_s:(\boldsymbol{v}\otimes\boldsymbol{v})\ \mathrm{d}\Gamma + \int_\Gamma(\boldsymbol{n}\otimes\boldsymbol{\omega})_s:\left[-p\hat{\boldsymbol{I}} + 2\mu_{eff}\nabla_s\boldsymbol{v}\right]\ \mathrm{d}\Gamma \quad (2.11)\end{aligned}$$

To simplify the complex terms, the following relationship is used,

$$\hat{\boldsymbol{A}}:\hat{\boldsymbol{T}}_s = \hat{\boldsymbol{A}}_s:\hat{\boldsymbol{T}}_s \quad (2.12)$$

where $\hat{\boldsymbol{A}}_s = \frac{1}{2}\left(\hat{\boldsymbol{A}} + \hat{\boldsymbol{A}}^T\right)$ is the symmetrized version of $\hat{\boldsymbol{A}}$. Taking (2.12) into account, Eq. (2.11) can be rearranged as:

$$\begin{aligned}&\int_\Omega q\nabla\cdot\boldsymbol{v}\ \mathrm{d}\Omega - \rho\int_\Omega \nabla_s\boldsymbol{\omega}:(\boldsymbol{v}\otimes\boldsymbol{v})\ \mathrm{d}\Omega + 2\mu_{eff}\int_\Omega \nabla_s\boldsymbol{\omega}:\nabla_s\boldsymbol{v}\ \mathrm{d}\Omega - \int_\Omega \nabla_s\boldsymbol{\omega}:p\hat{\boldsymbol{I}}\ \mathrm{d}\Omega = \\ &-\rho\int_\Gamma(\boldsymbol{n}\otimes\boldsymbol{\omega})_s:(\boldsymbol{v}\otimes\boldsymbol{v})\ \mathrm{d}\Gamma + \int_\Gamma(\boldsymbol{n}\otimes\boldsymbol{\omega})_s:\left[-p\hat{\boldsymbol{I}} + 2\mu_{eff}\nabla_s\boldsymbol{v}\right]\ \mathrm{d}\Gamma \quad (2.13)\end{aligned}$$

This set of equations is nonlinear and therefore it needs to be linearized, which in this case is done with Newton's method. Let us assume that at a $k-$th Newton iteration the pairs $\left\{\left(p^k,\boldsymbol{v}^k\right)\right\}$ fail to satisfy the Eqs. (2.6) but still satisfy all necessary boundary conditions. Then we require that the new pairs $\left\{\left(p^{k+1},\boldsymbol{v}^{k+1}\right)\right\} = \left\{\left(p^k+\delta p,\boldsymbol{v}^k+\delta\boldsymbol{v}\right)\right\}$ are the solution to the whole problem (both equations and boundary conditions are supposed to be satisfied).

$$
\begin{aligned}
&\int_\Omega q\nabla\cdot\left(\boldsymbol{v}^k+\delta\boldsymbol{v}\right)\ \mathrm{d}\Omega-\rho\int_\Omega\nabla_s\boldsymbol{\omega}:\left[\left(\boldsymbol{v}^k+\delta\boldsymbol{v}\right)\otimes\left(\boldsymbol{v}^k+\delta\boldsymbol{v}\right)\right]\ \mathrm{d}\Omega\\
&+2\mu_{eff}\int_\Omega\nabla_s\boldsymbol{\omega}:\nabla_s\left(\boldsymbol{v}^k+\delta\boldsymbol{v}\right)\ \mathrm{d}\Omega-\int_\Omega\nabla_s\boldsymbol{\omega}:\left(p^k+\delta p\right)\hat{\boldsymbol{I}}\ \mathrm{d}\Omega=\\
&-\rho\int_\Gamma\left(\boldsymbol{n}\otimes\boldsymbol{\omega}\right)_s:\left[\left(\boldsymbol{v}^k+\delta\boldsymbol{v}\right)\otimes\left(\boldsymbol{v}^k+\delta\boldsymbol{v}\right)\right]\ \mathrm{d}\Gamma\\
&+\int_\Gamma\left(\boldsymbol{n}\otimes\boldsymbol{\omega}\right)_s:\left[-\left(p^k+\delta p\right)\hat{\boldsymbol{I}}+2\mu\nabla_s\left(\boldsymbol{v}^k+\delta\boldsymbol{v}\right)\right]\ \mathrm{d}\Gamma
\end{aligned}
\tag{2.14}
$$

On expanding:

$$
\begin{aligned}
&\int_\Omega q\nabla\cdot\boldsymbol{v}^k\ \mathrm{d}\Omega+\int_\Omega q\nabla\cdot\delta\boldsymbol{v}\ \mathrm{d}\Omega-\rho\int_\Omega\nabla_s\boldsymbol{\omega}:\left(\boldsymbol{v}^k\otimes\boldsymbol{v}^k+\boldsymbol{v}^k\otimes\delta\boldsymbol{v}+\delta\boldsymbol{v}\otimes\boldsymbol{v}^k\right)\ \mathrm{d}\Omega\\
&+2\mu_{eff}\int_\Omega\nabla_s\boldsymbol{\omega}:\nabla_s\boldsymbol{v}^k\ \mathrm{d}\Omega+2\mu\int_\Omega\nabla_s\boldsymbol{\omega}:\nabla_s\delta\boldsymbol{v}\ \mathrm{d}\Omega-\int_\Omega\nabla_s\boldsymbol{\omega}:p^k\hat{\boldsymbol{I}}\ \mathrm{d}\Omega\\
&-\int_\Omega\nabla_s\boldsymbol{\omega}:\delta p\hat{\boldsymbol{I}}\ \mathrm{d}\Omega=\\
&-\rho\int_\Gamma\left(\boldsymbol{n}\otimes\boldsymbol{\omega}\right)_s:\left(\boldsymbol{v}^k\otimes\boldsymbol{v}^k+\boldsymbol{v}^k\otimes\delta\boldsymbol{v}+\delta\boldsymbol{v}\otimes\boldsymbol{v}^k\right)\ \mathrm{d}\Gamma\\
&+\int_\Gamma\left(\boldsymbol{n}\otimes\boldsymbol{\omega}\right)_s:\left(-p^k\hat{\boldsymbol{I}}\right)\ \mathrm{d}\Gamma+\int_\Gamma\left(\boldsymbol{n}\otimes\boldsymbol{\omega}\right)_s:\left(-\delta p\hat{\boldsymbol{I}}\right)\ \mathrm{d}\Gamma\\
&+\int_\Gamma\left(\boldsymbol{n}\otimes\boldsymbol{\omega}\right)_s:\left(2\mu_{eff}\nabla_s\boldsymbol{v}^k\right)\ \mathrm{d}\Gamma+\int_\Gamma\left(\boldsymbol{n}\otimes\boldsymbol{\omega}\right)_s:\left(2\mu_{eff}\nabla_s\delta\boldsymbol{v}\right)\ \mathrm{d}\Gamma
\end{aligned}
\tag{2.15}
$$

Rearranging the equation based on the known terms and solution variables

$$
\begin{aligned}
&\int_\Omega q\nabla\cdot\delta\boldsymbol{v}\ \mathrm{d}\Omega-\rho\int_\Omega\nabla_s\boldsymbol{\omega}:\left(\boldsymbol{v}^k\otimes\delta\boldsymbol{v}+\delta\boldsymbol{v}\otimes\boldsymbol{v}^k\right)\ \mathrm{d}\Omega\\
&+\int_\Omega\nabla_s\boldsymbol{\omega}:\left(-\delta p\hat{\boldsymbol{I}}+2\mu_{eff}\nabla_s\delta\boldsymbol{v}\right)\ \mathrm{d}\Omega+\rho\int_\Gamma\left(\boldsymbol{n}\otimes\boldsymbol{\omega}\right)_s:\left(\boldsymbol{v}^k\otimes\delta\boldsymbol{v}+\delta\boldsymbol{v}\otimes\boldsymbol{v}^k\right)\ \mathrm{d}\Gamma\\
&-\int_\Gamma\left(\boldsymbol{n}\otimes\boldsymbol{\omega}\right)_s:\left(-\delta p\hat{\boldsymbol{I}}+2\mu_{eff}\nabla_s\delta\boldsymbol{v}\right)\ \mathrm{d}\Gamma=\\
&-\int_\Omega q\nabla\cdot\boldsymbol{v}^k\ \mathrm{d}\Omega+\rho\int_\Omega\nabla_s\boldsymbol{\omega}:\left(\boldsymbol{v}^k\otimes\boldsymbol{v}^k\right)\ \mathrm{d}\Omega-\int_\Omega\nabla_s\boldsymbol{\omega}:\left(-p^k\hat{\boldsymbol{I}}+2\mu_{eff}\nabla_s\boldsymbol{v}^k\right)\ \mathrm{d}\Omega\\
&-\rho\int_\Gamma\left(\boldsymbol{n}\otimes\boldsymbol{\omega}\right)_s:\left(\boldsymbol{v}^k\otimes\boldsymbol{v}^k\right)\ \mathrm{d}\Gamma+\int_\Gamma\left(\boldsymbol{n}\otimes\boldsymbol{\omega}\right)_s:\left(-p^k\hat{\boldsymbol{I}}+2\mu_{eff}\nabla_s\boldsymbol{v}^k\right)\ \mathrm{d}\Gamma
\end{aligned}
\tag{2.16}
$$

2.1.1 Algebraic turbulence model

To account for turbulence, a μ_{eff} was introduced into the final governing equation which is the sum of dynamic viscosity, μ, and turbulence viscosity μ_{turb}, i.e,

$$
\mu_{eff}=\mu+\mu_{turb} \tag{2.17}
$$

The turbulence viscosity, μ_{turb}, needs to be estimated. In this thesis, an expression proposed by Majumdar et al. [5, 14] for cooling towers is used as shown below,

$$\mu_{turb} = C\rho u_{avg} y_l \tag{2.18}$$

where C is a constant equal to 0.06, ρ is the density of the fluid, u_{avg} is the average fluid velocity in the tower domain, and y_l is the characteristic length which is proportional to the local boundary layer width i.e,

$$y_l = \alpha y_b \tag{2.19}$$

where α is proportionality constant, and y_b is boundary layer width. The proportionality constant, α, is based on the flow type and for a radial jet is 0.125 [36]. It is chosen based on the radial nature of the flow obtained in the fan's presence. The other proportionality constants provided in reference [36] are mainly for the plane type of flow, and hence the radial jet constant is considered, which is more suitable for a system with a fan. The boundary layer width is equal to half of the channel width, i.e., for example, in ESDLab tower, the channel width is 0.645 m, for which the boundary layer width, y_b is equal to 0.3225 m. The average velocity in the tower is obtained by taking a cumulative average of measured velocity data. The data points collected at the outlet of the tower from experiments are averaged to evaluate the average velocity in the tower, which is explained in detail in section 3.1.2.

2.2 Governing equations with fill

As mentioned in the literature review, the fill is considered as a porous media in this current study. In considering the fill, the fluid is forced to pass through a restricted path that may have an effective smaller cross-sectional area compared to that of the rest of the tower cross-section. This may give rise to some compressibility effects, and hence compressibility has to be considered. In addition to the compressibility, the fluid flow in the porous media is very complex, and some type of averaging is used for such flows. The method of averaging is based on the assumption that locally averaged properties will suffice for design purposes [37].

Consider a small porous elementary volume shown in Fig. 2.1, where there is both fluid domain and solid domain. The two most common choices for representative elementary volume (REV) averaging are the phase and intrinsic average methods. For the phase average, the fill variables are averaged over the entire domain including the solid domain, while the intrinsic average, the fill variables are averaged over the domain of that the fluid exists. The phase and intrinsic REV averages are mathematically defined for a given function ϕ

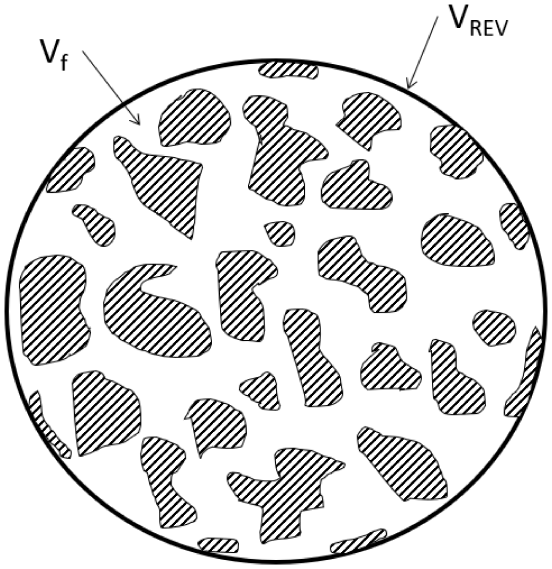

Figure 2.1 – Representation of a REV. Remade based on the schematic in reference [4]

respectively as

$$\langle \phi \rangle = \frac{1}{V_{REV}} \int_{V_f} \phi \, dV \tag{2.20}$$

$$\langle \phi \rangle^f = \frac{1}{V_f} \int_{V_f} \phi \, dV \tag{2.21}$$

where V_{REV} is the total volume of the REV and V_f is the volume of the fluid in the REV. These two REV averages are related to each other through the definition of porosity, ε, as follows

$$\langle \phi \rangle = \varepsilon \langle \phi \rangle^f \tag{2.22}$$

$$\varepsilon = \frac{V_f}{V_{REV}} \tag{2.23}$$

The resistance offered by the fill, $\boldsymbol{F}$, is given by:

$$\boldsymbol{F} = \mu \hat{\boldsymbol{K}}^{-1} \varepsilon \langle \boldsymbol{v} \rangle^f - C_F \hat{\boldsymbol{K}}^{-1/2} \langle \rho \rangle \left\| \varepsilon \langle \boldsymbol{v} \rangle^f \right\| \varepsilon \langle \boldsymbol{v} \rangle^f \tag{2.24}$$

where $\hat{\boldsymbol{K}}$ is the permeability tensor of the porous media and C_F is a constant. The resistance offered by the fill has two components: the viscous approximation term and inertial approximation term. The viscous approximation term also called as Darcy's law is the most probable approximation for the resistance when the flow is laminar. Since, the flow is turbulent as known from the literature review, it is imperative to add an inertial term which combined with the viscous term is called as Darcy-Forchheimer approximation.

In general, compressed RANS equations are solved in the tower incorporating the volume-averaged equation for the fill zone. Considering a d-dimensional cooling tower domain $\Omega \subset \mathbb{R}^d$ with a boundary Γ. It is known that the governing equations must be valid for two sets of domain, i.e, channel and porous media. Channel is the domain which is free of any kind of resistance to the flow while a resistance to the flow is present in the porous domain. Hence the domain, Ω has two sub domains, channel domain, $\Omega_c \subset \Omega$ with a boundary $\Gamma_c \subset \Gamma$ and porous domain, $\Omega_p \subset \Omega$ with a boundary $\Gamma_p \subset \Gamma$. Applying the assumptions above and simplifying the governing equations that were implemented in OpenFCST that are valid for all domains is as follows:

$$\nabla \cdot (\rho \boldsymbol{v}) = 0 \qquad \text{in } \Omega \tag{2.25}$$

$$\nabla \cdot (\rho \boldsymbol{v} \otimes \boldsymbol{v}) = \nabla \cdot \left(-p\hat{\boldsymbol{I}} + \hat{\boldsymbol{\sigma}}\right) + \boldsymbol{F} + \rho \boldsymbol{g} \qquad \text{in } \Omega \tag{2.26}$$

$$p = \rho \frac{RT}{M} \tag{2.27}$$

$$\hat{\boldsymbol{\sigma}} = 2\mu \nabla_s \boldsymbol{v} - \frac{2}{3}\mu \left(\nabla \cdot \boldsymbol{v}\right) \hat{\boldsymbol{I}} \tag{2.28}$$

$$\boldsymbol{F} = \begin{cases} \boldsymbol{0}, & \text{in } \Omega_c \\ -\mu \hat{\boldsymbol{K}}^{-1} \varepsilon \boldsymbol{v} - C_F \hat{\boldsymbol{K}}^{-1/2} \rho \left\| \varepsilon \boldsymbol{v} \right\| \varepsilon \boldsymbol{v}, & \text{in } \Omega_p \end{cases} \tag{2.29}$$

$$\varepsilon = \begin{cases} 1, & \text{in } \Omega_c \\ 0 < \varepsilon \leq 1, & \text{in } \Omega_p \end{cases} \tag{2.30}$$

$$\rho = \begin{cases} \rho, & \text{in } \Omega_c \\ \langle \rho \rangle, & \text{in } \Omega_p \end{cases} \tag{2.31}$$

$$\boldsymbol{v} = \begin{cases} \boldsymbol{v}, & \text{in } \Omega_c \\ \langle \boldsymbol{v} \rangle^f, & \text{in } \Omega_p \end{cases} \tag{2.32}$$

On following the same procedure of weak formulation and linearizing, the governing equations with fill results in

$$
\begin{aligned}
&\int_{\Omega} q\nabla\cdot\left(\delta\rho\boldsymbol{v}^k+\rho^k\delta\boldsymbol{v}\right)\,d\Omega-\int_{\Omega}\nabla_s\boldsymbol{\omega}:\left(\delta\rho\boldsymbol{v}^k\otimes\boldsymbol{v}^k+\rho^k\delta\boldsymbol{v}\otimes\boldsymbol{v}^k+\rho^k\boldsymbol{v}^k\otimes\delta\boldsymbol{v}\right)\,d\Omega\\
&+\int_{\Omega}\nabla_s\boldsymbol{\omega}:\left(-\delta p\hat{\boldsymbol{I}}+\delta\hat{\boldsymbol{\sigma}}\right)\,d\Omega-\int_{\Omega}\boldsymbol{\omega}\cdot\left(\delta\boldsymbol{F}+\delta\rho\boldsymbol{g}\right)d\Omega\\
&+\oint_{\Gamma}\left(\boldsymbol{n}\otimes\boldsymbol{\omega}\right)_s:\left(\delta\rho\boldsymbol{v}^k\otimes\boldsymbol{v}^k+\rho^k\delta\boldsymbol{v}\otimes\boldsymbol{v}^k+\rho^k\boldsymbol{v}^k\otimes\delta\boldsymbol{v}\right)\,d\Gamma\\
&-\oint_{\Gamma}\left(\boldsymbol{n}\otimes\boldsymbol{\omega}\right)_s:\left(-\delta p\hat{\boldsymbol{I}}+\delta\hat{\boldsymbol{\sigma}}\right)\,d\Gamma=\\
&-\int_{\Omega} q\nabla\cdot\left(\rho^k\boldsymbol{v}^k\right)\,d\Omega+\int_{\Omega}\nabla_s\boldsymbol{\omega}:\left(\rho^k\boldsymbol{v}^k\otimes\boldsymbol{v}^k\right)\,d\Omega\\
&-\int_{\Omega}\nabla_s\boldsymbol{\omega}:\left(-p^k\hat{\boldsymbol{I}}+\hat{\boldsymbol{\sigma}}^k\right)\,d\Omega+\int_{\Omega}\boldsymbol{\omega}\cdot\left(\boldsymbol{F}^k+\rho\boldsymbol{g}\right)\,d\Omega\\
&-\oint_{\Gamma}\left(\boldsymbol{n}\otimes\boldsymbol{\omega}\right)_s:\left(\rho^k\boldsymbol{v}^k\otimes\boldsymbol{v}^k\right)\,d\Gamma+\oint_{\Gamma}\left(\boldsymbol{n}\otimes\boldsymbol{\omega}\right)_s:\left(-p^k\hat{\boldsymbol{I}}+\hat{\boldsymbol{\sigma}}^k\right)\,d\Gamma
\end{aligned}
\tag{2.33}
$$

where:

$$
\delta p=\delta\rho\frac{RT}{M}
\tag{2.34}
$$

$$
\delta\hat{\boldsymbol{\sigma}}=\mu_{eff}\left(2\nabla_s\delta\boldsymbol{v}-\frac{2}{3}\left(\nabla\cdot\delta\boldsymbol{v}\right)\hat{\boldsymbol{I}}\right)
\tag{2.35}
$$

$$
\delta\boldsymbol{F}=\begin{cases}\boldsymbol{0}, & \text{in } \Omega_c\\ -\mu_{eff}\hat{\boldsymbol{K}}^{-1}\varepsilon\delta\boldsymbol{v}-C_F\hat{\boldsymbol{K}}^{-1/2}\left(\delta\rho\left\|\varepsilon\boldsymbol{v}^k\right\|\varepsilon\boldsymbol{v}^k+\rho^k\frac{\varepsilon\boldsymbol{v}^k\varepsilon\delta\boldsymbol{v}}{\left\|\varepsilon\boldsymbol{v}^k\right\|}\varepsilon\boldsymbol{v}^k+\rho^k\left\|\varepsilon\boldsymbol{v}^k\right\|\varepsilon\delta\boldsymbol{v}\right) & \text{in } \Omega_p\end{cases}
\tag{2.36}
$$

From Eq. (2.27), it is known that both pressure and density are related by the ideal gas law. In the case of the compressible flow, density is varied in the tower and it is considered as the solution variable instead of the pressure, i.e, density boundary conditions are applied in case of known pressure/density value. The viscosity as detailed in the previous section, is replaced by an effective viscosity μ_{eff} due to the turbulent nature of the flow. Q1Q2 elements are used to solve the compressible set of equations. A detailed discussion of the formulation is given in reference [38].

2.3 Heat and mass transfer

Once the fluid flow is established in the domain, the obtained velocity field is used to solve the advection-diffusion equations to achieve the heat and mass transport distribution in the tower. The governing equation for the mass transfer is

$$
\nabla\cdot\left(\rho\boldsymbol{v}\omega-\rho\mathcal{D}_{eff}\nabla\omega\right)=S_v
\tag{2.37}
$$

and the governing equation for the thermal transfer is

$$\nabla \cdot (\rho c_p \boldsymbol{v} T - \kappa_{eff} \nabla T) = S_T \tag{2.38}$$

where ω is the vapor mass-fraction, $\mathcal{D}_{eff}$ is the effective mass diffusivity tensor in m^2/s, S_v is the vapor source term $\mathrm{kg/m^3 s}$, T is the temperature of air in K, κ_{eff} is the effective thermal conductivity tensor in $\mathrm{W/(m\ K)}$, c_p is the specific heat of air per unit mass $\mathrm{J/(K\ kg)}$ and S_T is the heat source term in $\mathrm{J/(m^3\ s)}$.

S_v is the source term proportional to the difference between vapor density and saturated vapor density [14]

$$S_v = k_v \left(\omega_{\boldsymbol{v}} - \omega_{\boldsymbol{v}}^{sat}(T)\right) \tag{2.39}$$

where $\omega_{\boldsymbol{v}}$ is the moisture fraction of moist air, $\omega_{\boldsymbol{v}}^{sat}$ is the moisture fraction of the saturated moist air at a given temperature, and k_v is the effective mass transfer coefficient. The saturated moisture fraction of the moist air is evaluated as below:

$$\omega_{\boldsymbol{v}}^{sat} = \frac{1}{\rho} \frac{p_{sat}(T) M_v}{RT} \tag{2.40}$$

where $p_{sat}(T)$ is the saturation pressure at the local temperature, M_v is the vapor molar mass, R is universal gas constant and T is the local air temperature.

The constant k_v is dependent on the fill used and hence is obtained from the empirical equation provided by the fill manufacturer. Majumdar et al. [14] obtained the mass transfer coefficient k_v using Ka where K is the mass transfer coefficient, $\mathrm{kg/m^2 s}$ and a is the liquid-vapor interfacial area per unit volume, $\mathrm{m^2/m^3}$. The product of these two parameters is obtained by fitting to the experimental data using [1]

$$\frac{KaV}{m_w} = c_1 \left(\frac{L}{G}\right)^{c_2} H_{fi}^{c_3} \tag{2.41}$$

where V is the volume of the fill equal to product of the cross sectional area and height, H_{fi}, L is the mass flux of liquid (water) in $\mathrm{kg/(m^2 s)}$, G is the mass flux of gas (air) in $\mathrm{kg/(m^2 s)}$. From the above equation, the overall mass transfer coefficient Ka is achieved for a fixed $\frac{L}{G}$ ratio and known fill height, H_{fi}.

Once the mass transfer coefficient is achieved, Lewis factor relation is utilised to achieve the heat transfer coefficient k_T.

$$Le_f = \frac{k_T}{c_p Ka} \tag{2.42}$$

The source term S_t in Eq. (2.38) is is given by

$$S_T = k_T \left(T_w - T\right) \tag{2.43}$$

where T_w is the hot water temperature. The thermal transfer coefficient k_T is obtained by the overall mass transfer coefficient k_v and Lewis factor. Lewis factor values ranges from 0.5 to 1.3 and can influence the performance evaluation of cooling towers [39]. This, however, diminishes when ambient air is relatively hot and humid. Since, Merkel method is considered in the current study, a value of 1 is considered for Lewis factor.

The variation of temperature and mass fraction in the tower can influence the velocity and pressure distribution inside the tower. The density of air is related to temperature by equation

$$\rho = p\frac{M_a}{RT} \tag{2.44}$$

where p is pressure, M_a is the molecular mass of air in kg/mol, R is universal gal constant in J/(mol K), and T is the temperature in K. By this relation, changing air temperature affects the density of the air which in turn affects the velocity distribution as they are implicitly coupled with one another. In the current study, the effect of temperature is not considered, i.e., the velocity and density in the tower is not affected by the fluid flow temperature variation.

2.3.1 Effective diffusivities

As mentioned in the fluid flow section, the flow regime is usually turbulent. Hence the mass diffusive coefficient and thermal diffusive coefficient are replaced with effective diffusive terms which accommodate the turbulent effects.

$$\mathcal{D}_{eff} = \mathcal{D} + \mathcal{D}_{turb} \tag{2.45}$$

$$\kappa_{eff} = \kappa + \kappa_{turb} \tag{2.46}$$

where $\mathcal{D}_{turb}$ is the turbulent (mass) diffusivity and is related to the turbulent momentum diffusivity (eddy diffusivity) μ_{turb} through a dimensionless number called turbulent Schmidt number.

$$Sc_t = \frac{\mu_{turb}}{\rho\mathcal{D}_{turb}} \tag{2.47}$$

Koeltzsch [40] in his review on previous experimental investigations found that most authors used a constant for Sc_t ranging from 0.5 to 0.9. Wind tunnel experiments in the turbulent boundary layer showed a strong dependence of Sc_t on height within the boundary layer and

reported that the measured values range from 0.3 to 1.0. Another study by Flesch [41], based on the field observations under different stability and wind conditions, estimated values of Sc_t ranging from 0.18 to 1.34. However, they concluded that there was no clear trend in Sc_t with either stability, time of day, or wind speed in experiments.

Early CFD models on turbulent mass transport used $Sc_t = 0.7$ and Spalding [42] confirmed that this value is in close agreement with the experimental results. Launder [43] reported that a value of 0.9 suits for turbulence near the wall. Based on these two studies, most CFD studies have used values between 0.7 and 0.9. Tominaga et al. [44] reported that the optimum value of Sc_t is very different from the commonly used 0.7-0.9 values and are widely spread from 0.2 to 1.3. Further, they observed that a smaller value such as 0.3 tends to provide better predictions on concentration distribution around plumes and states that the Sc_t has a large influence on the prediction of mass transfer and thus needs to be selected carefully based on the flow characteristics. Since we are interested in the overall flow in the tower, a value of 0.7 is used in the current study.

Similar to the mass diffusivity, the thermal diffusivity is related to the turbulent diffusion coefficient through another dimensionless number called Prandtl number (σ_t) defined as the ratio of momentum diffusivity to thermal diffusivity

$$\sigma_t = \frac{c_p \mu_{turb}}{\kappa_{turb}} \tag{2.48}$$

In case of turbulence, Prandtl number is taken as unity [14], then the effective thermal conductivity can be written as

$$\kappa_{turb} = c_p \mu_{turb} \tag{2.49}$$

2.4 Domain, boundary conditions and input parameters

The domain considered plays a crucial role in understanding the flow behaviour. If only the flow inside the tower is of interest, one may choose not to include the ambient air outside the tower where the flow enters the domain, e.g. Majumdar et al. [14] and Hawlader and Liu [15]. However, the flow behaviour inside the tower might be influenced by the inlet geometry [11], and therefore the addition of air outside the tower might lead to more accurate results. The domain for the current study is developed based on the test facility in the ESDLab. The experimental setup shown in Fig. 2.2, built by Elizabeth Clare [3], has all the critical components of a full-scale cooling tower like the water distribution system, drift eliminator,

Figure 2.2 – Test facility in ESDLab. Reproduced from reference [3] with permission

fill, fan, and sink basin. The cross-sectional area of the tower is $0.645 \times 0.645\,\mathrm{m}^2$ with an overall height of 3.7 m and is designed to accommodate a fill of height as tall as 6 ft. A spray nozzle is installed, along with a drift eliminator on top of it. A rectangular basin is installed at the bottom of the tower, which collects the cold water. A fan is installed inside the rectangular duct upstream of the tower, responsible for drawing air into the tower. The fan is equipped with a variable frequency drive (VFD), meaning the airflow in the tower can be varied by changing the input power frequency to the drive.

The experiments were conducted with and without fill. With the current solver in OpenFCST, a solution is achieved for all the desired cases in the two-dimensional analysis. The solver is also able to provide a three-dimensional solution without fill.

2.4.1 Two dimensional domain

The test facility has a square cross-section with two inlets on opposite sides of the tower. As already mentioned before, since the inlet geometry influences the fluid flow behaviour inside

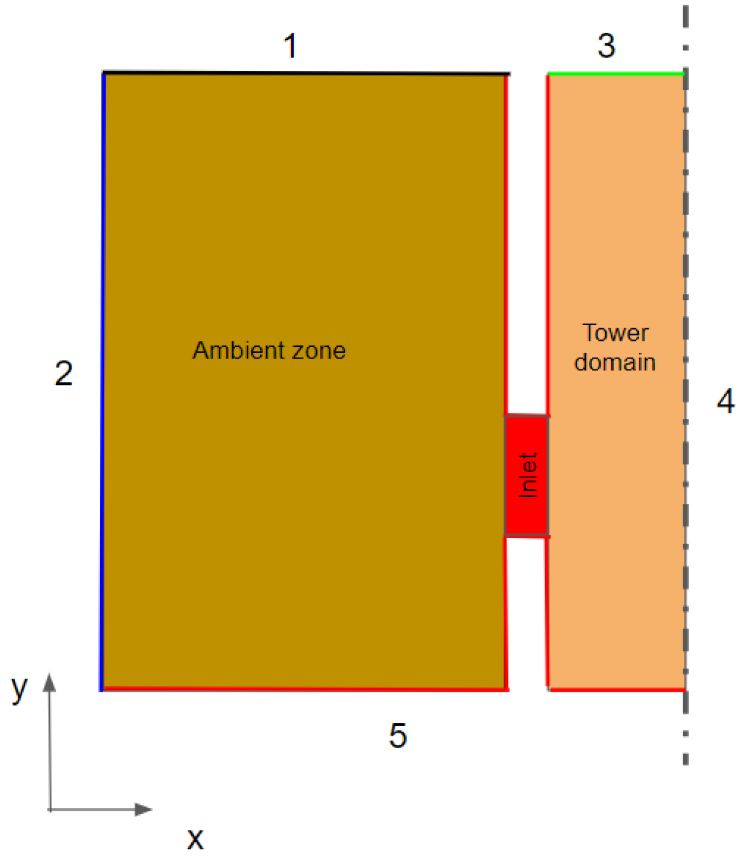

Figure 2.3 – 2D domain of the ESDLab tower

the tower, it is necessary to consider the ambient zone outside the tower. Hence, the domain is extended beyond the inlet of the tower outside the tower domain. Since the external air velocity (crosswind) is not considered, a symmetry condition is assumed due to which only a half section of the tower is simulated as shown in Fig. 2.3. The correct block of the domain labelled as the tower domain represents the half-section of the tower, while the left block represents the ambient section. Both are connected by an inlet which is shown as a red block in the schematic. Symmetry is considered across the central line in the tower represented by the dotted line towards the extreme right in the domain.

The tower simulations without fill are conducted to validate the model with the experimental data. The domain is kept free of any obstructions such as fill, and no water falling downwards is considered. The flow inside the tower is due to the fan installed and not due to the density difference. Hence, for simulations without fill, it can be safely assumed that the flow is incompressible, i.e., density is constant.

The numerals on each boundary represent the boundary IDs of the domain. Boundary ID 1

is the top ambient boundary which is considered as a pressure boundary. Since we are only interested in applying a pressure difference, gauge pressure values are applied as a boundary condition instead of absolute values. Boundary ID 2 is the vertical boundary and is set to be far from the tower inlet such that it can be considered as a wall, and hence a no-slip boundary condition can be applied. Boundary ID 3 is the outlet of the tower where both pressure and velocity can both be applied. From the measured data, both average velocity in the tower and pressure drop achieved is known. To have a good validation of the simulation, a pressure boundary condition is applied at the inlet and outlet for an empty tower case to evaluate the flow rate obtained. Having a pressure boundary condition at the outlet results in an unconstrained flow profile at the outlet, which otherwise would be constrained to have a uniform value. At boundary ID 4, a perfect-slip condition is applied. Boundary ID 5 (boundaries marked with red) are walls, and the no-slip condition is applied. The boundary conditions are summarized below

$$p|_{\Gamma_1} = p_{amb} \tag{2.50}$$

$$\boldsymbol{v}|_{\Gamma_2} = 0 \tag{2.51}$$

$$p|_{\Gamma_3} = p_{out} \tag{2.52}$$

$$(\boldsymbol{v} \cdot \boldsymbol{n})|_{\Gamma_4} = 0 \tag{2.53}$$

$$\boldsymbol{v}|_{\Gamma_5} = 0 \tag{2.54}$$

where p_{amb} is the ambient pressure, p_{out} is the pressure at the outlet, and $\boldsymbol{n}$ is the normal vector. The ambient pressure is the atmospheric pressure, and we apply a gauge pressure since the pressure difference is of interest. The velocity at different grid points in the plenum plane is known from the measured experimental data. In the case of simulations with fill, the same boundary conditions are applied, but density gradient is considered.

2.4.2 Three dimensional domain

Following the two-dimensional domain, the three-dimensional zone is considered as shown in Fig. 2.4. Initially, the entire domain containing all the four ambient zones on four sides of the tower is taken. The blue section is the actual tower, while the sections surrounding it represent the ambient zones. Two inlets on either side of the tower are shown in red, with the airflow path is shown with green arrows. From the geometrical symmetry along the two vertical planes, the domain can be cut, and a quarter part of the domain is generated, which is sufficient to provide the necessary information.

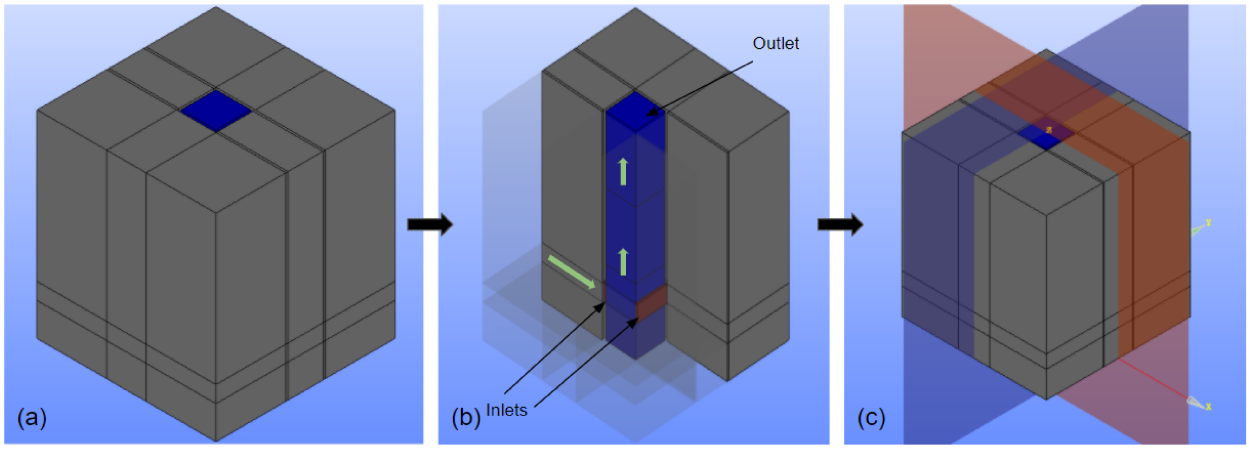

Figure 2.4 – (a) Full 3D domain with the ambient sections and tower domain shown in blue color. (b) Cooling tower with two inlets on either side and path taken by the flow. (c) Geometrical symmetry across the vertical planes

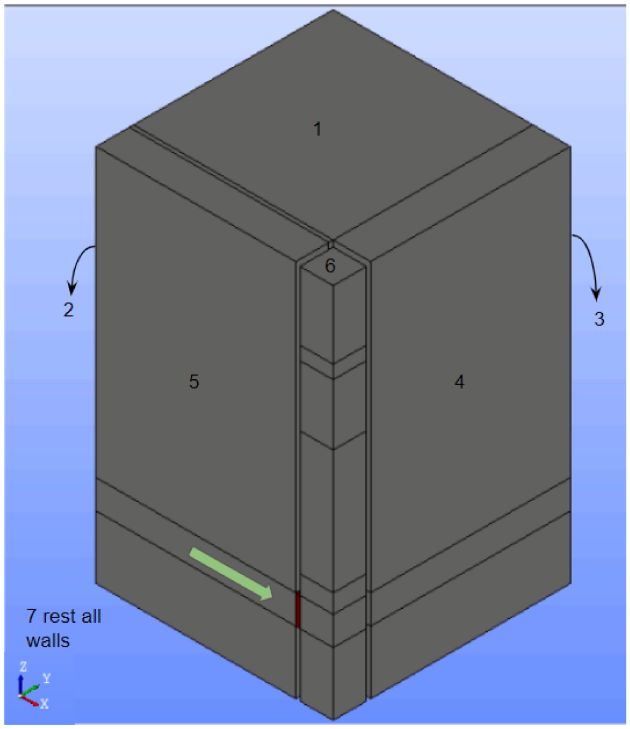

Figure 2.5 – Final computational domain with boundary IDs

The final considered quarter domain is shown in Fig. 2.5 along with the boundary IDs. Due to the symmetry, only one inlet becomes part of the final domain, shown in red. Boundary ID 1 represents the top boundary of the ambient zone. This zone is not affected by the fluid flow in the tower, and hence a Dirichlet pressure boundary condition is applied. Both boundary IDs 2 and 3 represent the far vertical boundaries of the ambient zone, which are considered as walls, and hence a no-slip boundary condition is applied. Boundary IDs 4

and 5 are formed due to the symmetry planes' cutting, and hence a symmetry boundary condition is applied. Boundary ID 6 is the outlet where a pressure boundary condition is applied. The rest of the boundaries of the domain are considered as walls with boundary ID 7. The boundary conditions applied are summarized below

$$p|_{\Gamma_1} = p_{amb} \tag{2.55}$$

$$\boldsymbol{v}|_{\Gamma_2} = \boldsymbol{v}|_{\Gamma_3} = \boldsymbol{v}|_{\Gamma_7} = 0 \tag{2.56}$$

$$(\boldsymbol{v} \cdot \boldsymbol{n})|_{\Gamma_4} = (\boldsymbol{v} \cdot \boldsymbol{n})|_{\Gamma_5} = 0 \tag{2.57}$$

$$p|_{\Gamma_6} = p_{out} \tag{2.58}$$

2.4.3 Input parameters

The input parameters for the simulation are based on the laboratory conditions of the ES-DLab. For all calculations in this study, the temperature is taken as 298 K and the pressure as 93000 Pa. The air density is 1.08 kg/m^3, and the humidity in the lab is approximately 15%, resulting in a moisture fraction of 0.0033 kg/kg.

The cross-section area of the tower is 0.645×0.645 m^2 with a total height of 3.65 m. An anti-fouling fill called OF21Ma is considered for which the porosity is obtained to be 0.975 from the manufacturers' datasheet. The permeability value is calculated from parametric studies which is described in detail in section 3.2.

2.5 Implementation and solution strategy

The linearized discrete weak formulation of governing equations along with appropriate boundary conditions, iterative procedures, and other related routines was implemented in the Open-Source Fuel Cell Simulation Toolbox (OpenFCST) [38]. OpenFCST is an open-source, finite element method-based multi-dimensional mathematical modelling software for polymer electrolyte fuel cells. The program can run in either serial or parallel mode (using the MPI protocol). For all the 2D simulations in OpenFCST, the serial computation is employed as it is quick to provide a solution; however, due to the drastic increase in degrees of freedom, a parallel computation was employed in 3D.

To predict the heat and mass transfer in the tower, five equations are solved i.e, continuity equation (Eq. 2.25), momentum equations (Eq. 2.26), mass transport equation (Eq. 2.37)

and thermal transport equation (Eq. 2.38). These equations are non-linear due to the presence of the convective term in all the transport equations. Hence, the Navier-Stokes equations are linearized as shown in section 2.1 and the transport equations are linearized as shown in Appendix A. Therefore, at every Newton step, the following incomplete Jacobian is solved to provide a solution update, $\delta \boldsymbol{u}$

$$\begin{pmatrix} A(\boldsymbol{u^k}) & B(\boldsymbol{u^k}) & 0 & 0 \\ B^T(\boldsymbol{u^k}) & C(\boldsymbol{u^k}) & 0 & 0 \\ 0 & 0 & K(\boldsymbol{u^k}) & 0 \\ 0 & 0 & 0 & M(\boldsymbol{u^k}) \end{pmatrix} \begin{pmatrix} \delta\rho \\ \delta \boldsymbol{v} \\ \delta T \\ \delta\omega \end{pmatrix} = \begin{pmatrix} R_\rho(\boldsymbol{u^k}) \\ \boldsymbol{R_v}(\boldsymbol{u^k}) \\ R_T(\boldsymbol{u^k}) \\ R_\omega(\boldsymbol{u^k}) \end{pmatrix} \tag{2.59}$$

and the new Newton iterate is then given by $\boldsymbol{u^{k+1}} = \boldsymbol{u^k} + \alpha\delta\boldsymbol{u}$ where α is set to one unless the residual increases between iterations. The complete Jacobian matrix is difficult to compute analytically; therefore, an incomplete Jacobian is solved where $\frac{\delta R_\rho}{\delta T}$, $\frac{\delta R_\rho}{\delta \omega}$, $\frac{\delta R_T}{\delta \boldsymbol{v}}$, $\frac{\delta R_T}{\delta \rho}$, $\frac{\delta R_\omega}{\delta \boldsymbol{v}}$ and $\frac{\delta R_\omega}{\delta \rho}$ are neglected. In order to simplify the problem, it is assumed that the temperature and mass fraction have a limited effect on the fluid flow. Therefore, the density and viscosity variations with temperature and mass fraction are neglected. Pressure is computed based on the Eq. (2.44).

The tolerance level is kept different for different simulations, i.e., the overall tolerance on absolute residual is taken as 10^{-8} for the empty tower case in 2D while it is taken as 10^{-5} in 3D. In the case of simulations with fill, only 2D simulations were performed for which the tolerance residual was taken as 10^{-6}.

2.6 Simulations in Ansys

Few of the simulations performed in OpenFCST were also performed using Ansys to; 1) check the validity of the simulation results and 2) assess the accuracy of the algebraic turbulence model. Fluid flow equations in OpenFCST are validated against standard problems, which are also detailed in the next chapter. However, an attempt is also made here to compare the simulation results and the computation time, especially for the 3D simulations. In OpenFCST, an algebraic turbulence model is employed, whereas in Ansys, options are available to employ a more sophisticated turbulence model like the $k-\epsilon$ turbulence model. The results obtained from both the simulations are then compared with the experimental data. The fluid flow equations solved in ANSYS are:

$$\nabla \cdot (\rho \boldsymbol{v}) = 0 \qquad \text{in } \Omega \tag{2.60}$$

$$\nabla \cdot (\rho \boldsymbol{v} \otimes \boldsymbol{v}) = \nabla \cdot \left(-p\hat{\boldsymbol{I}} + \hat{\boldsymbol{\sigma}} \right) + \rho \boldsymbol{g} \qquad \text{in } \Omega \tag{2.61}$$

$$\hat{\boldsymbol{\sigma}} = 2\mu \nabla_s \boldsymbol{v} - \frac{2}{3}\mu \left(\nabla \cdot \boldsymbol{v} \right) \hat{\boldsymbol{I}} \tag{2.62}$$

pressure and velocity are coupled by the SIMPLE scheme with the first-order discretization for the pressure and second-order discretization for the velocity following the Q1Q2 approximation considered in the OpenFCST. The domain and boundary conditions are as described in section 2.4.2. The tolerance on the residual is taken as 10^{-5} for all fluid equations and also the turbulent equations when the $k - \epsilon$ model is considered. To proceed with the algebraic model, laminar flow is considered with viscosity value revised to the desired value following Eq. (2.18).

Chapter 3

Results and discussion

The numerical model described in chapter 2 is utilized to perform simulations. The simulations are performed based on the data obtained from the ESDLab test facility to validate the model. First, the test facility is described in detail, followed by the experimental and simulation results.

3.1 ESDLab test facility

The ESDLab test facility is equipped with different sensors to measure velocity and pressure in the tower. As shown in Fig. 3.1, a pitot tube is inserted into the tower through a hole drilled on the side and is held in position. The pitot tube connected to a differential pressure sensor measures the total pressure and the dynamic pressure and provides static pressure as the output. A velocity sensor connected to the differential sensor reads the dynamic pressure, and the velocity is calculated with appropriate correction terms. More details about the measurement of velocity and pressure are provided in reference [3]. Various critical planes are selected in the tower as shown in Fig. 3.1 where the grey area represents a zone encompassing fill, spray distribution setup, and drift eliminator. The suggested planes are available for measurement only when the tower is empty, with only a few critical planes available when fill and drift eliminator are installed. At these critical planes, a 5×5 grid is selected based on the ASHRAE duct traverse method [45]. The pitot tube is placed at these points for a certain time over which time-averaged static pressure values are obtained. The procedure is repeated on all the points on the grid.

The incompressible N-S equations in chapter 2 are solved to estimate the fluid flow distribution in 2D with and without fill. The same equations are then used to estimate the flow distributions in 3D without fill. These are compared to experimental results obtained for an

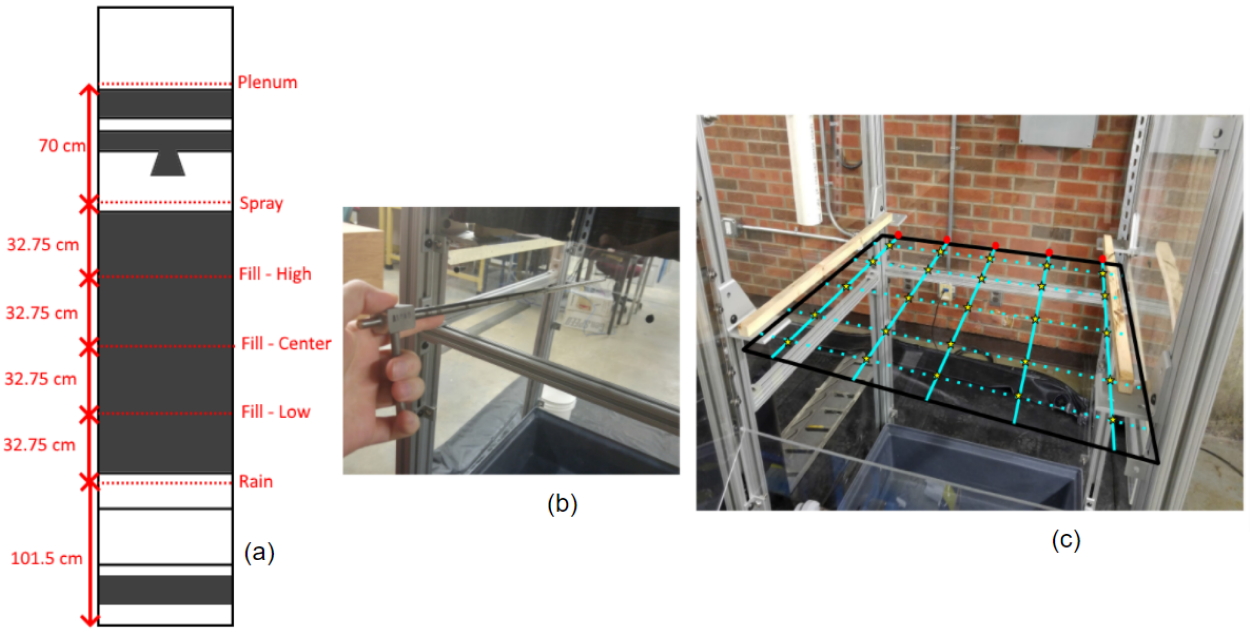

Figure 3.1 – (a) Critical planes in the tower (b) Pitot tube held in position for measuring velocity and pressure (c) Grid points over which the data is measured. Reproduced from reference [3] with permission

empty tower at different flow rates. Subsequently, compressible N-S equations are solved to estimate the fluid flow distribution when the fill is introduced into the tower.

3.1.1 Computational domain and mesh

Simulations are obtained for the computational domain in Fig. 3.2. To assess the grid independence of the solution, a series of simulations are performed starting with the initial mesh is shown in Fig. 3.3a. The considered mesh is globally refined, i.e., with each successive refinement, each cell is divided into four smaller cells. The solution is achieved for the successive refinements where two parameters are considered to check the convergence of the solution: the overall flow rate in the tower and the inlet plane velocity at the critical point marked with a red star in Fig. 3.3a. These parameters are plotted against the number of cells as shown in Fig. 3.3b. The accuracy is improved by global refinement, i.e., by reducing the cell size by half, but it also increases the computation cost. While the computational cost is not a concern in 2D, it is in the 3D case. To reduce the computational cost, adaptive refinement can be used so that only the cells with the highest numerical error are refined between successively refined meshes. This feature is used to minimize the computational cost.

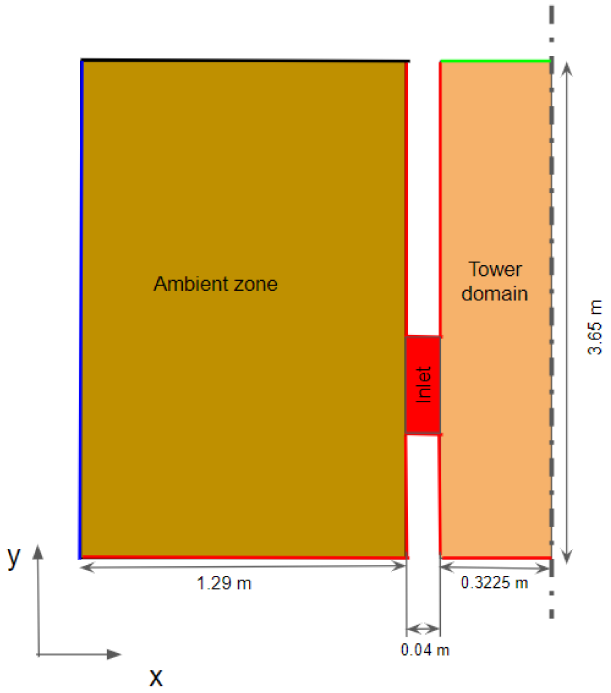

Figure 3.2 – Two dimensional domain considered with dimensions

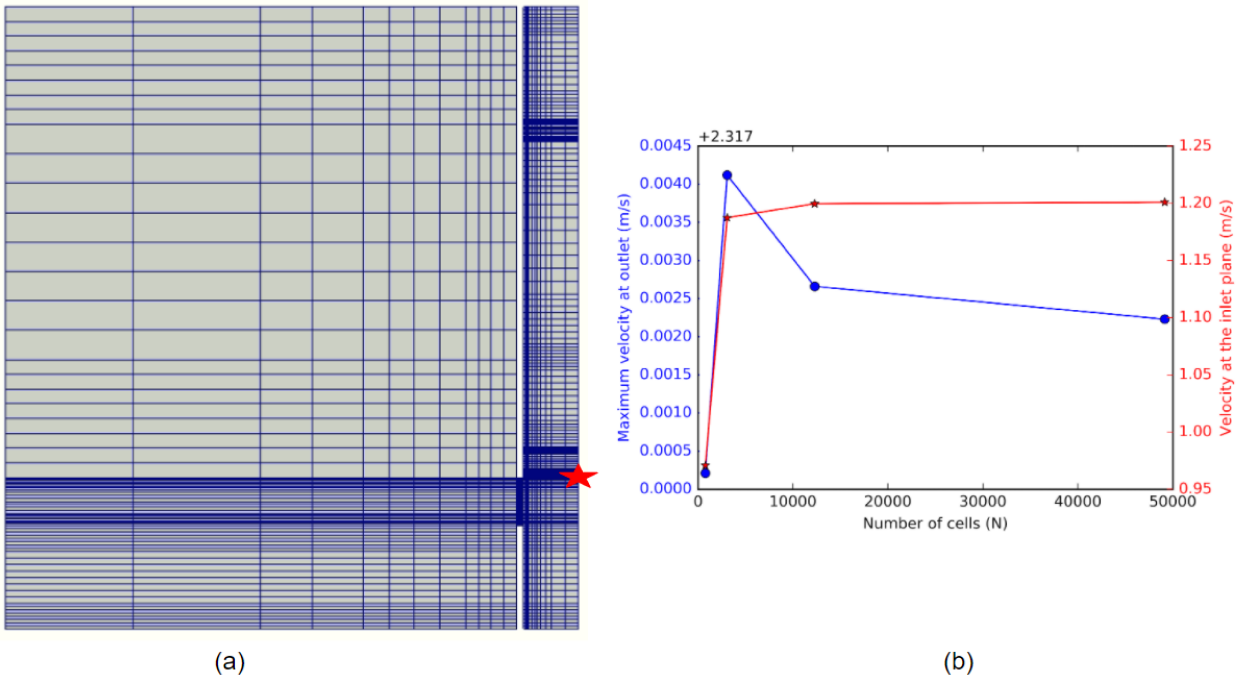

Figure 3.3 – (a) Initial mesh considered for grid independence study and (b) grid independent study with global refinement

When using adaptive refinement, only the cells which have high solution gradients are refined. The extent of cells refined can be regulated, and in the current study, it is taken as

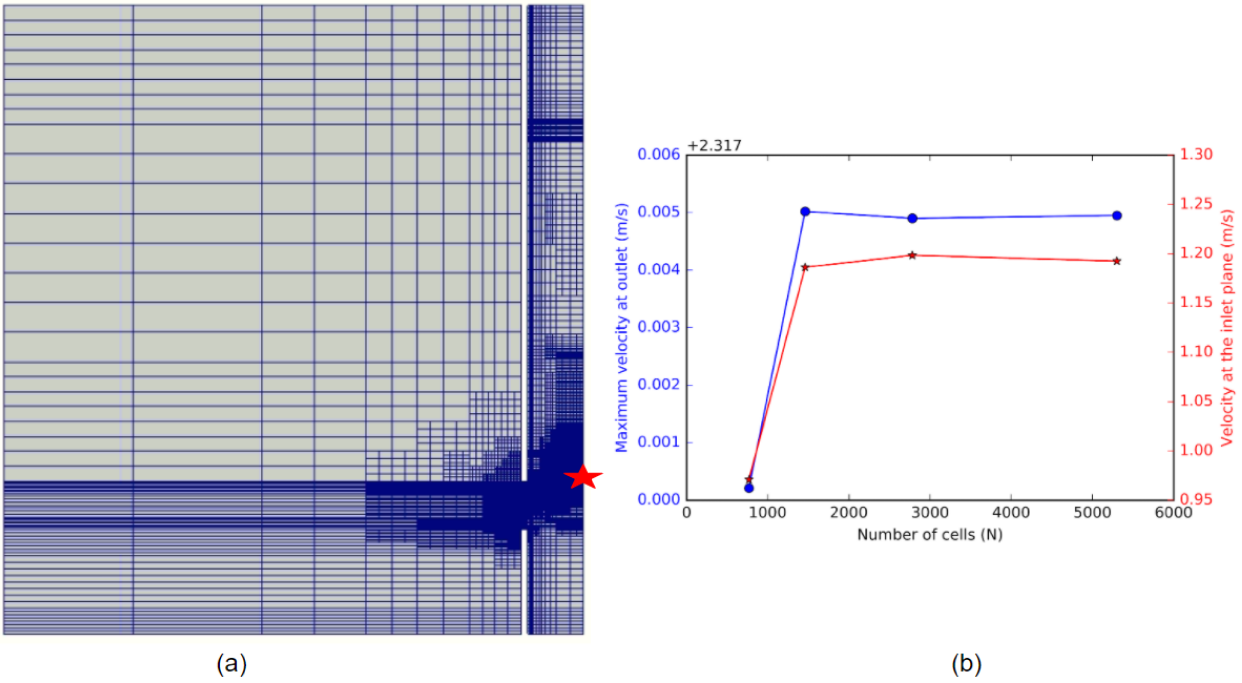

Figure 3.4 – (a) Final mesh obtained with adaptive refinement and (b) grid independent study with adaptive refinement

0.30, i.e., 30 percent of the total cells are refined. The initial mesh shown in Fig. 3.3a is adaptively refined multiple times and the final mesh obtained is shown in Fig. 3.4a. The inlet region of the tower is refined, while the outlet region has almost the same number of elements as the initial mesh. The solution gradients vary greatly at the inlet of the tower, which makes it a critical region and hence is refined. As in the previous case, the same parameters are plotted against the number of cells shown in Fig. 3.4b where both are observed to have converged to a particular value.

The tolerance on the absolute residual (square root of the sum of residuals of continuity and momentum equations) in both cases (global refinement and adaptive refinement) is 10^{-10} and both the obtained solutions have been observed to have convergence. However, there is a slight difference in the final solution values as observed from the values of maximum velocity at the outlet. The difference is due to the reason that the mesh in adaptive refinement is not refined at the outlet. At the same time, there is absolutely no difference in the inlet plane velocity value where the mesh is refined successively. The difference, however, is very minimal as observed from the plots in Fig. 3.3b and Fig. 3.4b.

The total number of cells for the global refinement is around 50000 which is drastically reduced to around 5000 cells for adaptive refining. This has also resulted in a reduction in

Table 3.1 – Experimentally measured average pressure and velocity at the plenum plane

Input Frequency (Hz)	Velocity (m/s)	Gauge pressure (Pa)
30	1.2096	4.22
40	1.6274	7.50
50	2.1065	11.94
60	2.5813	16.83

computation time of 10 times. Hence, to have faster computation with reasonable accuracy on the final solution, adaptive refinement is considered starting from the initial mesh in Fig. 3.3a with 2 levels of refinement.

3.1.2 Empty tower - 2D

Considering the computational domain in Fig. 3.2 and the boundary conditions specified in the section 2.4.1, the incompressible RANS equations are solved to obtain the fluid flow in an empty tower. The simulations are performed by using the experimental results, i.e., the pressure values obtained from the experiments are applied as boundary conditions. For different input frequencies of VFD, the velocity and pressure values are measured at the plenum plane in reference [3] are displayed in Table 3.1. The experimental results are measured over a 5x5 grid. The mean of all data points is calculated for the plenum plane (refer Fig. 3.1) by dividing the sum of all values by the total number of data points (25). This value of average pressure is then used as a boundary condition at the outlet. Considering a pressure of 4.22 Pa at the outlet for 30 Hz, the simulation is executed.

The corresponding average velocity in the tower is 1.2096 m/s for which the Reynolds number as calculated from Eq. (2.1) is 54700. i.e., the flow regime is well in the turbulent regime. As mentioned, in the current study, an algebraic turbulence model [14] is considered to accommodate the turbulent effects where the effective viscosity is evaluated using the average value of the velocity obtained from the experimental data. The effective viscosity for the considered simulation is 0.0032 Pa.s obtained from Eq. (2.18) where C = 0.06, ρ = 1.09 kg/m^3, $\alpha = 0.125$ and $y_b = 0.3225$ m.

Fig. 3.5 shows the velocity and pressure distribution for an empty tower operating at 30 Hz. The applied pressure difference drives the fluid flow in the tower. However, it is seen that a low-pressure zone is observed at the tower inlet as the fluid is restricted to change direction and flow vertically. Due to this sudden change in the flow behaviour, a vena-contracta is formed. A major portion of the flow is pushed towards the tower center with comparatively

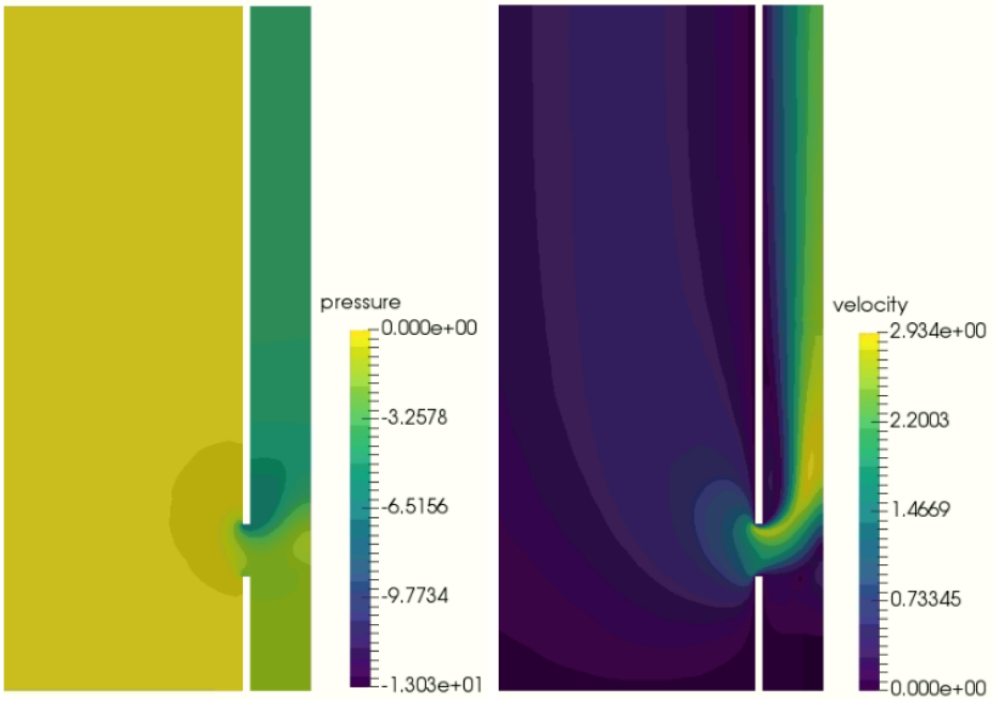

Figure 3.5 – Pressure and velocity distribution for 30 Hz fan input frequency

less flow near the tower wall resulting in a non-uniform distribution of flow across the tower cross-section.

The low-pressure zone at the inlet wall gives rise to a recirculation zone along the tower wall where the fluid flows in the opposite direction to the general flow direction. Due to the pressure difference, some part of the flow is pushed downwards, which is also observed in the velocity distribution in Fig. 3.5. The fluid flows back and mixes with the incoming flow resulting in a recirculation zone. The presence of this recirculation zone extends the uneven distribution of flow deep into the tower. The flow gradually shapes itself to form laminar flow downstream of the inlet, resulting in a parabolic velocity profile. This is because of the algebraic model considered for turbulence as suggested by Majumdar et al. [14].

The solution obtained with the current model depends on the turbulence viscosity. A change in turbulence viscosity can result in different velocity predictions in the tower. To understand the sensitivity of the results to this parameter, the turbulence viscosity value is varied, and the maximum velocity value at the outlet is plotted in Fig. 3.6. For a turbulence viscosity of 0.0032 Pa.s, the predicted maximum velocity at the outlet is 2.32195 m/s, the blue line in the plot. The viscosity value is varied in either direction to assess the sensitivity. The model does not result in a solution below 0.0016 Pa.s as the convection terms become too

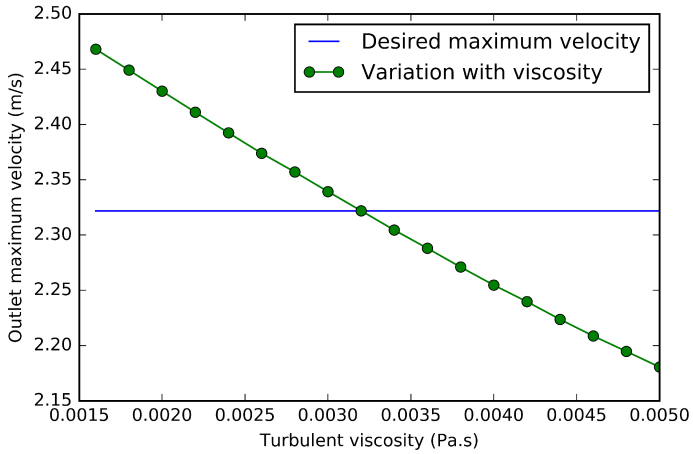

Figure 3.6 – Sensitivity of viscosity on outlet maximum velocity

dominant henceforth. On increasing the viscosity, the outlet velocity decreased due to the more viscous resistance offered. From the study, it is observed that a reduction of 50% of turbulence viscosity only changed the velocity prediction by approximately 5% showing less sensitivity.

To compare the simulations with the experimental data, an average velocity is considered. Since an algebraic model is considered, the obtained velocity profile is parabolic at the outlet. The average velocity is taken as 1/2 the maximum velocity obtained at the outlet.

Simulations were also performed at other fan speeds as shown in Table 3.1. The average velocity obtained in each case is plotted against the pressure at the plenum plane in Fig. 3.7. The experimental value of velocity is obtained by averaging over a cross-sectional grid. To account for any errors, the standard deviation of the data is also plotted to display the range of the experimental data. The obtained simulation results follow a similar trend to that of the experimental data well within the range of tolerance of the measurements. The discrepancy in the results might be related to the three-dimensional flow effects such as varying velocity profile along the inlet width and wall effects in the tower, which are not properly captured with a two-dimensional model.

The solution of the current two-dimensional model results in a fluid flow distribution in the central plane (refer Fig. 3.8a). The obtained fluid flow profile shows a sharp turn at the inlet with maximum velocity, while if the offset plane (Fig. 3.8b) is solved, the flow can have a similar velocity distribution. However, the distribution is affected by the sidewall of the tower, which effectively results in a different magnitude in the velocity [46]. The variation in the

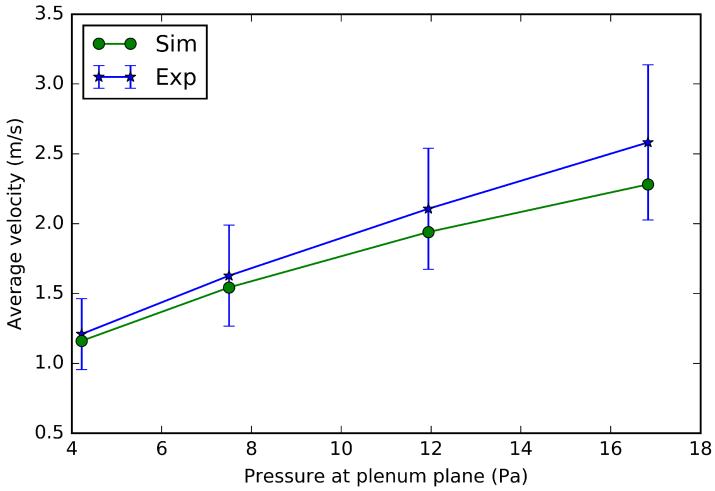

Figure 3.7 – Pressure vs average velocity comparison with experimental data

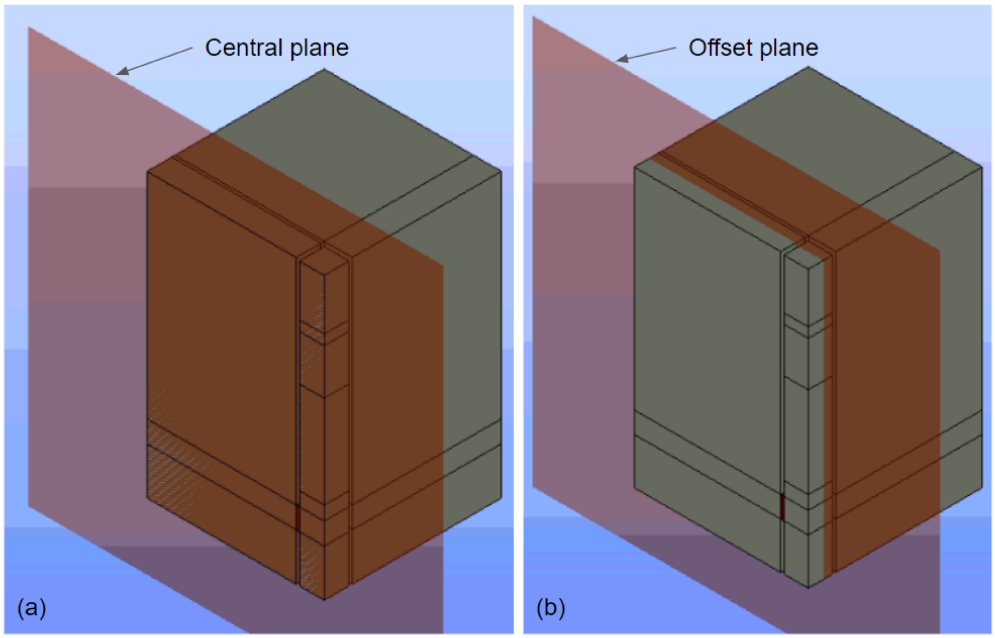

Figure 3.8 – (a) Central plane over which the two-dimensional model provides a solution (b) Offset plane slightly away from the central plane

flow velocity along the inlet emphasizes the need not to consider a single velocity profile for mass flow calculation. A similar explanation can be provided for the flow profile downstream of the tower as the no-slip conditions of the wall very well determine the flow behaviour. Thus, the overall flow rate discrepancy arises as these effects are not taken care of by a two-dimensional model. A detailed validation study requires a point-to-point velocity comparison with the experimental data. Such comparison is possible with a three-dimensional

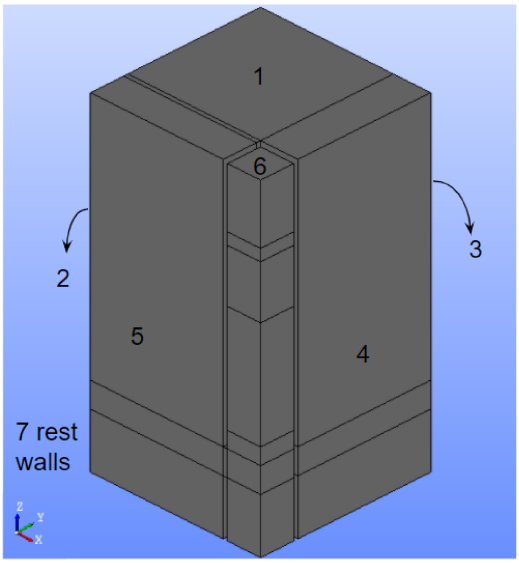

B.ID	Section of the domain	Boundary condition applied
1	Ambient top surface	Dirichlet Pressure (= 0 Pa)
2	Ambient vertical surface (normal - X axis)	Wall
3	Ambient vertical surface (normal - Y axis)	Wall
4	Ambient symmetrical plane (normal - Y axis)	Symmetry Condition
5	Ambient symmetrical plane (normal - X axis)	Symmetry Condition
6	Tower top surface	Dirichlet Pressure (= average value from experimental measurements)
7	Rest all outer surfaces	Wall

Figure 3.9 – 3D domain and boundary conditions applied

model, which is discussed in the next section. Additionally, the turbulence model considered also affects the flow behaviour, which is also discussed in the three-dimensional model.

3.1.3 Empty tower - 3D

To capture the three-dimensional effects and compare the velocity profiles inside the tower, simulations are performed with the 3D domain and boundary conditions as shown in Fig. 3.9. The pressure value at the outlet is taken from Table 3.1. The incompressible N-S equations are solved using Newton's iterative method in OpenFCST. In addition to OpenFCST, simulations were also conducted in Ansys. The same simulations as in OpenFCST were conducted with two turbulence models i.e, algebraic model and $k-\epsilon$ model. In the case of the algebraic model, the laminar flow physics is considered with the viscosity value changed to the desired turbulence viscosity value. In the other case, the turbulence model is set to the standard $k-\epsilon$ model and no further changes were done to viscosity. The different solver types considered are referred to with different abbreviation as in Table 3.2.

Fig. 3.10 shows the numerically predicted gauge pressure and velocity distribution in an empty tower at an input frequency of 60Hz using the OpenFCST solver. The pressure distribution shows a low-pressure zone at the inlet of the tower, while a gradual change is observed

Table 3.2 – Abbreviations used for different simulations

Simulation method	**Abbreviation used**
OpenFCST	OpenFCST
Ansys with algebraic	Ansys_algebraic
Ansys with $k-\epsilon$	Ansys_kepsilon

in the rest of the tower. The incoming high flow velocity causes this low pressure due to the sudden contraction in size and change in direction. The fluid stream cannot closely follow the sharp angle and hence results in a narrowing stream profile. Such a phenomenon gives rise to unequal distribution of flow stream resulting in a lower pressure drop region at the tower inlet.

As mentioned in the previous section, one of the main reasons to simulate a 3D model is to reduce the three-dimensional effects, which can be observed when the velocity profiles are analyzed at the central plane and an offset plane. Fig. 3.11 shows the velocity profile in the central plane (refer Fig. 3.8a for central plane and Fig. 3.8b for offset plane) and in the offset plane that is 0.3 m from the central plane. The colormap is kept the same in both cases to display the extent of variation. It is observed that both planes have similar profiles with greatly varying velocity magnitudes emphasizing the need for a 3D domain.

The velocity profile, in general, follows the trend as in the case of the 2D domain except that it varies along the inlet width. A significant portion of the flow is pushed towards the tower centre due to vena-contracta, and it assumes a laminar profile as it flows towards the exit. Due to the non-uniform distribution of the flow at the inlet, the lower pressure drop and some airflow downwards results in a recirculation zone at the inlet.

Ansys simulations

With the same boundary conditions, simulations are performed in Ansys with the algebraic turbulence model and with the $k-\epsilon$ turbulence model. The solution achieved with the algebraic model is shown in Fig. 3.12. It has a similar pressure distribution to that of the OpenFCST solution. In both cases, the velocity at the inlet is more concentrated towards the center of the tower due to convective effects. Eventually, the flow distributes across the tower cross-section. Since a constant viscosity is used for the whole domain, the predicted velocity profile in the tower appears laminar rather than turbulent.

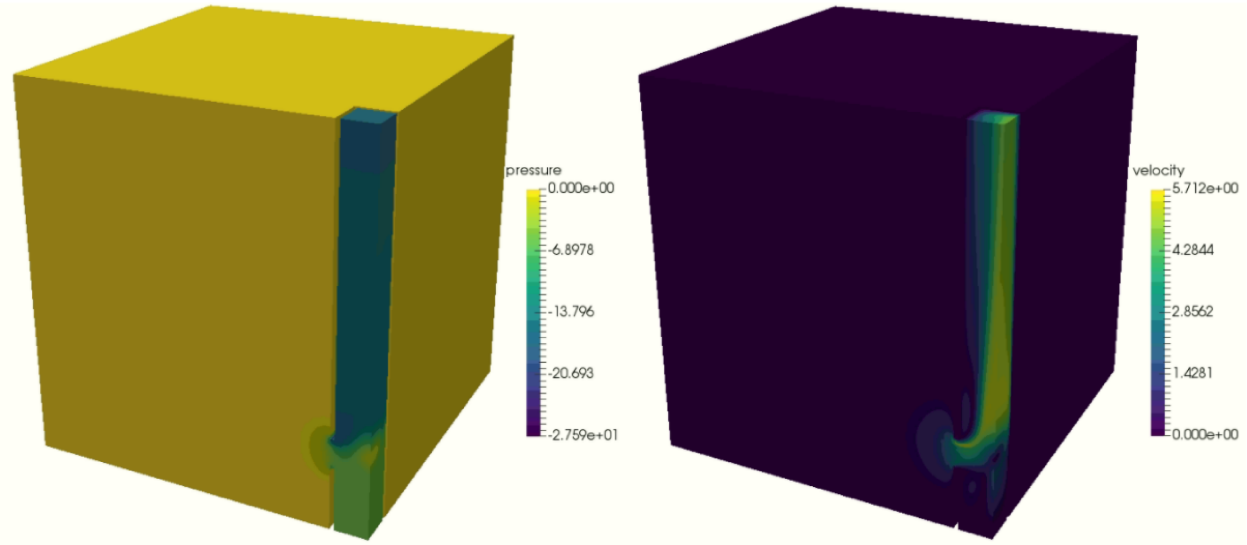

Figure 3.10 – Pressure(left) and velocity(right) distribution in an empty tower at an input frequency of 60Hz

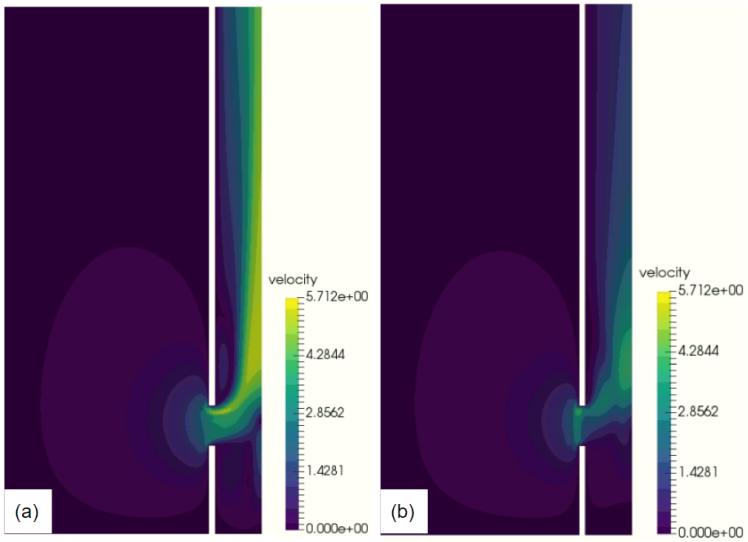

Figure 3.11 – (a) Velocity profile in the central plane (b) Velocity profile in the offset plane at a distance of 0.3 m from the central plane towards the side wall of the tower

The solution achieved in Ansys using the k-epsilon model is shown in Fig. 3.13. The pressure in the tower has a similar distribution to the algebraic model; however, the low-pressure zone at the tower inlet is dominantly visible, extending to almost half the tower height. Due to the high velocities, the flow entering the tower is pushed towards the center and the sidewall as it flows downstream. This effectively creates the low-pressure region at the tower inlet, making some amount of airflow downwards. The recirculation zone is critical in all mechanical cooling towers as most towers have a similar geometrical configuration. Louvres

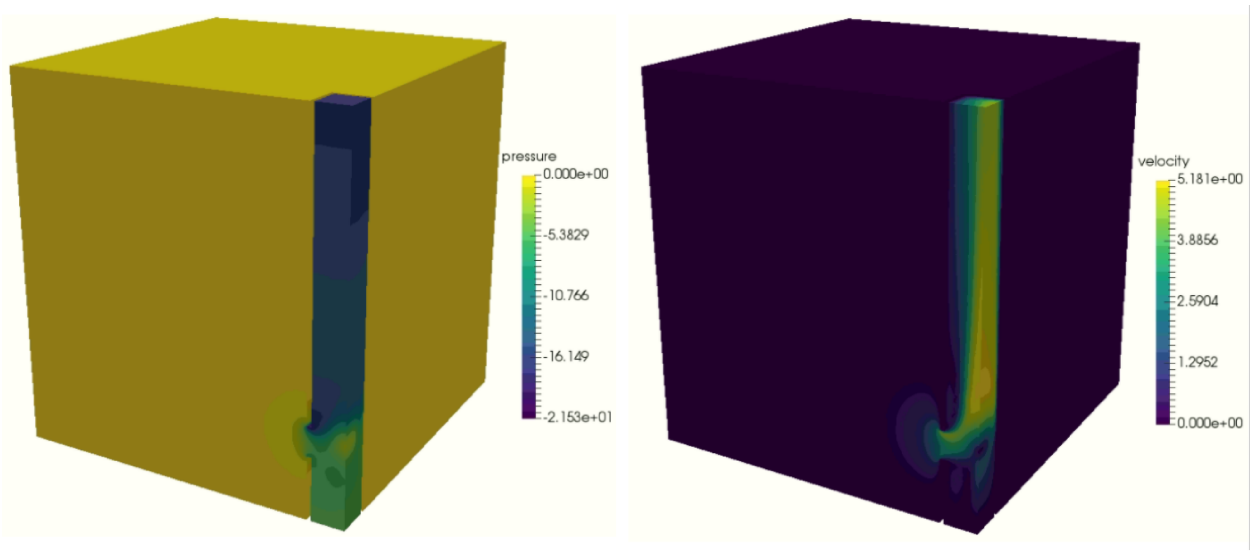

Figure 3.12 – Pressure(left) and velocity(right) distribution in an empty tower at an input frequency of 60Hz obtained from Ansys with algebraic turbulence model

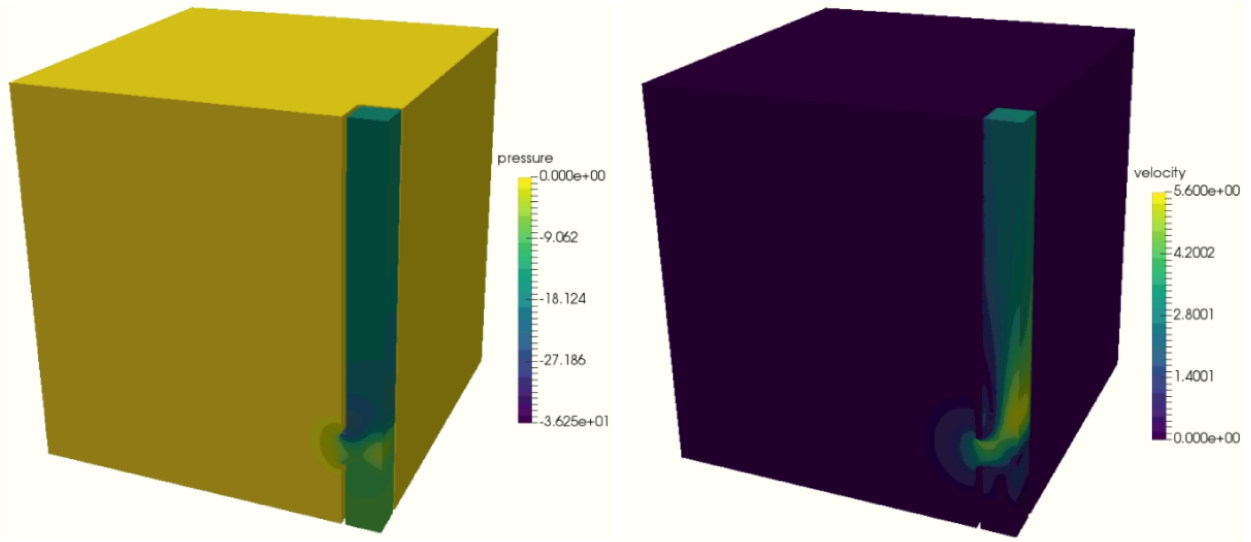

Figure 3.13 – Pressure(left) and velocity(right) distribution in an empty tower at an input frequency of 60Hz obtained from Ansys with $k - \epsilon$ turbulence model

are therefore present to modulate airflow into the tower. The louvres in a cooling tower act as a barrier for sunlight, noise, water splash-out and debris while also improving the airflow of the cooling tower.

The k-epsilon model, however, has a different velocity distribution as compared to the algebraic models (both OpenFCCST and Ansys). Contrary to the laminar profile, the flow seems to have achieved a uniform velocity in the tower domain before the tower exit. Such a

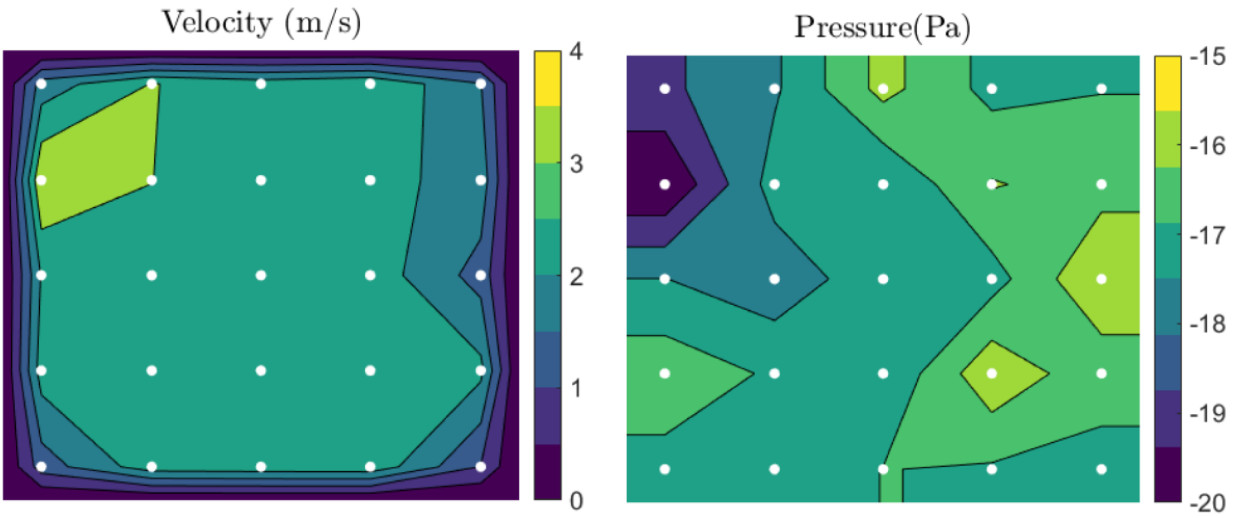

Figure 3.14 – Experimental velocity (left) and pressure (right) profiles in the plenum plane for 60 Hz input frequency

variation is observed owing to the presence of the wall-treatment in the k-epsilon turbulence model. The wall gives rise to a boundary layer, where the velocity changes from the no-slip condition at the wall to its free stream value. The variation is usually most significant in the near-wall region, and hence the most substantial gradients are found here, which are modelled using a standard wall function. The turbulent effects inside the tower dominate such that they force the flow to attain a uniform value in the free-stream, which is not the case with the algebraic model. The pressure has the expected distribution; however, the low-pressure region is much higher, owing to turbulent effects that eventually result in higher resistance at the inlet.

Comparison with experiments

The experimental values measured over a cross-sectional area are plotted over as surface data for better visualization. For an input frequency of 60Hz, the measured velocity and pressure distribution at the plenum plane are shown in Fig. 3.14. The white dots in the figure are the measuring points for which the data is available. The surface data is extended to the wall for both velocity and pressure profiles. The velocity value at the wall is kept at zero, while for pressure, the value of the nearest data point is considered. For example, at each corner, the pressure value of the closest corner data point is taken. The velocity is uniform for the significant portion of the cross-section; however, it is not as uniform as expected considering a fully turbulent regime. The pressure distribution does not follow any particular pattern emphasizing the turbulent nature of the flow, giving rise to fluctuations.

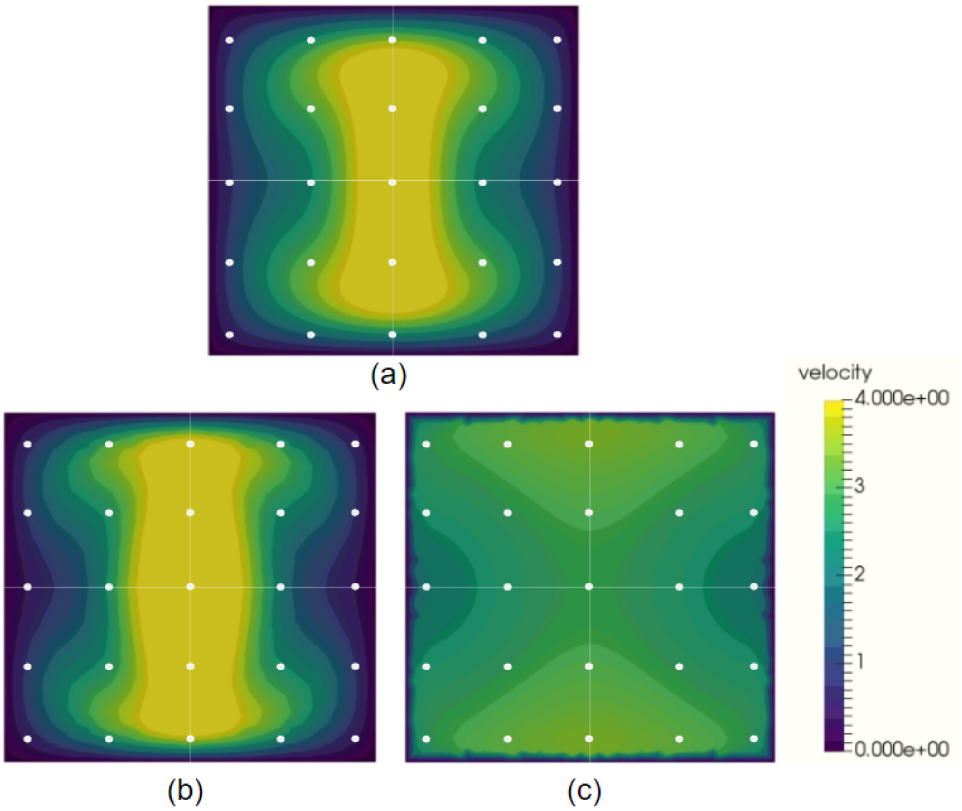

Figure 3.15 – Velocity distribution in the plenum plane obtained for (a) OpenFCST (b) Ansys_algebraic (c) Ansys_kepsilon

The velocity distribution at the plenum plane obtained from simulations is as shown in Fig. 3.15. The solution is obtained for only a quarter part of the cross-section. Utilizing symmetry, the solution can be visualized in the remaining quarters. The white dots in the plots are provided to show the experimental data points.

OpenFCST and Ansys_algebraic simulations have a similar velocity distribution. On the other hand, the experimental distribution is more uniform as would be expected in a turbulence regime. This is the drawback of using an algebraic model. At high Re, convection dominates, resulting in an almost uniform flow across the cross-section with a steep gradient at the wall. The Ansys_kepsilon model provides a more uniform profile with values close to the experimental distribution.

The pressure comparison at the plenum plane is shown in Fig. 3.16. The pressure prediction at this plane is as expected as a pressure boundary condition is applied at the outlet. In all the simulated cases, the pressure in the plenum plane is close to the measured value.

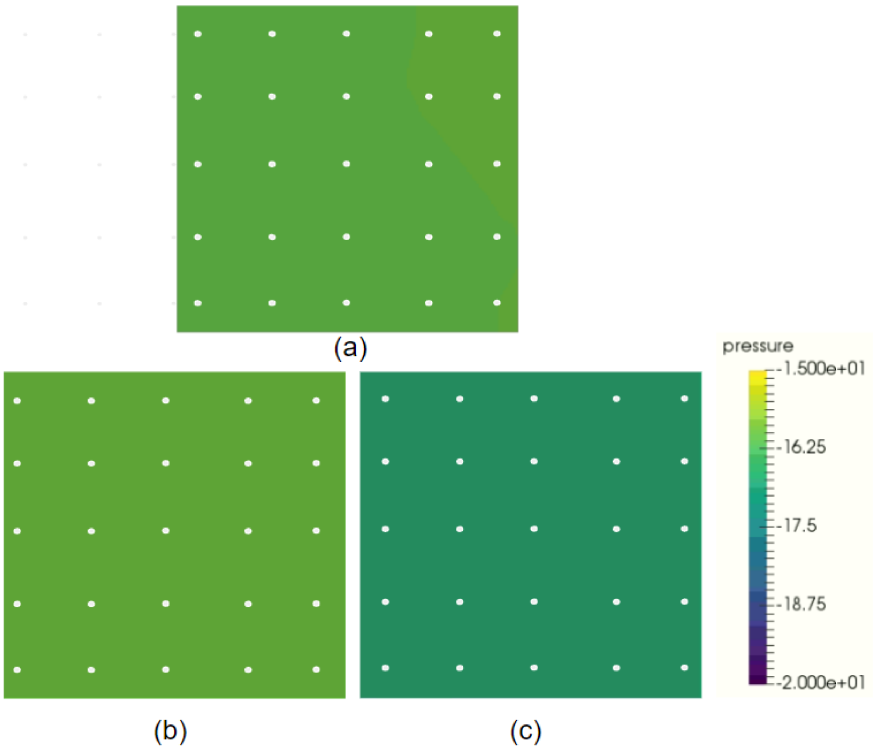

Figure 3.16 – Pressure distribution in the plenum plane obtained for (a) OpenFCST (b) Ansys_algebraic (c) Ansys_kepsilon

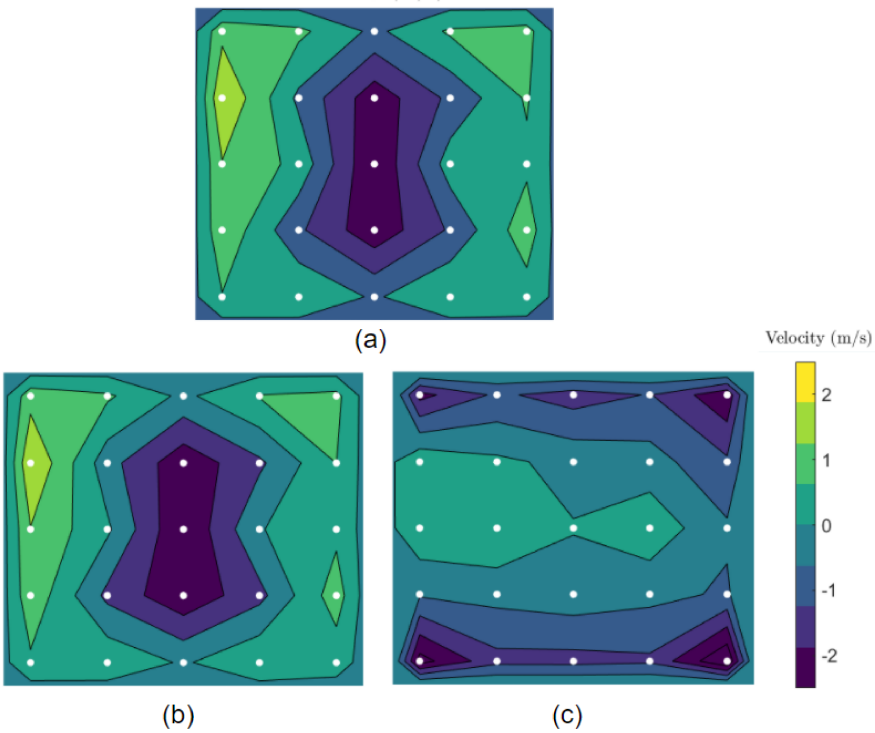

Figure 3.17 – Plenum plane velocity difference plots. Difference of experimental data to (a) OpenFCST (b) Ansys_algebraic (c) Ansys_kepsilon

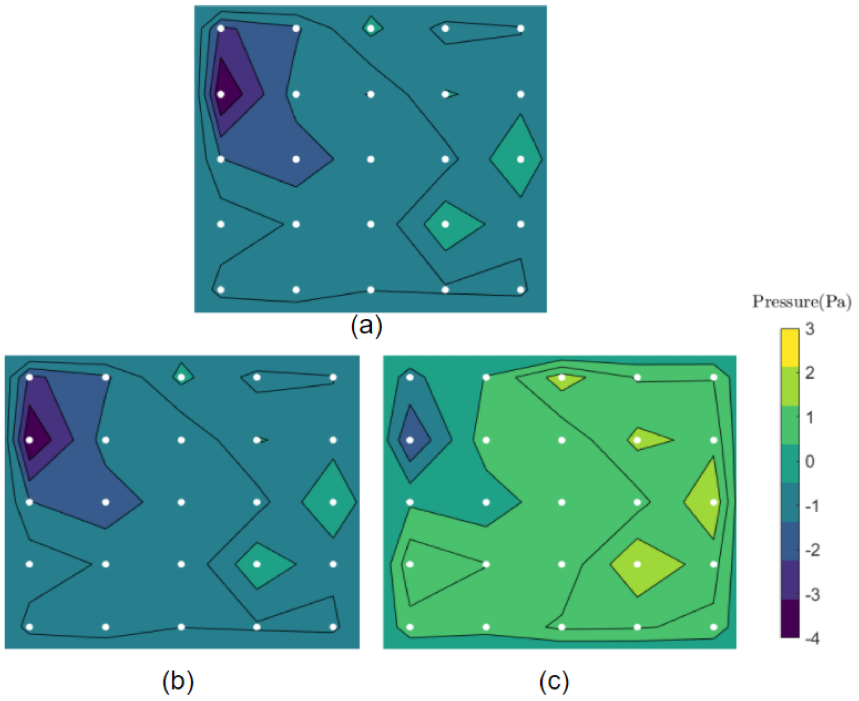

Figure 3.18 – Plenum plane pressure difference plots. Difference of experimental data to (a) OpenFCST (b) Ansys_algebraic (c) Ansys_kepsilon

To better visualize the differences between the numerical prediction and experimental data, the difference between simulation and experimental data is plotted for the velocity and the pressure at the plenum plane. Fig. 3.17 shows the difference in velocity between either OpenFCST or Ansys and the experimental data. As observed from the distribution plots, OpenFCST and Ansys_algebraic have similar difference plot distribution with the differences in the central plane in the range of 2 m/s, which is very significant considering the average velocity measured is 2.58 m/s. Fig. 3.18 shows the differences between the numerical and experimental pressure distribution. As discussed, a close agreement is observed.

The flow in the tower achieves uniformity towards the exit, due to which the simulation results in the plenum plane do not show much variation from the experimental data. However, the flow at the inlet undergoes a drastic change both in direction and magnitude and is also critical in shaping the flow downwards. In this regard, comparing the flow variables in the rain plane (see Fig. 3.1) helps in better validation of the solvers. Fig. 3.19 shows the variation of the experimental velocity and pressure profiles measured in the rain plane. The velocity in the cross-section is negative near the inlet, suggesting the presence of a recirculation region. The magnitude of the flow velocity increases towards the tower's center, and the highest magnitude is experienced in the central plane. Due to the recirculation, a

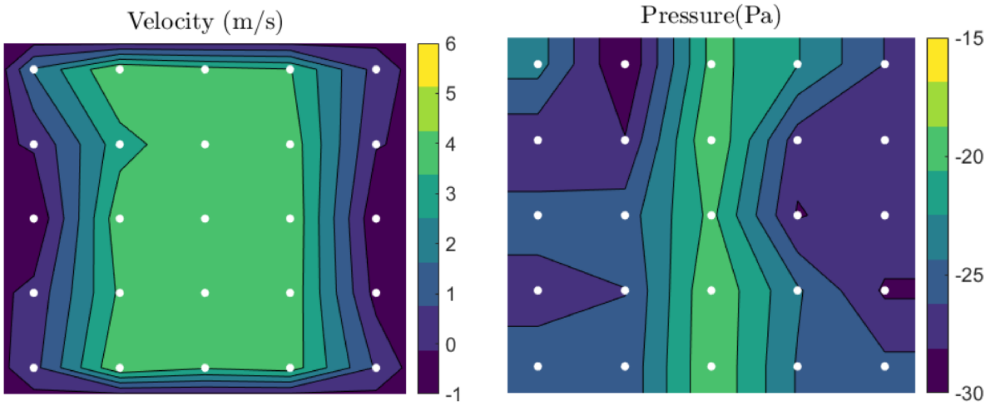

Figure 3.19 – Experimental velocity(left) and pressure(right) profiles in the rain plane for 60Hz input frequency

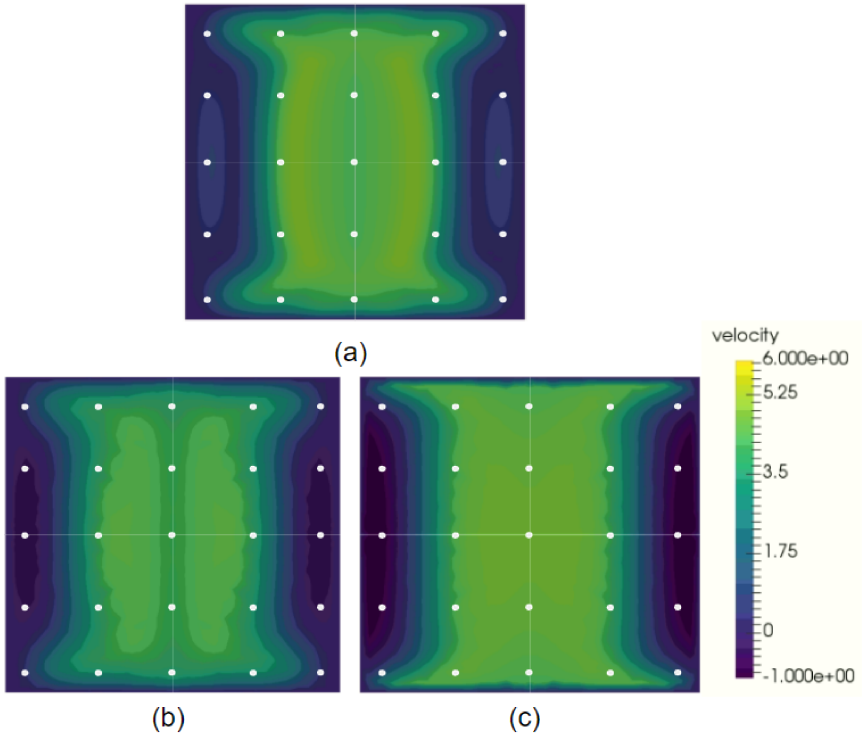

Figure 3.20 – Rain plane velocity distribution (a) OpenFCST (b) Ansys_algebraic (c) Ansys_kepsilon

low-pressure zone is experienced in the tower inlet, and the pressure is steadily increased towards the tower center. Fig. 3.20 shows the velocity profile at the rain plane for different simulations.

Fig. 3.21 shows the pressure profile distribution at the rain plane for different simulations. The pressure close to the wall is lower and gradually increases towards the tower's center

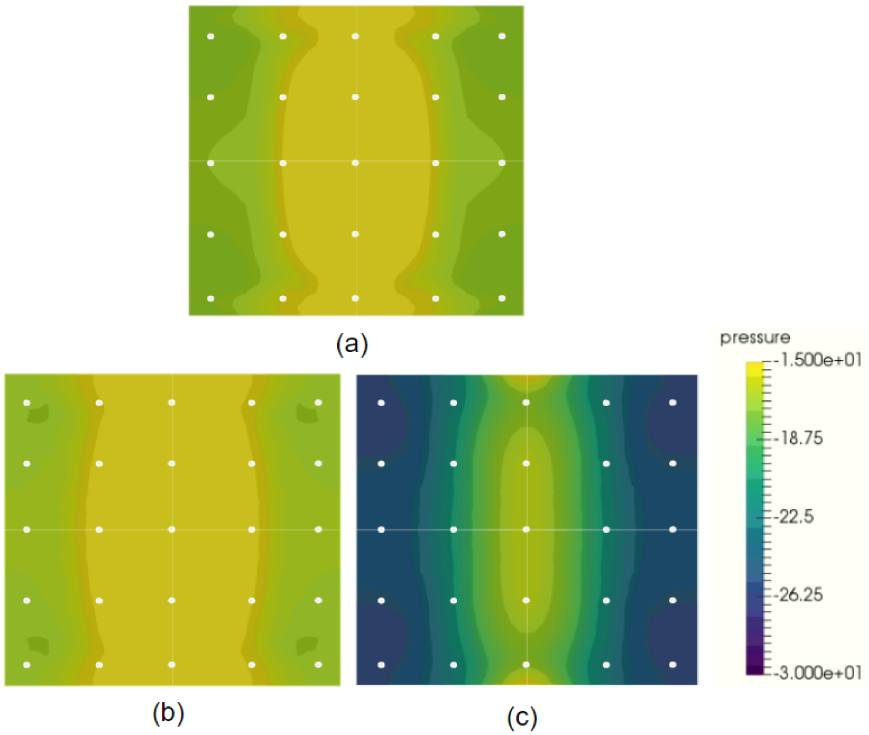

Figure 3.21 – Rain plane pressure distribution (a) OpenFCST (b) Ansys_algebraic (c) Ansys_kepsilon

due to the higher dynamic pressure. While OpenFCST and Ansys_algebraic show a similar range in the difference, Ansys_kepsilon shows a much larger variation. It is noted that RANS models, including the $k-\epsilon$ turbulence model, cannot predict the turbulent intensities due to their limitations at higher Reynolds numbers [47]. Such a case becomes dominant when there is a separation of flow in the domain [48]. In order to assess the range of difference for each case, the difference of velocity and pressure are plotted in Fig. 3.22 and in Fig. 3.23 respectively.

From the difference plots, it is observed that there are significant differences between the simulation results and experimental results, more so in the case of Ansys_kepsilon. However, the extent of deviation is unknown, making it challenging to decide on the best solver. Hence, a parameter is defined that evaluates the deviation of the simulation from the experiments called an error parameter (Er). It is defined as the square root of the sum of the squared of the difference at each grid point, divided by the total number of grid points.

$$Er = \frac{\sqrt{\sum_{i=1}^{i=25} (EX_i - SX_i)^2}}{N} \tag{3.1}$$

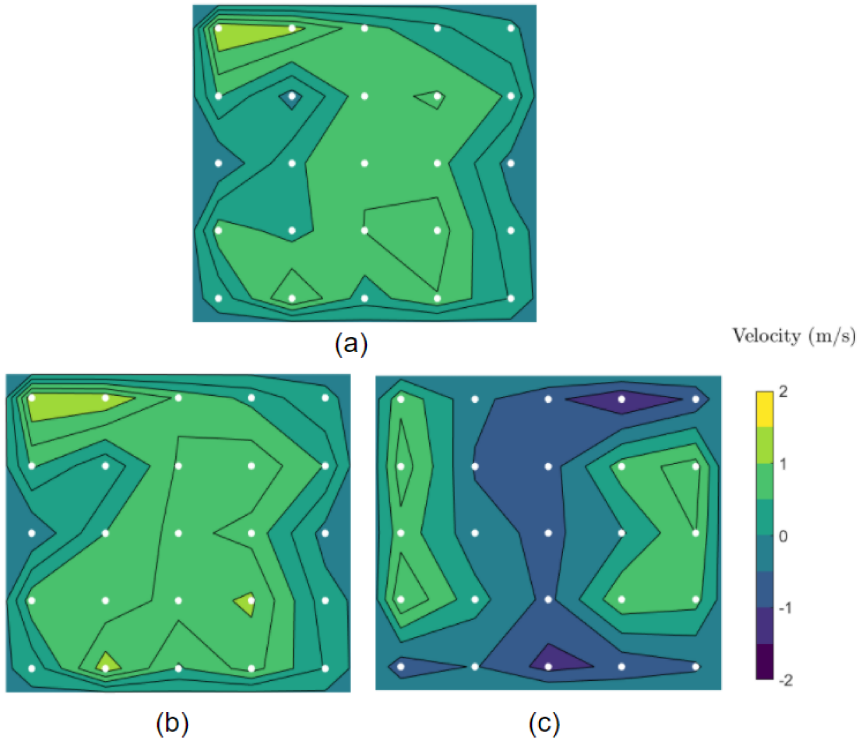

Figure 3.22 – Rain plane velocity difference plots. Difference of experimental data to (a) OpenFCST (b) Ansys_algebraic (c) Ansys_kepsilon

where EX_i is the experimental data at the ith grid point, SX_i is the simulation data at the ith grid point and N is the total number of grid points. Smaller the value of the error parameter, smaller is the deviation of the solver results from the experimental data. For this, the pressure and velocity distribution for the plenum plane and rain zone plane are considered. The error parameter for velocity and pressure is evaluated for both planes and is shown in Table 3.3. It is observed that OpenFCST and Ansys_algebraic have lower values while Ansys_kepsilon has higher value of error parameter.

The mass flow rate obtained by integrating over the cross-sectional area is also compared for each solver as shown in Fig. 3.24. The plot shows that OpenFCST and Ansys_algebraic provide closer predictions to the experimental results than the Ansys_kepsilon model. The $k-\epsilon$ turbulence model under-predicts the momentum diffusion as in the current case, the turbulent diffusion is considered isotropic, which in 3D may become anisotropic, i.e., the turbulence viscosity is different in different directions and has to be considered as a tensor instead of a scalar. As a result, a more extended recirculation zone is observed, resulting in a much lower pressure drop at the inlet than the experimental data. The resulting flow distribution, in turn, results in a different mass flow rate at the exit as observed from Fig.

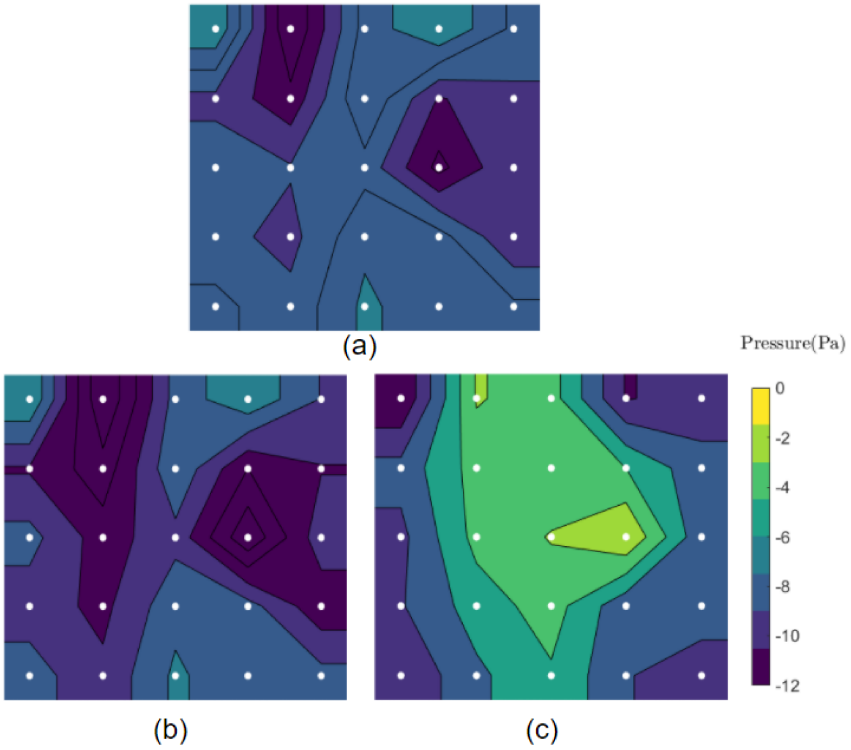

Figure 3.23 – Rain plane pressure difference plots. Difference of experimental data to (a) OpenFCST (b) Ansys_algebraic (c) Ansys_kepsilon

Table 3.3 – Error parameter evaluated at different planes

	Error parameter (Er)
Plenum pressure (OpenFCST/Exp)	2.429377e-01
Plenum pressure (Ansys_algebraic/Exp)	2.520445e-01
Plenum pressure (Ansys_kepsilon/Exp)	2.762858e-01
Plenum velocity (OpenFCST/Exp)	2.374392e-01
Plenum velocity (Ansys_algebraic/Exp)	2.296034e-01
Plenum velocity (Ansys_kepsilon/Exp)	2.253912e-01
Rain pressure (OpenFCST/Exp)	5.951192e-01
Rain pressure (Ansys_algebraic/Exp)	6.603898e-01
Rain pressure (Ansys_kepsilon/Exp)	2.682249e+00
Rain velocity (OpenFCST/Exp)	3.564314e-01
Rain velocity (Ansys_algebraic/Exp)	3.481984e-01
Rain velocity (Ansys_kepsilon/Exp)	4.965775e-01

3.24. OpenFCST and Ansys_algebraic predicted the recirculation zone and were in closer agreement with the experimental data. Hence an algebraic turbulence model is used in future simulations unless specified otherwise.

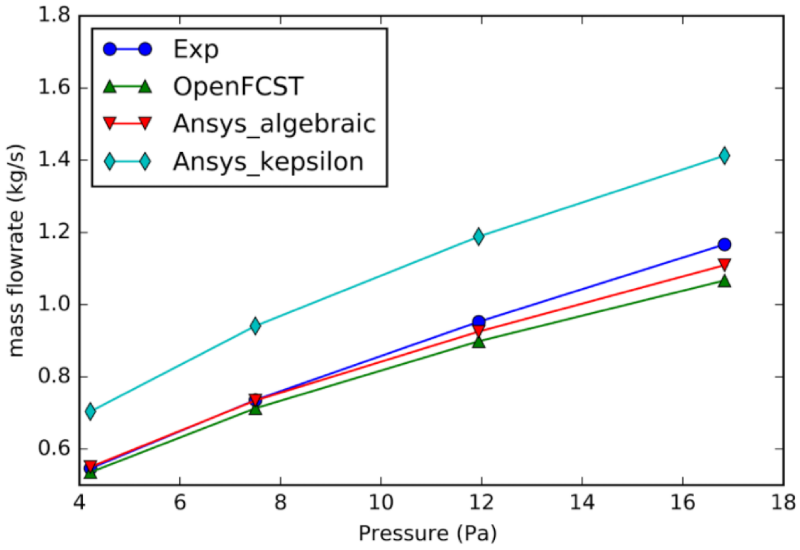

Figure 3.24 – Mass flowrate variation with outlet pressure for different solvers

3.2 Tower with fill - 2D

The incompressible solver with an algebraic model and porous media formulation was first considered to simulate the cooling tower with fill. Simulations resulted in poor convergence due to numerical limitations, which are described in Appendix B

In general, both compressible and incompressible formulations have been utilized in literature to simulate the flow in porous media. The presence of fill gives rise to pressure variation, which in turn results in density variation, especially in the closed flow, as in the case of the cooling tower. The change in density may be less, but it is necessary to incorporate the compressible behaviour of the gases to accommodate the mass conservation in the domain. Santamaria et al. [49] emphasized the importance of using a compressible fluid flow model that forces the gas through porous media. Additionally, the incompressible formulation might underestimate the permeability value of the porous media [50, 51]. Jarauta et al. [38] showed that compressible formulation for an appropriate velocity/density pair provides a continuous and stable solution. The compressible formulation is also validated with the Experimental data in Mangal et al. [52], and Xu [53]. Cooling tower simulations with porous media in the past have considered compressible formulations as it is suitable to accommodate any changes in the air density due to heat and mass transfer [6, 31]. Due to the above reasons, and lack of convergence and incorrect pressure observed (Appendix B) with the incompressible solver, a compressible formulation, implemented in OpenFCST and validated in ref [38] is considered.

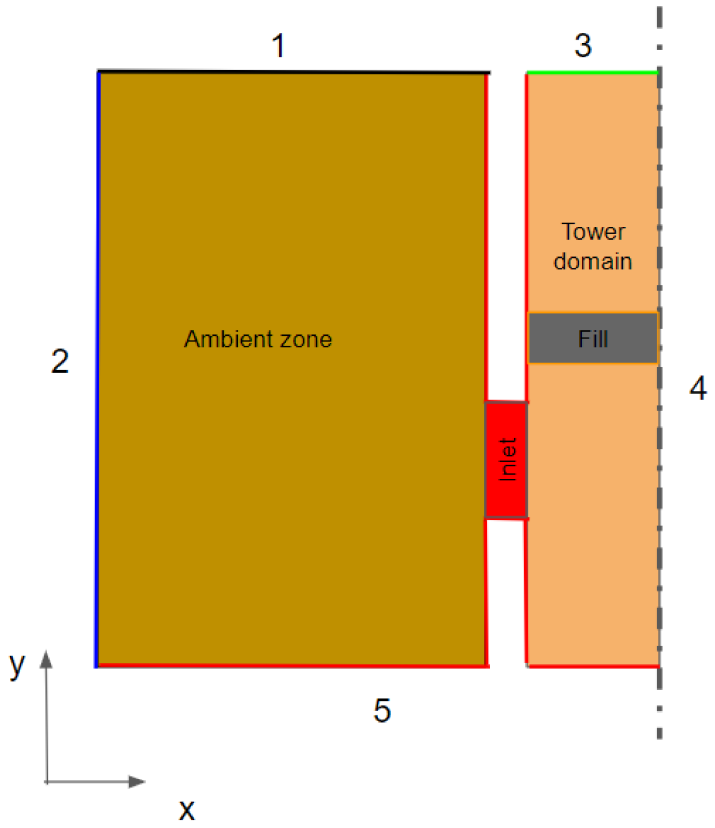

Figure 3.25 – 2D domain with fill

In the numerical model, a two feet fill is installed in the domain as shown in Fig. 3.25 while keeping all the other dimensions the same as of the empty tower. Experiments were performed with this setup, and the pressure at the plenum plane was recorded. The pressure drop values are listed in Table 3.4. For further computation, an estimation of the fill permeability is required. The resistance offered by the fill can either be modelled as linear, resulting in a dominant viscous force or quadratic, resulting in a dominant inertial force. Both of these terms are implemented in the solver; however, it is necessary to know which term is dominant to make the final choice on the permeability value.

Since fill is considered a porous media, the said permeability of the fill can be multi-dimensional and different along with different directions. In general, air flows from the bottom of the fill towards the top of the fill and, therefore, a single permeability value along Y-direction is considered for parametric study. Since there is no net flow along the X-direction in the fill, the permeability in this direction is approximated as a small number (ideally, it is zero, but such a value can result in a computational error).

Table 3.4 – Pressure drop measurement for two feet fill height

Average velocity (m/s)	Pressure drop (Pa)
2.54	33.7
2.16	22.8
1.73	15.0
1.13	8.60

Table 3.5 – Pressure drop measurement for four feet fill height

Average velocity (m/s)	Pressure drop (Pa)
2.22	56.50
1.91	41.57
1.53	26.93
1.23	16.34

To estimate the permeability value (k), simulations are performed at moderate velocity with multiple values of permeability and the pressure prediction is noted. The obtained pressure is then compared to one of the experimental data points. The value of the permeability which matches with the experimental data is then used to estimate the pressure at other data points. In case, the considered value provides a good prediction at the other data points, it can be used for future simulations to predict the pressure drop. However, the experimental data point with which the predicted pressure is matched should be considered carefully. An extreme data point should be avoided as it may result in extrapolation issues. Therefore, in the current study, the data point corresponding to the average flow rate of 1.7 m/s is considered.

A parametric study is performed on the permeability value as shown in Fig. 3.26a where Darcy's estimation is used for the pressure prediction for the two feet fill. The fill permeability value of 0.5 cm^2 results in good agreement with the experimental data and is then used to predict pressure for other data points as shown in Fig. 3.26b. This value, however, deviates significantly in predicting the pressure drop for a four feet fill (data in Table 3.5) as shown in Fig. 3.26c.

At high velocity, inertial effects might dominate, and, as a result, the fill model is extended to include inertial effects by adding a Forchheimer term (Eq. 2.24). A new parametric study is performed using the updated model to include the inertial effects to obtain the fill permeability value for pressure prediction. The same set of data for the two feet fill and four feet fill is considered. A permeability value of 230 cm^2 was obtained, which has a good prediction with the experimental data of both two and four feet high fills. The results are

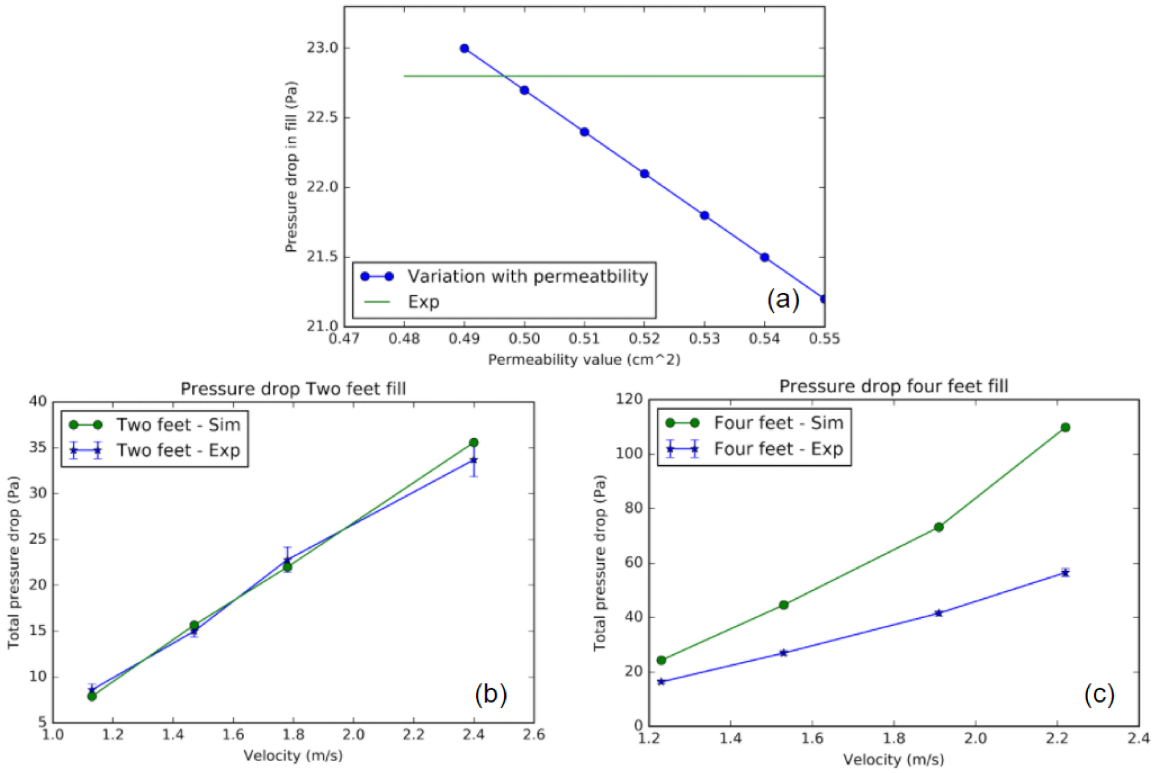

Figure 3.26 – (a) Parametric study on permeability value using the Darcy's estimation for pressure drop (b) pressure drop obtained at k=0.5 cm^2 for 2 feet fill (c) pressure drop obtained at k=0.5 cm^2 for 4 feet fill

shown in Fig. 3.27 highlight the importance of the inertial term in order to achieve accurate predictions of pressure drop across the fill. This value of permeability of the fill is achieved by considering the overall pressure drop in the tower rather than just the pressure drop across the fill.

The velocity and pressure distribution inside the tower with fill are as shown in Fig. 3.28. As seen in previous simulations, a lower pressure zone is observed at the tower inlet, giving rise to a recirculation zone. With the introduction of fill in the tower, the flow redistributes itself in the rain zone, and the recirculation zone is suppressed. While the flow in the rest of the domain remains similar, the flow in the rain zone drastically changes with the introduction of the fill. It, however, has a maximum velocity entering the tower but quickly redistributes to allow the flow to spread uniformly across the cross-section before the fill inlet. The fill, thus, influences the flow profile, which emphasizes the critical nature of the flow behaviour in the rain zone. However, the uniformity of the flow is not fully achieved, and some non-uniformity is present before entering the fill inlet. The flow maintains the same distribution throughout the fill and results in a flow distribution similar to that of a channel flow.

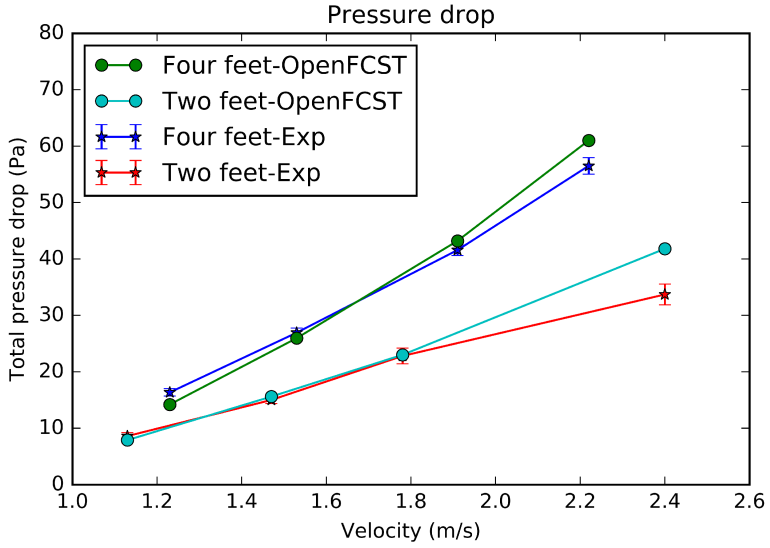

Figure 3.27 – Pressure drop comparison with experimental data at k=230 cm^2

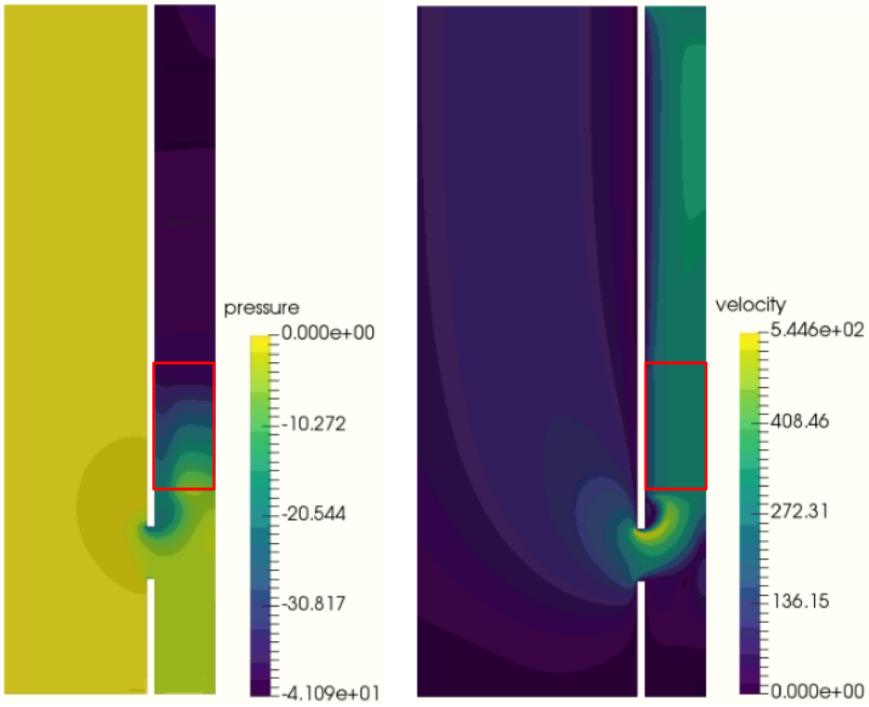

Figure 3.28 – Pressure (left) and velocity (right) distribution for an average velocity of 2.54 m/s in the tower with 2 feet fill

Two critical regions in the tower significantly contribute to the pressure drop: 1) tower inlet region extending until the fill inlet and 2) fill region. The tower inlet has a low-pressure region, arising due to a vena-contracta, resulting in an uneven distribution of flow across the

tower cross-section. The pressure drop observed at the tower inlet starts to recover as the flow tends to become uniform. However, due to the presence of the fill, full recovery does not happen and, hence, an inherent pressure loss is always observed that contributes towards the overall pressure drop.

By construction, the fill consists of a solid component that offers resistance to the fluid flow. In the current study, the permeability is defined along the vertical direction only. The permeability in the horizontal direction is considered a minimal value, indicating a high resistance to the flow and, therefore, imposing a no-flow condition. The flow adjusts itself before entering the fill and maintains a uniform flow across the fill. Due to uni-directional permeability along the vertical direction, a gradual pressure drop is observed across the fill as shown in Fig. 3.28.

Assuming the porous media as a bed of spheres of uniform diameter D_p, the Kozeny-Carman equation can be used to estimate the size of the particles

$$D_p = \sqrt{180 \frac{(1-\varepsilon)^2}{\varepsilon^3} \frac{k}{\phi^2}} \tag{3.2}$$

where ε is the porosity, ϕ is the sphericity of the particle [54]. With the obtained permeability of 230 cm^2, $\varepsilon = 0.975$ and considering ϕ to be unity, the diameter of the spherical particle is estimated to be 5.61 cm. It indicates that a bed of spherical particles with a uniform diameter of 5.21 cm results in 230 cm^2. Such an analogy fits better in considering a fluid flow across a bed of sand particles. The equation above is developed assuming regular shapes like spheres or cylinders as solid objects. In contrast, in fill, the solid objects are either sheets or wire-like grills, which may not be co-related to a specific object type. Additionally, the equation is applicable at low Reynolds numbers. So Darcy's law is applied for the pressure drop, while in the case of cooling towers, the flow regime is turbulent, and the Konzeny-Carman equation may not provide a good estimation of the shape of the fill.

3.2.1 Parametric studies

It is observed that by introducing the fill in the tower, the flow behaviour is significantly affected. In addition to being a source of pressure loss, the fill also straightens the flow. Therefore, it is imperative to understand the extent of the influence of the fill on the flow behaviour. Studies are conducted with varying fill height and fill location in the tower to understand the extent of the influence of the fill on pressure drop. The fill height (H) is varied in the tower while the airflow rate is kept constant with an average velocity (u_{avg})

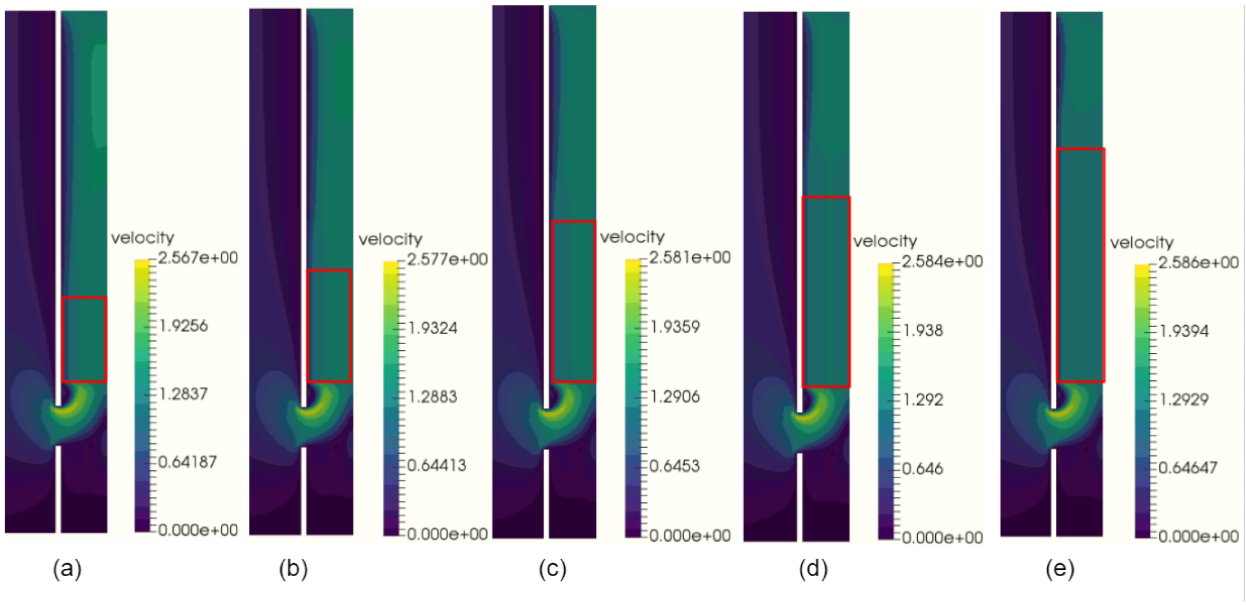

Figure 3.29 – Velocity profiles for u_{avg} = 1.20 m/s are different fill height (a) 2 feet (b) 3 feet (c) 4 feet (d) 5 feet (e) 6 feet

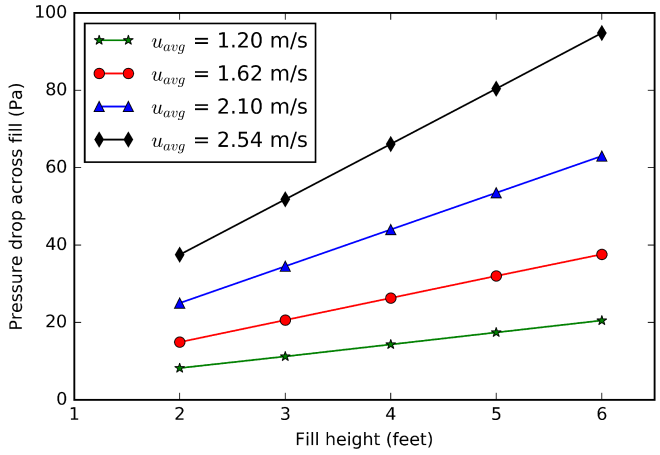

Figure 3.30 – Pressure drop variation with fill height at different velocities

of 1.20 m/s, and the obtained velocity profile is shown in Fig. 3.29. The velocity profile in the domain is similar at the tower inlet region in all the cases, with a minor variation in maximum velocity value. After passing through the fill, the flow tries to acquire a uniform profile as it exits the tower.

As mentioned in the previous section, two major pressure drop zones are present in the tower. To better estimate pressure drop across the fill, the difference of pressure values obtained across the fill is evaluated. The pressure profiles at the fill inlet and the fill outlet are consid-

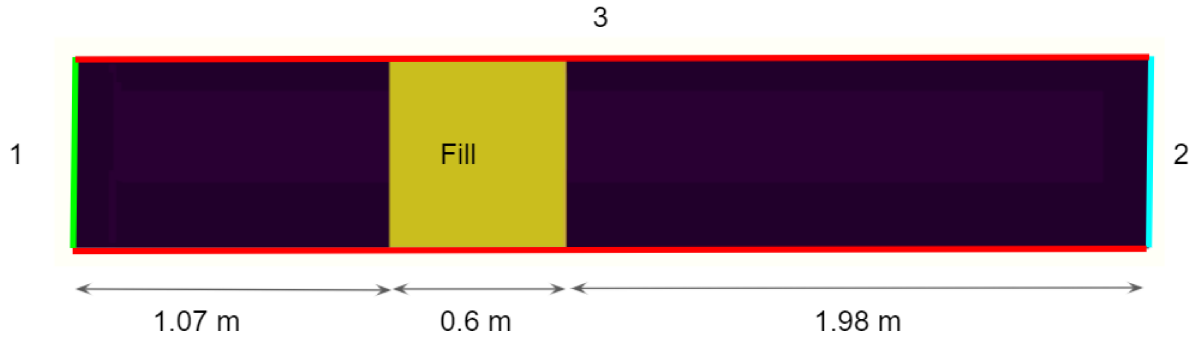

Figure 3.31 – Chanel domain with porous media inside and width equal to ESDLab tower, i.e., 0.645 m

ered for which the average values are evaluated, and subsequently, the difference is calculated.

The pressure drop increases with the fill height as shown in Fig. 3.30 and is observed to have a linear relation with the fill height. The magnitude of pressure drop in a tower is highly dependent on the fill height and the flow rate. The higher the fill height, the longer the path travelled by the flow inside the fill, resulting in a more significant pressure drop.

It has been observed experimentally that the pressure drop across the fill changes with its location inside the tower [3]. The predicted pressure drop obtained when fill placed close to the inlet is different to the pressure drop obtained when fill is placed far away from the inlet. The discrepancy in the results was hypothesized to be of the proximity of the fill to the inlet, which is studied with the help of numerical analysis.

To understand the inlet effects on the pressure drop across the fill, two types of simulations are conducted. In one case, a channel is considered as shown in Fig. 3.31 is considered, and in the other case, the ESDLab tower is considered with inlet and fill placed at different locations. IN the channel simulations, the air enters from one end of the channel (boundary ID 1) and leaves at the other end (boundary ID 2) with a fill in-between in the channel. Such a setup provides the actual pressure drop across the fill without any inlet effects. The fill is also initially placed close to the inlet (normal) and is gradually moved inside the tower by 1 foot each time, and the obtained pressure drop across the fill is noted. The obtained pressure with channel and the ESDLab tower with inlet is plotted in Fig. 3.32a.

The pressure drop across the fill in the channel simulations represents the actual pressure drop in the fill as it is not influenced by any flow related parameters. Fig. 3.32a shows that

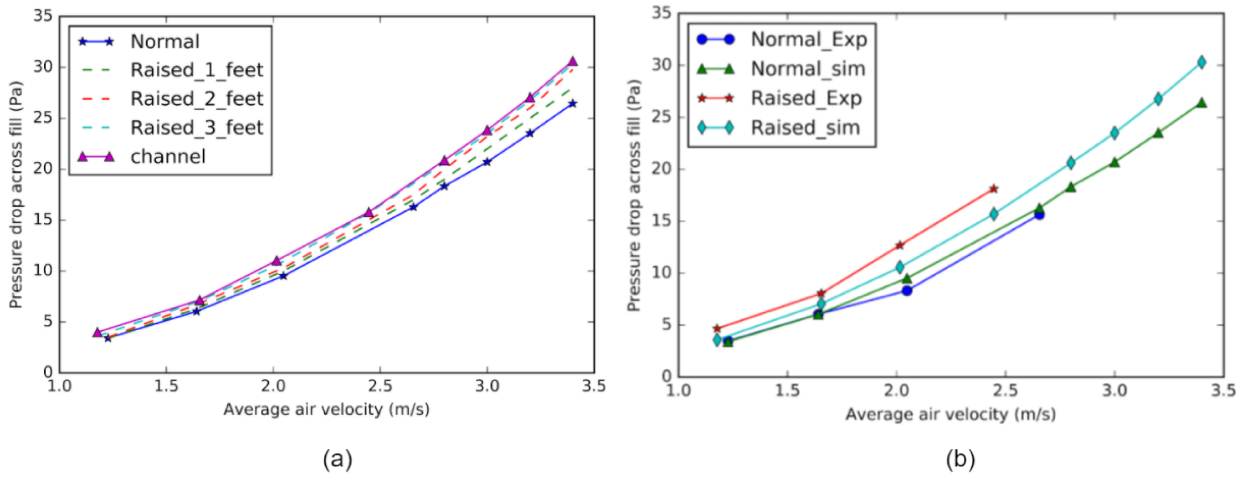

Figure 3.32 – (a) Pressure drop across fill in channel and in ESDLab tower with varying fill location (b) ESDLab pressure drop comparison with the experimental data - 2 feet fill, k=600 cm^2

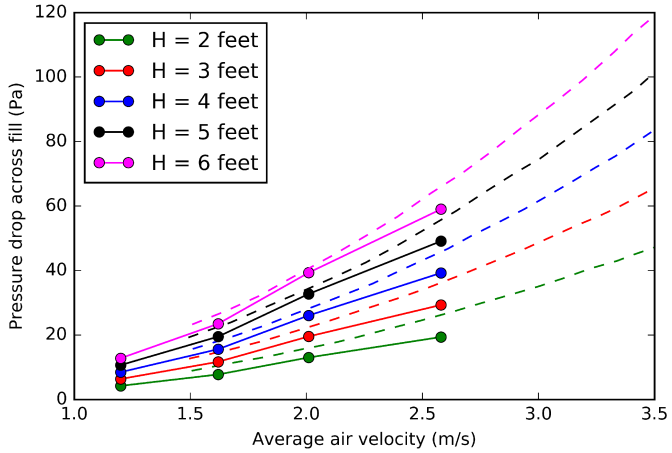

Figure 3.33 – Pressure drop comparison with the manufacturer's data. Solid lines indicate the simulation results and dashed lines indicate the manufacturer's data. k=500 cm^2

the pressure drop in the normal position is affected by its proximity of the inlet resulting in a lower pressure drop across the fill as compared to that of the channel case. When the fill moves upwards in the tower, the extent of the inlet effects reduces, resulting in an increased pressure drop reaching a similar value of pressure drop to that of channel simulation. With the fill raised by 3 feet inside the tower relative to the normal position has a closer pressure drop to that of the fill as in this case, the recirculation zone almost ends before it reaches the fill.

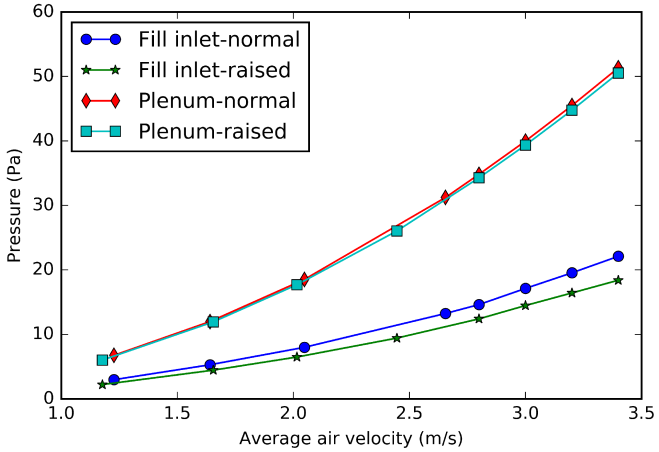

Figure 3.34 – Pressure at fill inlet plane and plenum plane k=600 cm^2

Following the study, the simulation results were compared with the experimental data of the ESDLab tower for the normal and raised positions of the fill as shown in Fig. 3.32b. The fill permeability value is calibrated using the normal position data. The obtained pressure drop for the normal position with the calibrated model can reproduce the experimental data. Pressure drop across the fill for the raised position is increased but is slightly lower than that of the experimental data. The difference between the pressure drop of normal (green color line in Fig. 3.32b) and raised (light blue color line in Fig. 3.32b) positions increases with increasing flow rates, implying that the inlet effects increase with the airflow rate into the tower.

The fill permeability value of 600 cm^2 still cannot match exactly with the experimental data in the raised position. Hence, to better compare with the manufacturer's data, the fill permeability value is again calibrated to the raised position of the fill, which comes out to be 500 cm^2. With the permeability value of 500 cm^2, the pressure drop obtained in the channel should be the pressure drop just across the fill without any inlet effects calibrated with ESDLab experimental data. The obtained pressure drop across the channel at different fill heights and airflow rates is compared with the manufacturer's data of the fill as shown in Fig. 3.33. The predicted pressure drop is lower in comparison with manufacturer's data with an offset value for all the simulations. Since the inlet information is not available for the manufacturer's data, it may be a probable reason for discrepancies in the results between the two as the numerical model has no inlet effects.

As mentioned earlier, another region that has largely contributed towards the pressure drop is the inlet region. Fig. 3.34 shows the pressure drop at the inlet plane and the plenum

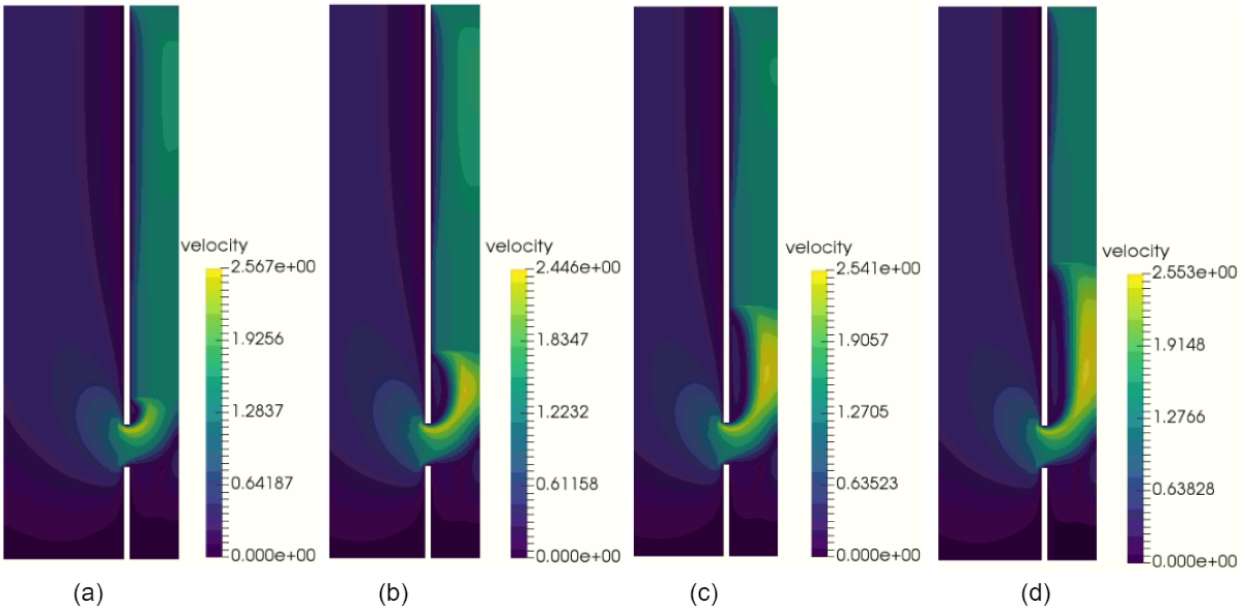

Figure 3.35 – Velocity profiles at u_{avg} = 1.20 m/s at different fill locations (a) 0.5 ft, (b) 1.5 ft (c) 2.5 ft (d) 3.5 ft

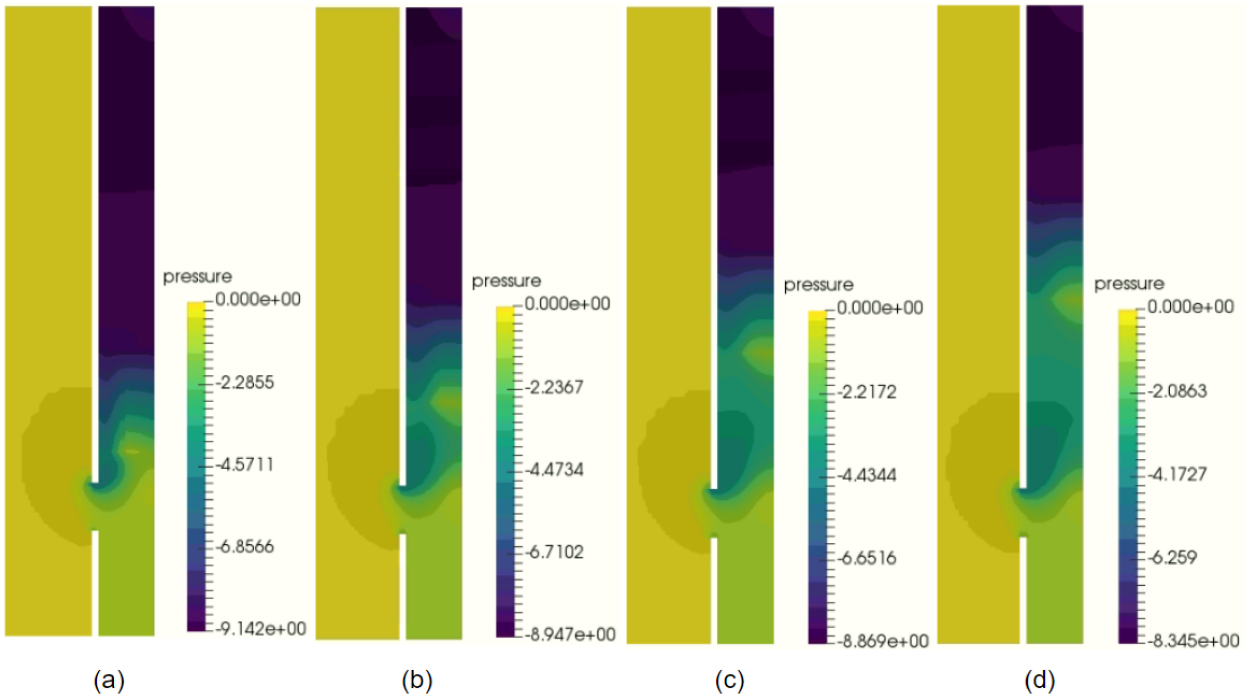

Figure 3.36 – Pressure profiles at u_{avg} = 1.20 m/s at different fill locations (a) 0.5 ft, (b) 1.5 ft (c) 2.5 ft (d) 3.5 ft

plane (overall pressure) for both normal and raised positions of the fill. The pressure drop increases with the velocity in the tower, and the inlet region is observed to have a significant

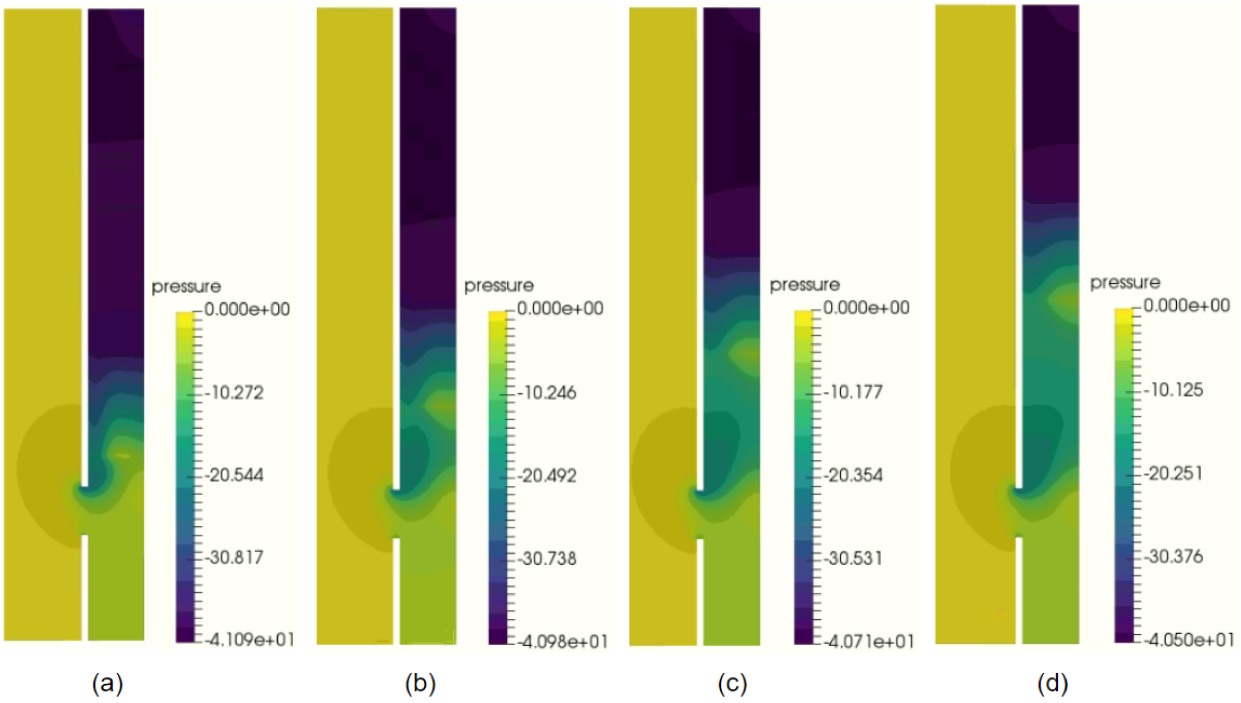

Figure 3.37 – Pressure profiles at $u_{avg} = 2.58$ m/s at different fill locations (a) 0.5 ft, (b) 1.5 ft (c) 2.5 ft (d) 3.5 ft

contribution towards the pressure drop. With the fill raised in the tower, the low-pressure region at the inlet, responsible for the recirculation zone, recovers some pressure, due to which a lower pressure drop is observed when compared to the normal position of the fill. Although the pressure drop is slightly reduced by raising the fill, it still has a sizeable contribution to the tower's overall pressure drop. Closer examination also reveals that when the fill is raised, there is a slight reduction in the pressure drop at the inlet and, on the other hand, the pressure drop across the fill increases. Both of these pressure drop changes tend to counter-balance each other. Therefore, varying the fill location has little impact on the overall pressure drop in the tower.

A default offset of 1/2 feet is present between the fill inlet and the tower inlet. The simulations are now performed by considering a fill of height 2 feet, raised to a new location in the tower with an increment of 1 foot each time at an average velocity of $u_{avg} = 1.20$ m/s. The obtained velocity profiles are shown in Fig. 3.35.

The velocity profile undergoes major changes by changing the fill location in the tower. The air flows under the influence of momentum until it encounters the fill, where it is forced to redistribute. A major portion of the flow is present along the central axis of the tower,

thereby resulting in a recirculation zone extending from the tower inlet until the fill inlet. Therefore, the presence of the recirculation results in a non-uniform distribution of the flow across the tower cross-section. The pressure drop profiles are shown in Fig. 3.36. The overall pressure remained similar for the same velocity as the reduced pressure drop at the inlet is counter-balanced by the increase in pressure drop across the fill. The same effect can be observed at higher velocity as shown in Fig. 3.37 .

3.2.2 Heat and mass transfer

Advection-diffusion equations stated in section 2.3 are used to achieve heat and mass transfer distribution in the tower. Following assumptions were considered in solving for heat and mass distribution:

- The change in fill permeability due to the addition of water is not considered
- The hot water temperature is constant in the fill zone
- The change in air density and velocity due to changes in relative humidity and temperature are not considered

With the introduction of water into the tower, the fill is partly occupied by water as it flows down. Due to this, the effective cross-sectional area available for air is less, and the fill's permeability may decrease. In general, the pressure drop coefficients provided by the manufacturers are related to the air and water flow rate in the tower. In the current study, fill is considered as a porous media, and the permeability value k is calibrated by experimental data, as mentioned in the fluid flow section. Similarly, it has to be calibrated by introducing water in the tower. Due to the lack of experimental data, the change in fill permeability with water introduction is not considered.

The thermal source term is defined as proportional to the temperature difference between the water and air, i.e., $(T_w - T)$, where T_w is the hot water temperature, and T is the air temperature. Water falling through the fill zone loses heat gradually and has a lower temperature at the bottom of the fill than at the top. In the current model, water flow is not solved, and the water temperature variation is unknown. Hence, the water temperature variation is not considered, and the water temperature is assumed constant throughout the fill zone equal to the inlet water temperature.

The fluid flow is obtained with the RANS equations, and the advection-diffusion equations utilize the fluid flow to achieve the heat and mass transfer. The temperature change and mass distribution in the tower should affect the fluid's velocity and density; however, to simplify the calculations, density and velocity are calculated using the inlet air conditions when solving for heat and mass transfer.

Table 3.6 – Boundary conditions for the transport equations

ID	Boundary type	Mass Bound. conditions	Thermal Bound.conditions
1	Inflow - Dirichlet	ω specified (= 0.0033)	T specified (= 298.15 K)
2	Wall - no flux	$\boldsymbol{n} \cdot \boldsymbol{N}_\omega = 0$	$\boldsymbol{n} \cdot \boldsymbol{q}_t = 0$
3	Outflow	$\boldsymbol{n} \cdot \boldsymbol{N}_{\omega d} = \boldsymbol{n} \cdot (-\rho \mathcal{D}_{eff} \nabla \omega_o)$	$\boldsymbol{n} \cdot \boldsymbol{q}_{td} = \boldsymbol{n} \cdot (-\kappa_{eff} \nabla T_o)$
4	Symmetry - no flux	$\boldsymbol{n} \cdot \boldsymbol{N}_\omega = 0$	$\boldsymbol{n} \cdot \boldsymbol{q}_t = 0$
5	Wall - no flux	$\boldsymbol{n} \cdot \boldsymbol{N}_\omega = 0$	$\boldsymbol{n} \cdot \boldsymbol{q}_t = 0$

where $\boldsymbol{N}_\omega = \rho \boldsymbol{v} \omega - \rho \mathcal{D}_{eff} \nabla \omega$, $\boldsymbol{q}_t = \rho c_p \boldsymbol{v} T - \kappa_{eff} \nabla T$, $\boldsymbol{N}_{\omega d} = -\rho \mathcal{D}_{eff} \nabla \omega$, $\boldsymbol{q}_{td} = -\kappa_{eff} \nabla T$, ω_o and T_o are the solutions obtained at the outlet to the previous Newton iteration

To obtain the heat and mass distribution in the tower, the 2D domain is assigned with extra boundary conditions related to the temperature and water mass fraction. The fill zone is considered as the source of both heat, and water vapour with the hot water temperature taken as 323.15 K. The ambient air conditions were considered as 298.15 K with 15% relative humidity for which the water mass fraction results in 0.0033 (water vapour in kg/dry air in kg). Required boundary conditions for the transport equations are reported in Table 3.6.

The value of the mass transfer coefficient is calculated using the empirical Eq. (2.41) and taking liquid flow rate of 2.5 kg/s and air mass flow rate of 1.16 kg/s (liquid to gas flow rate, $L/G = 2.15$), 2 feet fill, and the width of the tower is 0.645 m. The product Ka is 0.005449 g/(cm^3 s). Assuming unity for the Lewis factor, the heat transfer coefficient is 0.005511 W/(cm^3 K).

The obtained temperature and relative humidity is shown in the Fig. 3.38a. The air temperature is equal to the ambient air until it reaches the fill where it encounters the heat source. The air temperature gradually increases as it flows through the fill and reaches an average value of 317 K at the end of the fill. However, it is observed that the maximum temperature of the air reaches almost 323 K at the wall. A similar trend is reported by Williamson et al. [7] where the air temperature is similar in the tower cross-section with a sudden spike at the tower wall. Such a distribution is due to the lower velocity of fluid close to the wall as shown in Fig. 3.39. Since the fluid close to the wall has a lower velocity, it has a longer residence

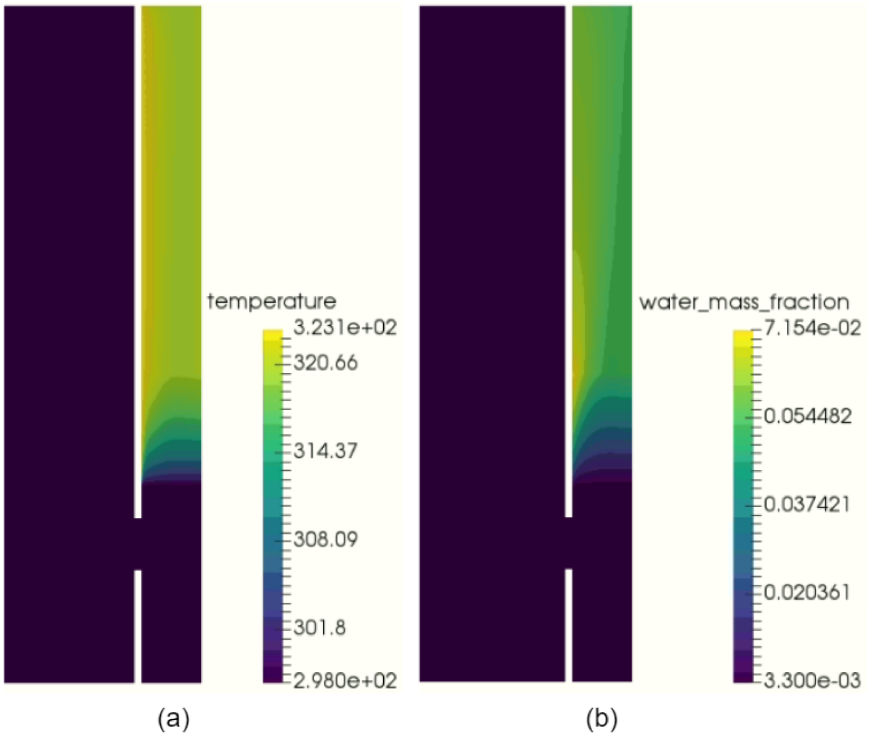

Figure 3.38 – (a) Temperature distribution and (b) water mass fraction distribution for 2 feet fill at $u_{avg} = 1.2$ m/s, $Ka = 0.005449$ g/(cm^3 s) and, $k_T = 0.005511$ W/(cm^3 K)

time in the fill, and, as a result, it can extract more thermal energy, resulting in a higher exit temperature. Mass fraction has a similar distribution as temperature. It remains the same until the fill inlet and then gradually increases as it passes through the fill. A line plot is used at the fill exit with which the average of temperature and mass fraction are calculated.

The average temperature at the fill exit is 321.38 K, an increase of about 23.23 K. Using simple energy conservation between the liquid and the gas phase, the outlet water temperature can be estimated. The conservation equation used is

$$Gc_{pa}(T_a^{out} - T_a^{in}) + m_{eva}H_l \approx Lc_{pw}(T_w^{in} - T_w^{out}) + m_{eva}c_{pw}T_{avg} \tag{3.3}$$

where G is dry airflow rate in kg/s, c_{pa} is specific heat of air equal to 1.00 kJ/(kg K), T_a^{out} is exit air temperature in K, T_a^{in} is inlet air temperature in K, L is the water flow rate in kg/s, c_{pw} is specific heat of water equal to 4.18 kJ/(kg K), T_w^{in} is water inlet temperature in K, T_w^{out} is water outlet temperature in K, m_{eva} is the average water temperature equal to $(\frac{T_w^{in}+T_w^{out}}{2})$, m_{eva} is the rate of water evaporated in kg/s, and H_l is the latent heat of water equal to 2396.4 kJ/(kg K). Initially, the relative humidity is 15 % and the humidity ratio is 0.0033. At the outlet, the average relative humidity is around 78 % and the exit temperature is 321.38 K. For such conditions, the mass fraction is 0.0573 kg/kg resulting in an increase

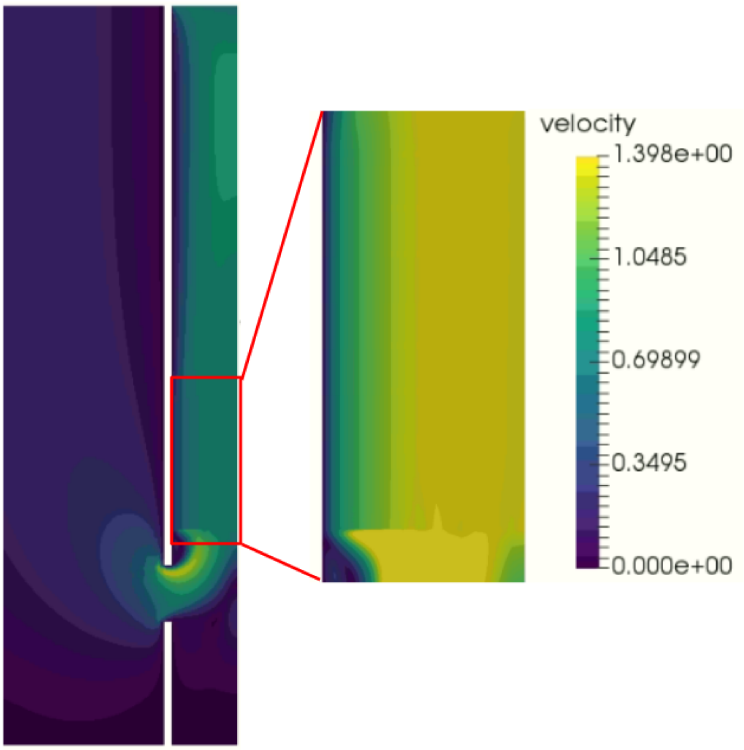

Figure 3.39 – Velocity profile in the fill zone

of 0.054 kg/kg of water vapor in the air. The mass flow rate of evaporated water is equal to the product of 0.054 kg/kg and 0.54 kg/s (u_{avg} = 1.20 m/s) which is 0.029 kg/s. In the current study, the water is not solved for, however, to estimate the water outlet temperature, its flow rate is needed which is obtained by assuming a constant L/G ratio. In calculating the mass transfer coefficients, the L/G ratio is taken as 2.15 therefore the water flow rate is 1.16 kg/s. With these values, the water temperature is reduced by 9.4 K, i.e., the outlet water temperature is $\approx$ 313.75 K.

The ESDLab has also developed CoolIT, an open-source cooling tower simulation analysis software based on the Merkel method. With the same fill parameters, CoolIT resulted in an outlet air temperature of 312.58 K. CoolIT has a lower temperature prediction for air as it is based on the assumption that the air is saturated at the tower's exit with 100% relative humidity. In the current model, the air exit temperature is 321.38 K, higher than the value predicted by CoolIT. The current model tends to overestimate the air temperature because it does not solve for water and, hence, the hot water temperature is kept constant.

The numerical model solves heat and mass flow individually, and the air temperature is not affected by the amount of mass transferred into the air. Due to higher temperature at

Table 3.7 – Numerical simulation vs CoolIT results

S.no	T_{sim}(RH%)	T_{CoolIT}	$T_{sim} - T_{CoolIT}$
1	321.38 (77.89)	312.58	8.8
2	321.87 (81.62)	313.16	8.66
3	322.68 (89.16)	314.98	7.7

the exit, the amount of vapour holding capacity increases; however, the numerical model is not expected to produce 100% saturation at the exit. Hence, it is hypothesized that the numerical model may provide similar results as CoolIT if the numerical model has increased saturation. To check the phenomenon, the fill equation is modified to increase the transfer coefficients in the model such that the mass transfer is increased.

The exponent of $\frac{L}{G}$ ratio in Eq. (2.41) is increased such that the mass transfer coefficient Ka is 0.006269 g/(cm^3 s) and heat transfer coefficient k_T is 0.00634 W/(cm^3 K). By using the increased value of transfer coefficients, both thermal transport and mass transport are increased, for which the simulation results in an exit air temperature of 321.87 K with a relative humidity of 81.62% while CoolIT results in an exit air temperature of 313.16 K. In another simulation, the exponent value is again increased where Ka is 0.00886 g/(cm^3 s), and k_T is 0.00896 W/(cm^3 K). Numerical model results in an exit air temperature of 322.68 K with a relative humidity of 89.16% and CoolIT results in an exit air temperature of 314.98 K.

The exit air temperatures predicted with different exponent values are reported in Table 3.7. With the increasing transfer coefficient, the relative humidity predicted by the numerical model increases. The predicted air exit temperature values between the numerical model and CoolIT are compared. The difference is observed to have almost remained similar with a slight movement of numerical model prediction towards the CoolIT results. This suggests that the results predicted by the numerical model will always have an offset difference due to the overestimation of exit air temperature. The overestimation is due to the higher water temperature value utilized in the source equation (2.43). The constant higher value of hot water temperature results in more heat generation in the system, which is not correct in practical application.

The effect of temperature on the density is neglected in the current model, since the model is developed for mechanically induced draft towers. To evaluate the effect of temperature on density, the dimensionless Richardson number is used from which buoyant velocity due to

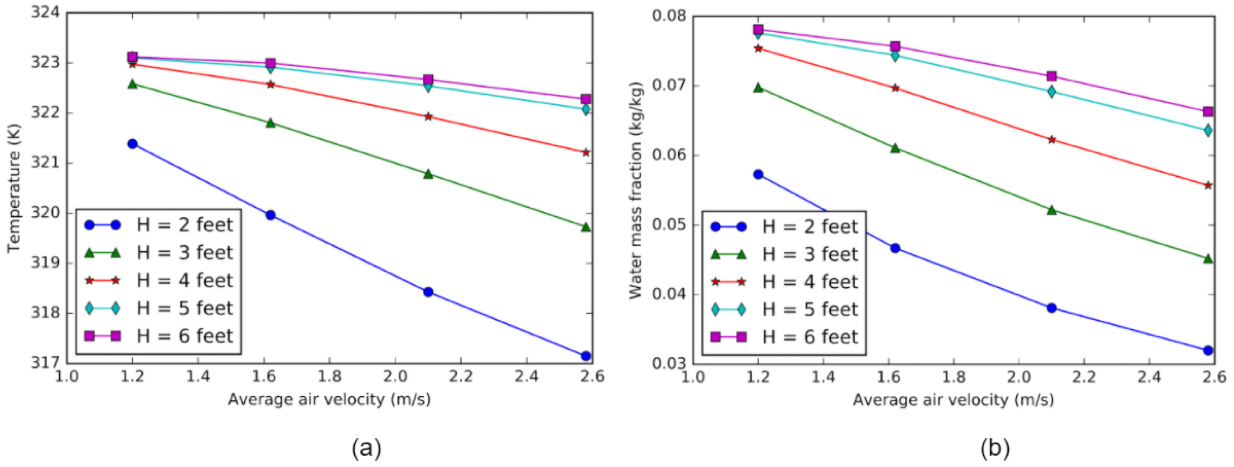

Figure 3.40 – (a) Temperature variation and (b) water mass fraction variation with increasing air flowrate at $Ka = 0.005449$ g/(cm^3 s) and $k_T = 0.005511$ W/(cm^3 K)

density difference can be estimated,

$$u_b = \sqrt{\boldsymbol{g} h \frac{\Delta\rho}{\rho_{amb}}} \tag{3.4}$$

where u_b is the buoyant velocity, $\boldsymbol{g}$ is the acceleration due to gravity, $\Delta\rho$ is the change in density of air, ρ_{amb} is the ambient air density, and h is the vertical height of the tower after the fill.

For an average velocity of 2.58 m/s in the tower, a density difference of 6.3*10^{-2} kg/m^{3}is observed in the tower based on the air temperature at the exit (Eq. (2.44)). The vertical height is 1.38 m, for which the buoyant velocity is evaluated as 0.9 m/s. This value of buoyant velocity is comparable to the average velocity in the tower. A significant buoyant velocity can induce flow into the tower, which is not considered in the current study. As a result, low airflow is available in the tower, resulting in higher air temperature at the exit. In reality, the air is inducted into the tower both due to the fan and as well as due to the density difference. Due to the assumption that the density is not varied with temperature and relative humidity, the current study has a limitation in assessing the total inlet airflow. This in turn affects the prediction of air temperature and humidity ratio at the exit. Hence, the assumption that the density-independent of temperature should be revised in future work even for a case of the mechanically induced draft tower.

Keeping the mass transfer coefficient and heat transfer coefficient constant at 0.005449 g/(cm^3) and 0.00511 W/(cm^3 K) respectively, a parametric study is done for varying air flowrate and fill height. The obtained temperature and water mass fraction are shown in

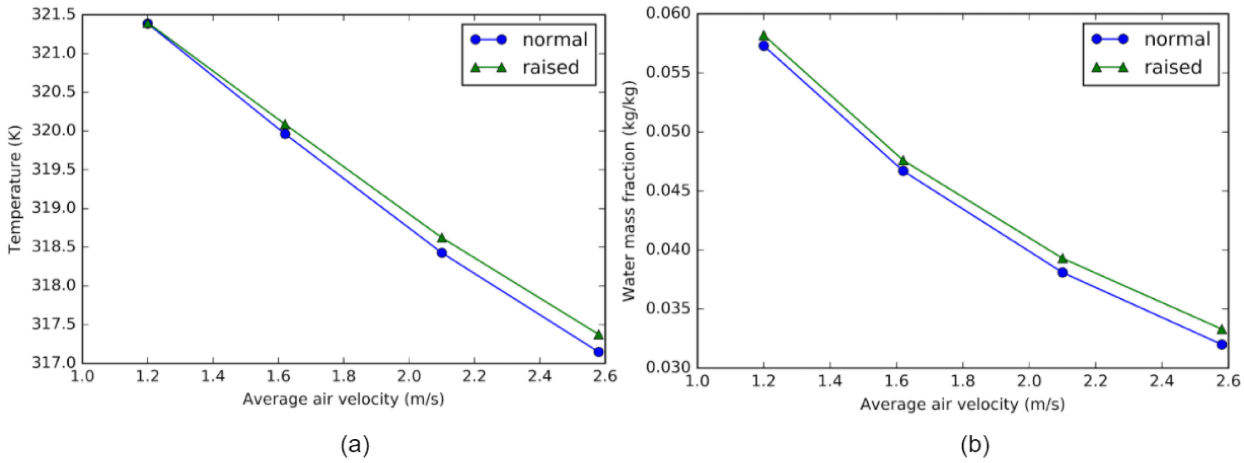

Figure 3.41 – (a) Temperature variation (b) Mass fraction variation. Results obtained with 2 feet fill at k=230 cm^2, Ka = 0.005449 g/(cm^3 s) and k_T = 0.005511 W/(cm^3 K)

Fig. 3.40. For a constant fill height, the temperature decreases with increasing airflow rate. Since the transfer coefficients are constant, the amount of heat transfer remains similar while the airflow rate is higher and, hence, the increase in temperature is lower. Similarly, the amount of mass transfer remains similar, so a decrease in the mass fraction is observed with an increasing flow rate.

For a constant flow rate, the temperature increases with increasing fill height. The air is provided with enough time to get more amount of heat and, hence, more heat transfer takes place which results in higher air temperature at the outlet. With a fill of 6 feet, the air has almost achieved the maximum temperature, i.e., the hot water temperature.

Fig. 3.41 shows the variation of temperature and mass fraction when the fill is raised in the tower. Both are observed to have decreased by raising the fill. When fill is raised in the tower, the maximum velocity value is lower. The velocity distribution is kept constant while solving for heat and mass transfer, due to which convection of heat and mass is reduced and, hence, a lower value of temperature and mass fraction. However, this difference is minimal and does not have a significant effect on thermal performance.

Chapter 4

Industrial cooling tower simulations

From chapter 3, it is established that the current model developed in OpenFCST can provide a fluid flow solution with an algebraic turbulence model. In this chapter, the study is extended to apply the developed model to industrial-scale cooling towers. To show the versatility of the current numerical model, it is first applied to obtain results for an industrial cooling tower and subsequently to a cross-flow tower reported in reference [5].

4.1 Industrial scale cooling tower

The developed model is used to obtain the fluid flow distribution in an industrial-scale cooling tower. Also, the mass and heat transfer equations are solved to predict air temperature and mass fraction. A 2D domain of the cooling tower is shown in Fig. 4.1. The boundary IDs are the same as those mentioned in section 2.4.1 and the same boundary conditions are applied. In this case, the fill is installed at the cooling tower inlet, leaving no offset between the tower inlet and the fill inlet.

The working parameters of the considered cooling tower are not known and hence an approximate air flow rate as in reference [5] is considered such that the Reynolds number in the tower is 784,800. The ambient section of the domain is extended such that it does not affect the inlet conditions. The permeability of the fill is kept the same as obtained from the analysis in chapter 3, i.e, equal to 230 cm^2. The algebraic viscosity is evaluated based on Eq. (2.18) and it is equal to 0.098 Pa.s ($C = 0.06$, $\rho = 1.2$ kg/m^3, $u_{avg} = 1.2$ m/s, $\alpha = 0.125$ and $y_l = 9.13$ m).

A constant velocity value is applied at the tower outlet, and the obtained results are shown in Fig. 4.2. As in the ESDLab tower case, the airflow at the fill inlet is forced to redistribute,

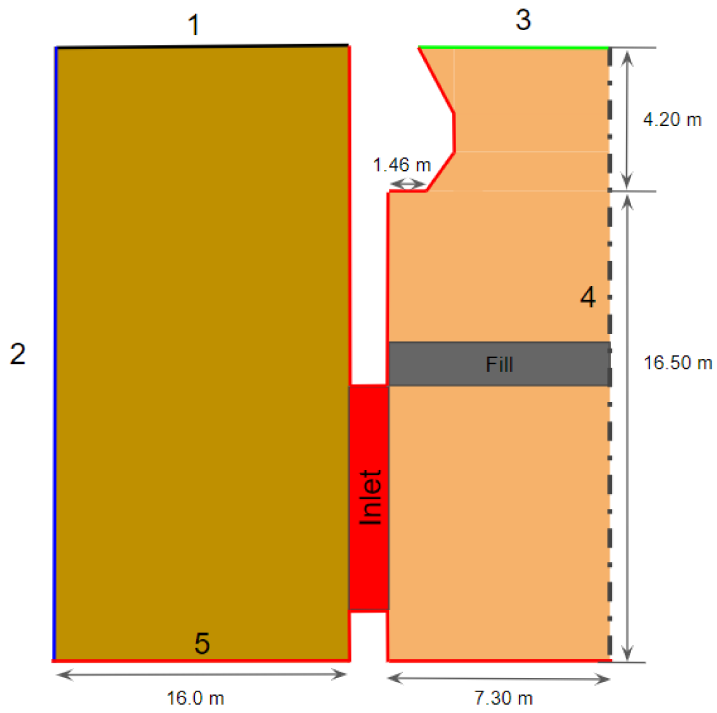

Figure 4.1 – 2D domain of a real cooling tower

resulting in a uniform flow in the tower cross-section. As a result, a maximum flow velocity is observed at the inlet. There is no recirculation zone as no offset is present between the tower inlet and fill inlet. The hyperbolic shape of the stack is approximated with a set of straight lines across which a minor change in the flow profile is observed due to the change in cross-section. However, the flow profile predicted in the stack is not the actual profile as the presence of a fan makes a difference and is the limitation of the current study. The bulk of the pressure drop is in the fill zone, with some pressure drop observed at the fill inlet due to the abrupt change in the flow direction.

The pressure drop follows a similar trend with fill height and flow rate as mentioned in section 3.2.1. By changing the fill location inside the tower, the velocity profile was observed to have a different distribution as shown in Fig. 4.3. In the ESDLab tower, the momentum of the fluid has its effect until the flow reaches the center of the tower. However, in a giant cooling tower like the industrial cooling tower, such a situation is less likely to happen. In such conditions, the recirculation zone is limited to the wall end of the tower and does not have much influence on the flow profile in the rest of the tower cross-section.

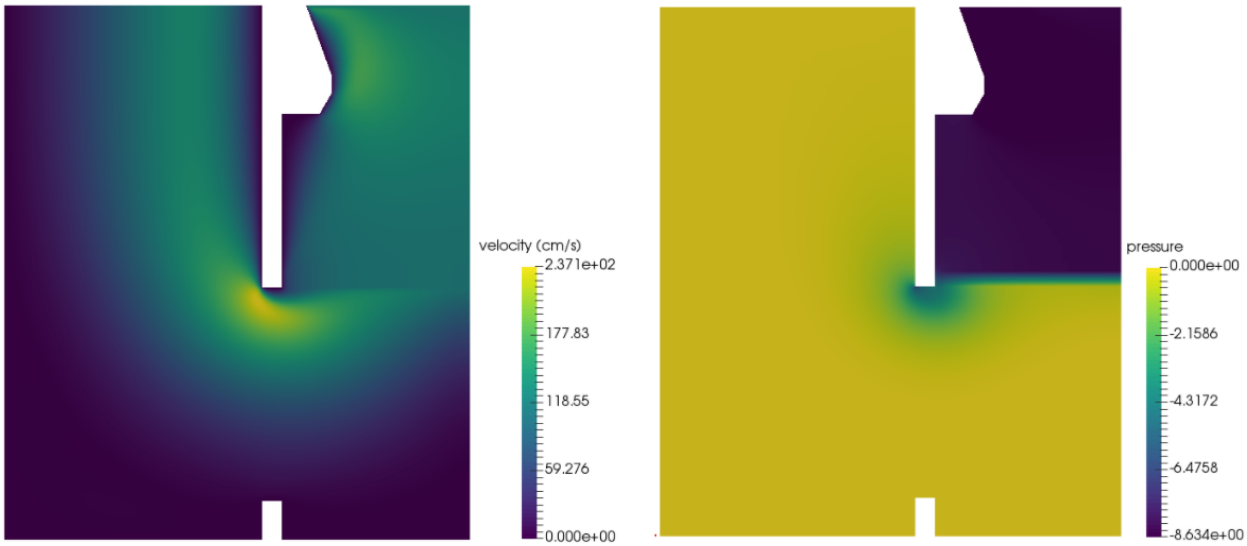

Figure 4.2 – Velocity (left) and pressure (right) distribution in an industrial scale cooling tower at u_{avg}= 1.2 m/s

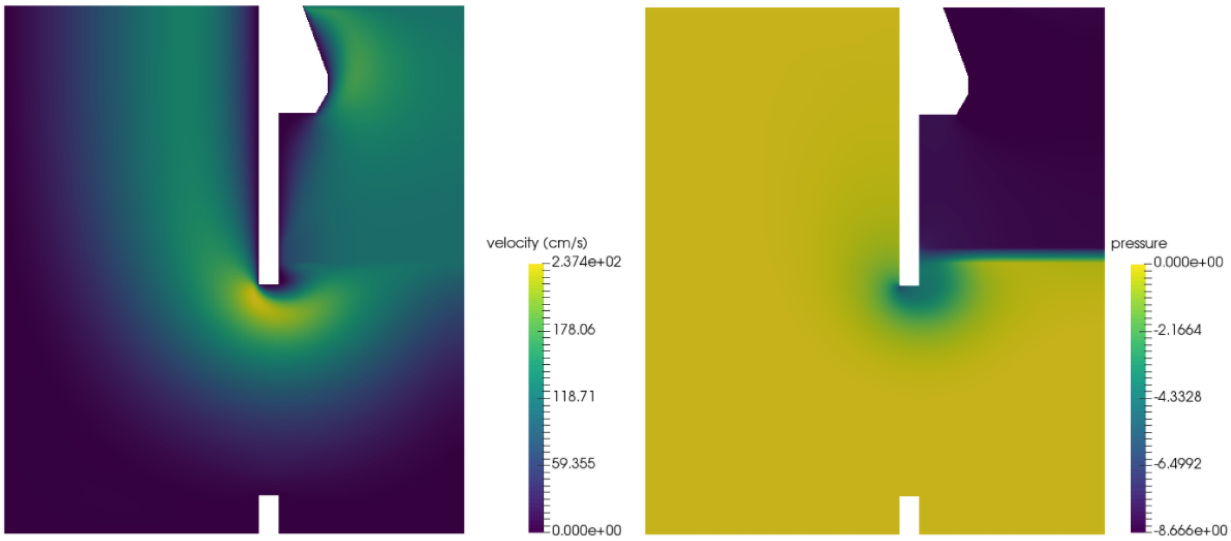

Figure 4.3 – Velocity (left) and pressure (right) distribution in an industrial scale cooling tower at u_{avg}= 1.2 m/s with 2 feet fill raised by 3 feet inside the tower

Parametric studies

The overall pressure drop in the tower increases with fill height as shown in Fig.4.4. The increase in fill height, increases the resistance path for the flow and, hence, a higher overall pressure drop is observed in the tower.

Fig. 4.5a shows the pressure drop variation at the inlet plane and the overall pressure. By default, no offset distance is present between the fill and the inlet of the tower. The fill

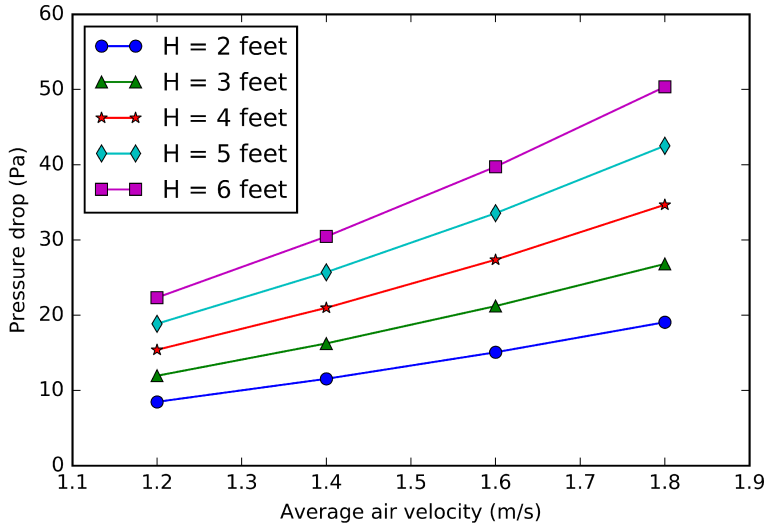

Figure 4.4 – Overall pressure drop variation with velocity at different fill heights

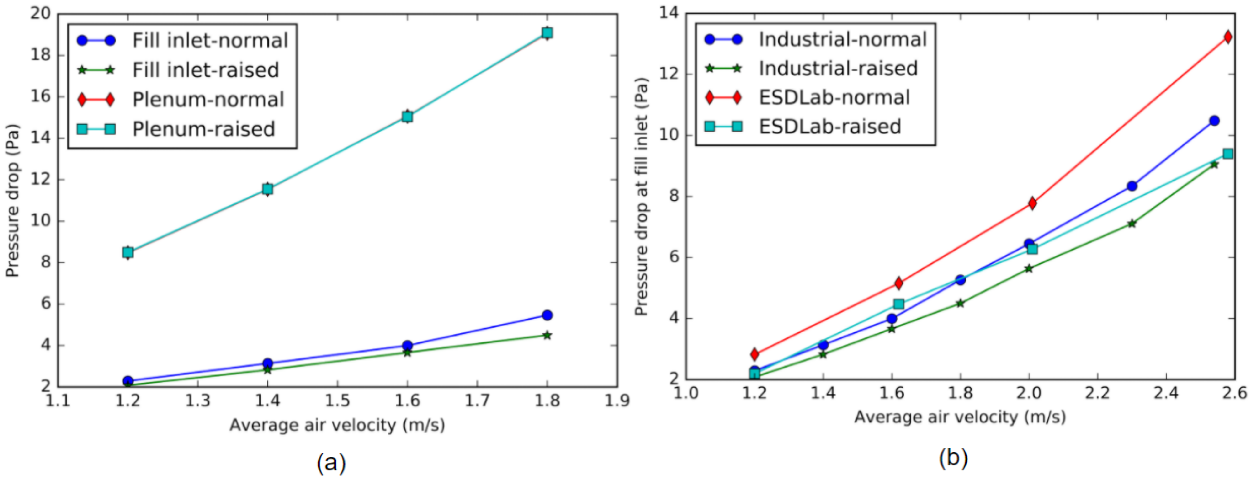

Figure 4.5 – (a) Pressure drop variation at fill inlet plane and plenum plane in the industrial tower (b) Comparison of inlet pressure drop ESDLab tower results for normal and raised fill positions. Results obtained for 2 feet fill and k=230 cm^2

is then raised by 3 feet, and the inlet plane pressure drop and the overall pressure drop are noted. The overall pressure drop is not affected by the fill location in the tower. The inlet pressure drop is reduced by raising the fill in the tower; however, the reduction is very minimal compared to the overall pressure drop in the tower.

Fig. 4.5b shows the inlet pressure drop comparison between the industrial cooling tower and ESDLab cooling tower. ESDLab tower has higher inlet pressure drop values for any fill position, the reason being the tower's geometry. In the case of the ESDLab tower, the

dimensions are smaller such that the air entering from one inlet encounters the air entering at the opposite end of the tower. The flow profile at the inlet is very much influenced by the tower dimensions and can lead to a higher pressure drop at the inlet. In the case of the industrial tower, the recirculation region is very much limited to the inlet tower wall. The dimension of the tower is large enough such that the flow entering has a smooth transition except for a tiny region. For this reason, the inlet effects are higher in the ESDLab tower (test facility with lower dimensions) and lower in the industrial tower. However, the difference in the pressure drop is reduced by raising the fill as the inlet effects in ESDLab are reduced.

4.1.1 Mass and temperature distribution

Similar to the ESDLab tower, the mass transport and thermal transport equations are solved to obtain the mass and temperature distribution in the tower. The ambient air conditions were considered as 298.15 K with 15% relative humidity for which the moisture fraction of water results in 0.0033. The hot water temperature is taken as 323.15 K. Required boundary conditions for the transport equations are reported in Table 4.1

Table 4.1 – Boundary conditions for the transport equations

ID	Boundary type	Mass Bound.conditions	Thermal Bound.conditions
1	Inflow - Dirichlet	ω specified (= 0.0033)	T specified (= 298.15 K)
2	Wall - no flux	$\boldsymbol{n} \cdot \boldsymbol{N}_{\omega} = 0$	$\boldsymbol{n} \cdot \boldsymbol{q}_t = 0$
3	Outflow	$\boldsymbol{n} \cdot \boldsymbol{N}_{\omega d} = \boldsymbol{n} \cdot (-\rho \mathcal{D}_{eff} \nabla \omega_o)$	$\boldsymbol{n} \cdot \boldsymbol{q}_{td} = \boldsymbol{n} \cdot (-\kappa_{eff} \nabla T_o)$
4	Symmetry - no flux	$\boldsymbol{n} \cdot \boldsymbol{N}_{\omega} = 0$	$\boldsymbol{n} \cdot \boldsymbol{q}_t = 0$
5	Wall - no flux	$\boldsymbol{n} \cdot \boldsymbol{N}_{\omega} = 0$	$\boldsymbol{n} \cdot \boldsymbol{q}_t = 0$

where $\boldsymbol{N}_{\omega} = \rho \boldsymbol{v} \omega - \rho \mathcal{D}_{eff} \nabla \omega$, $\boldsymbol{q}_t = \rho c_p \boldsymbol{v} T - \kappa_{eff} \nabla T$, $\boldsymbol{N}_{\omega d} = -\rho \mathcal{D}_{eff} \nabla \omega$, $\boldsymbol{q}_{td} = -\kappa_{eff} \nabla T$, ω_o and T_o are the solutions at the outlet obtained to the previous Netwon iteration.

The transfer coefficients are kept the same as that of the ESDLab tower, meaning the liquid to gas flow rate ratio is kept constant at 2.15. The airflow rate is equal to 182.98 kg/s resulting in a liquid flow rate of 393.40 kg/s.

The obtained temperature and water mass fraction inside the tower is shown in Fig. 4.6. The temperature in the tower is equal to the ambient temperature until it reaches the fill, where it starts to increase owing to the heat source in the fill zone. The temperature of air increases until it passes through the fill. Air exiting the fill acquires a temperature profile that remains uniform for the rest of the tower domain except in the stack. The water mass

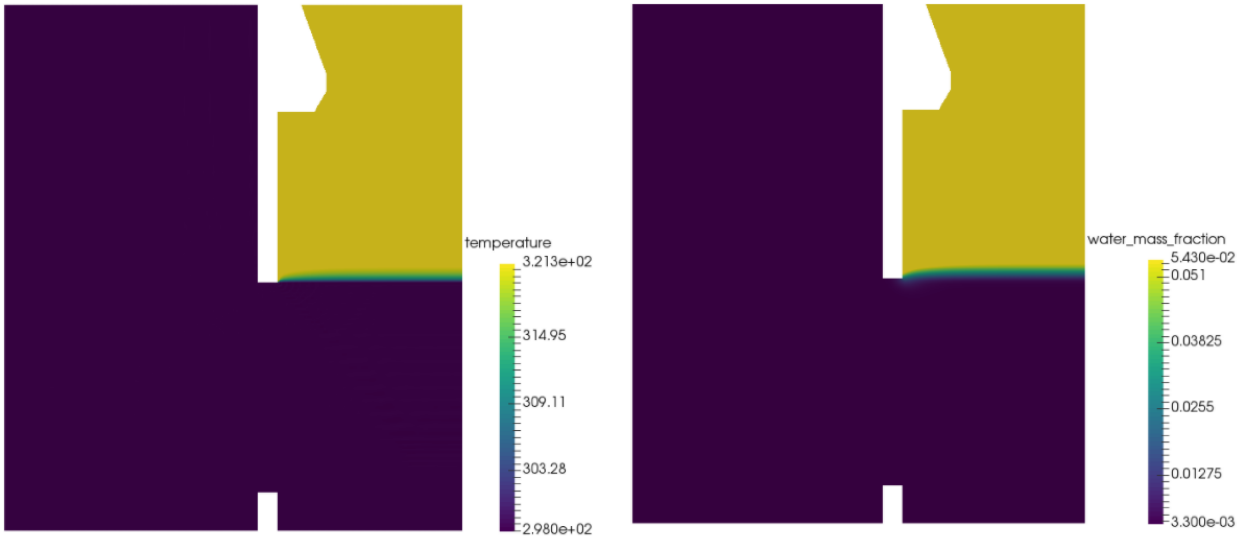

Figure 4.6 – Temperature (left) and water mass fraction (right) distribution in an industrial scale cooling tower. 2 feet fill with u_{avg} =1.20 m/s, Ka = 0.005449 g/(cm^3 s) and k_T = 0.005511 W/(cm^3 K)

fraction inside the tower follows a similar trend as of temperature. It remains 0.0033 (water vapour in kg/dry air in kg) until the air reaches the fill and starts to increase as it encounters the mass source in the fill zone. It increases until it reaches the end of the fill zone and remains uniform for the rest of the domain.

Both temperature and water mass fraction have similar distribution profiles at the fill exit. 2 feet fill with L/G ratio equal to 2.15 can result in an average temperature of 322 K at the tower exit. The average mass fraction of water at the tower's exit is 0.0606 resulting in a relative humidity of 78.52%. Using the energy balance in Eq. (3.3), the outlet water temperature is calculated as 313.5 K, a reduction of about 10 K in the temperature of the water.

Parametric studies

Parametric study is conducted on the industrial cooling tower, for varying flow rate, fill height and constant transfer coefficients where Ka is 0.005449 g/(cm^3 s), and k_T is 0.005511 W/(cm^3 K). For a constant fill height, the temperature of the air decreases with increasing airflow rate, as shown in Fig. 4.7a. Since the transfer coefficients are kept constant, the same amount of heat and mass transport occurs; however, more air is available, due to which air temperature decreases with increasing flow rate.

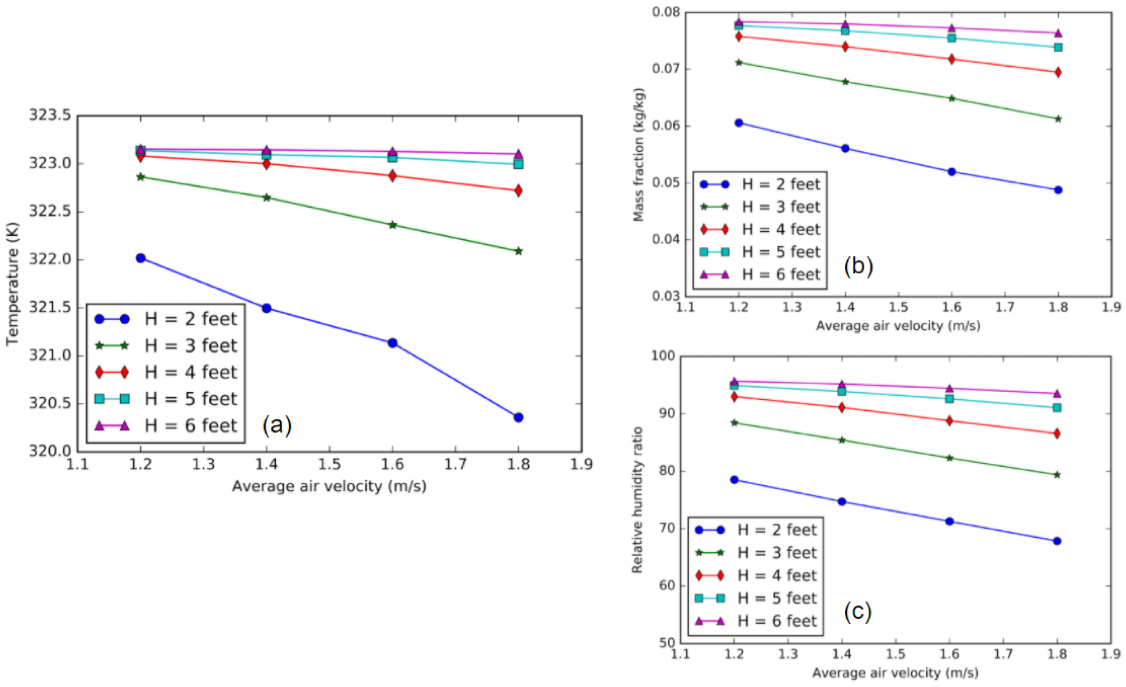

Figure 4.7 – (a) Air temperature variation (b) Mass fraction variation (c) Relative humidity variation with average air velocity at L/G =2.15, Ka = 0.005449 g/(cm^3 s) and k_T = 0.005511 W/(cm^3 K)

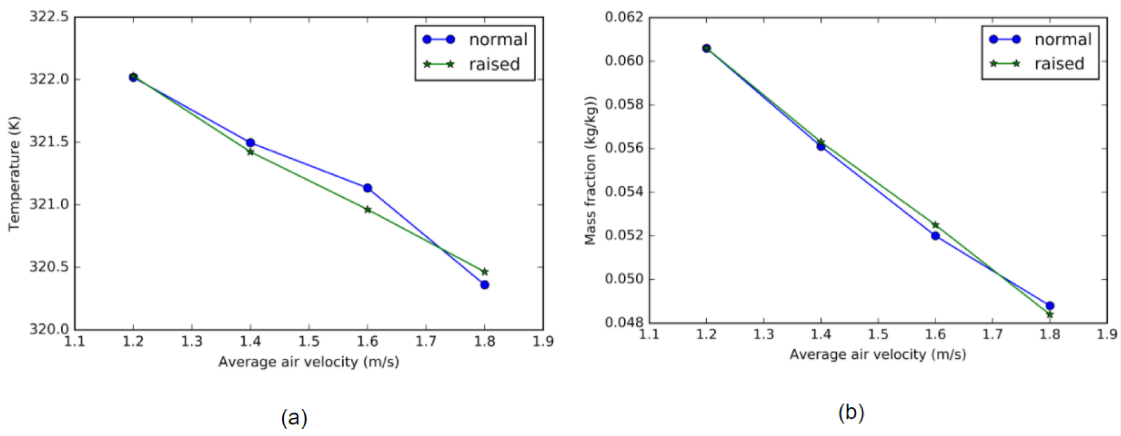

Figure 4.8 – (a) Temperature variation (b) Mass fraction variation with air velocity at Ka = 0.005449 g/(cm^3 s) and, k_T = 0.005511 W/(cm^3 K)

For a constant airflow rate, the air temperature increases with increasing fill height. Higher fill height results in more heat and mass transfer between air and water and higher exit air temperature. The air temperature is observed to have reached the maximum temperature available, i.e., hot water temperature signifying that the tower is very effective and result in good thermal performance. The mass fraction and relative humidity also has a similar variation as of temperature with flow rate and fill height as shown in Fig. 4.7b and 4.7c

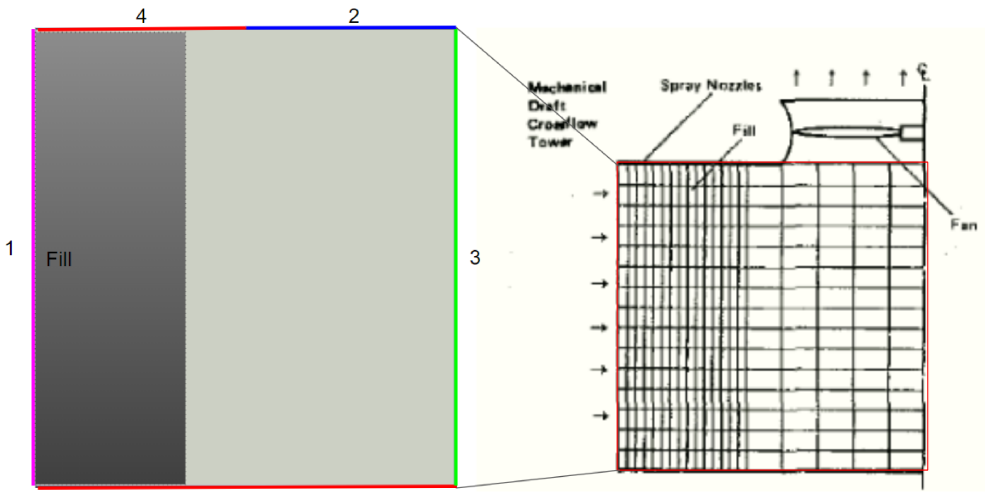

Figure 4.9 – Computational domain in accordance with the domain in reference [5]. Reproduced with permission (permission pending)

respectively.

Fig. 4.8 shows the temperature and mass fraction variation with velocity for fill in normal and raised position. The effect of fill position on the temperature and mass fraction is negligible as it does not affect the flow distribution in the tower.

4.2 Cross-flow tower

The industrial cross-flow tower studied in reference [5] is analyzed as an example of a cross-flow cooling tower. The geometry and dimensions of the tower are given in Fig. 4.9 and Table 4.2 respectively. The fan stack section is not modelled; instead, the outlet pressure is taken to be -152 Pa. Based on the pressure at the outlet, the density is evaluated and is applied as a boundary condition at the outlet (boundary ID 2). An ambient density value is applied at the inlet (boundary ID 1) while boundary ID 3 is applied with symmetry condition, and boundary ID 4 is applied with no-slip boundary condition.

Table 4.2 – Cross flow tower dimensions

Mean-half width of the tower	9.70 m
Cell width	11.98 m
Air travel with of the fill	5.15 m
Fan diameter	8.53 m
Type of fill	Splash bar

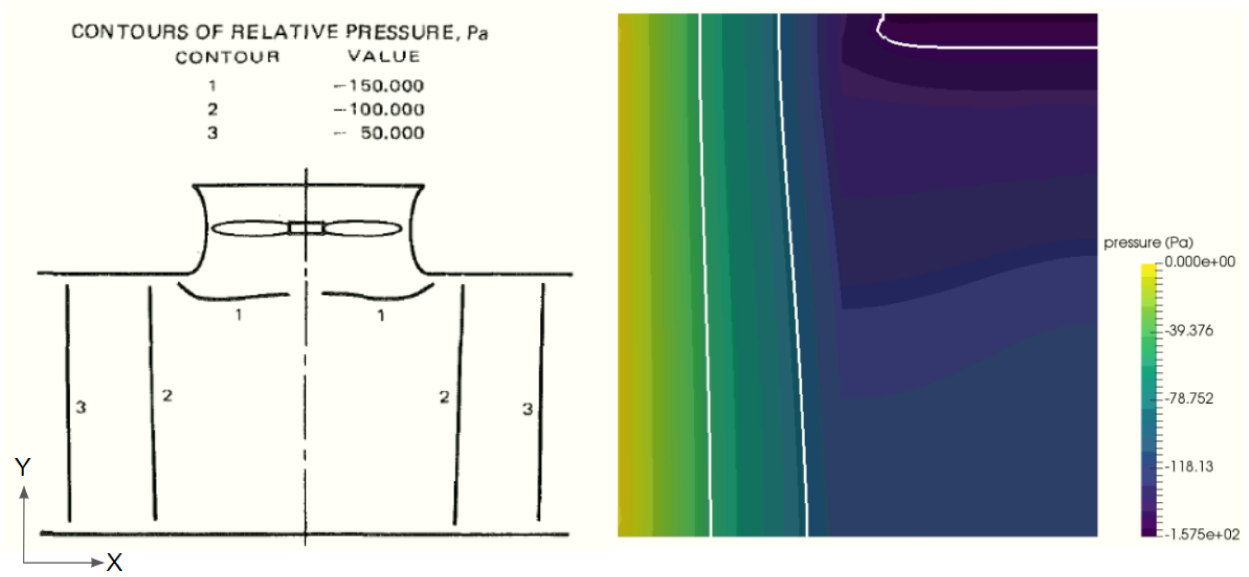

Figure 4.10 – Comparison of pressure profiles from reference [5] (left) and from our model (right) for permeability value of 2400 cm^2 in X and Y directions. Reproduced with permission. (permission pending)

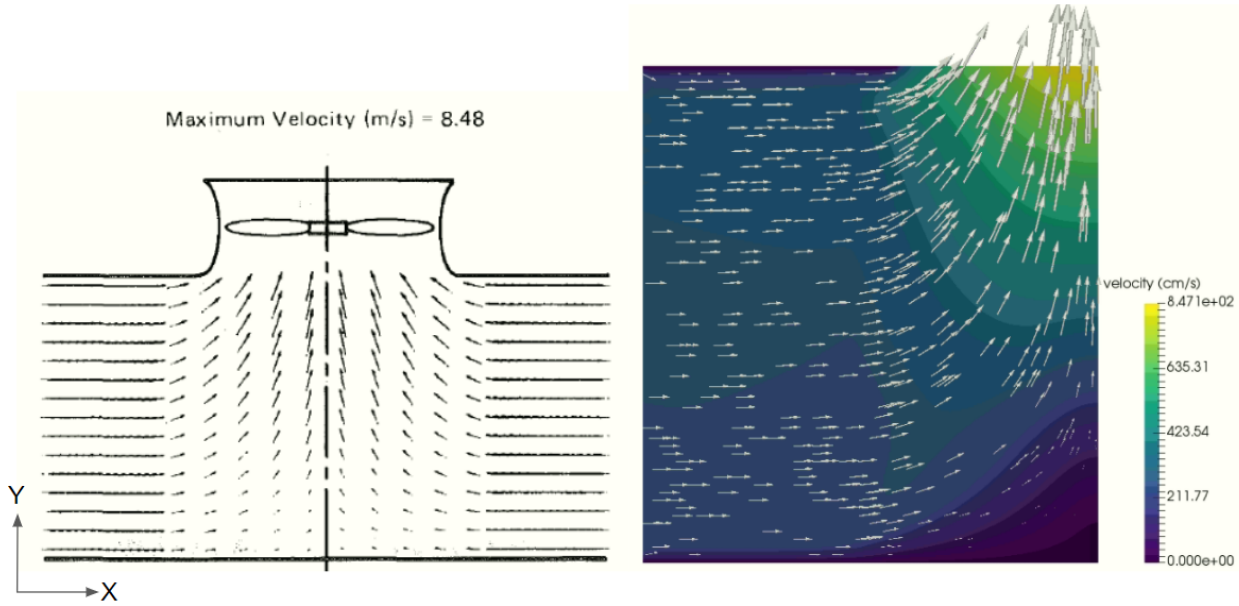

Figure 4.11 – Comparison of velocity profiles from reference [5] (left) and from our model (right) for permeability value of 2400 cm^2 in X and Y directions. Reproduced with permission (permission pending)

To estimate the turbulence viscosity, the fill pitch is taken to be 20.32 cm based on reference [5], and the average velocity of 4.24 m/s is used. The final turbulent viscosity then is 0.554 Pa.s. Fill type is mentioned as a splash fill and, hence, the permeability values are provided

in X and Y directions. Similar to the parametric study in section 3.2, the permeability is varied in either direction to arrive at a specific value such that the provided velocity values are matched with the simulation values. The final value of permeability is 1600 cm^2 in either direction.

The obtained flow profiles are compared to those reported by Majumdar et al. [5]. Fig. 4.10 shows the pressure profiles from reference [5] (left) and from present model (right). In the present model results, isobaric contour lines are provided for the same values as reported in Majumdar et al. [5]. The pressure has a gradual variation in the horizontal direction and an insignificant variation in the vertical direction in both models. The bulk of the pressure drop occurs in the fill zone.

Fig. 4.11 shows the comparison between velocity profiles. Velocity in the fill zone is horizontal as shown in reference [5] (left) and mostly uniform throughout the zone. As soon as the air exits the fill, it is smoothly accelerated towards the tower's center as it exits the tower. Both the profiles have a similar trend at the tower exit and at the bottom of the tower, where the air velocity is low. The air velocity increases gradually, moving from the bottom of the tower towards the top and has the maximum velocity at the center of the tower outlet.

4.2.1 Mass and temperature distribution

The ambient air temperature is taken as 306 K with a relative humidity of 58% such that the mass fraction is equal to 0.018 kg/kg. The hot water temperature is given as 313.15 K. The boundary conditions applied are shown in Table 4.3

Table 4.3 – Boundary conditions for the transport equations

ID	Boundary type	Mass Bound.condition	Thermal Bound.condition
1	Inflow - Dirichlet	ω specified (= 0.018)	T specified (= 306.15 K)
2	Outflow	$\boldsymbol{n} \cdot \boldsymbol{N}_{\omega d} = \boldsymbol{n} \cdot (-\rho \mathcal{D}_{eff} \nabla \omega_o)$	$\boldsymbol{n} \cdot \boldsymbol{q}_{td} = \boldsymbol{n} \cdot (-\kappa_{eff} \nabla T_o)$
3	Symmetry - no flux	$\boldsymbol{n} \cdot \boldsymbol{N}_{\omega} = 0$	$\boldsymbol{n} \cdot \boldsymbol{q}_{t} = 0$
4	Wall - no flux	$\boldsymbol{n} \cdot \boldsymbol{N}_{\omega} = 0$	$\boldsymbol{n} \cdot \boldsymbol{q}_{t} = 0$

where $\boldsymbol{N}_{\omega} = \rho \boldsymbol{v} \omega - \rho \mathcal{D}_{eff} \nabla \omega$ and $\boldsymbol{q}_t = \rho c_p \boldsymbol{v} T - \kappa_{eff} \nabla T$, $\boldsymbol{N}_{\omega d} = -\rho \mathcal{D}_{eff} \nabla \omega$, $\boldsymbol{q}_{td} = -\kappa_{eff} \nabla T$, ω_o and T_o are the solutions at the outlet obtained to the previous Newton iteration.

The temperature and mass fraction distribution in the tower are obtained by taking mass transfer coefficient as 0.0013 g/(cm^3 s) and heat transfer coefficient as 0.005511 W/(cm^3 K). The temperature profiles are shown in Fig. 4.12 where the profile from reference [5] (left)

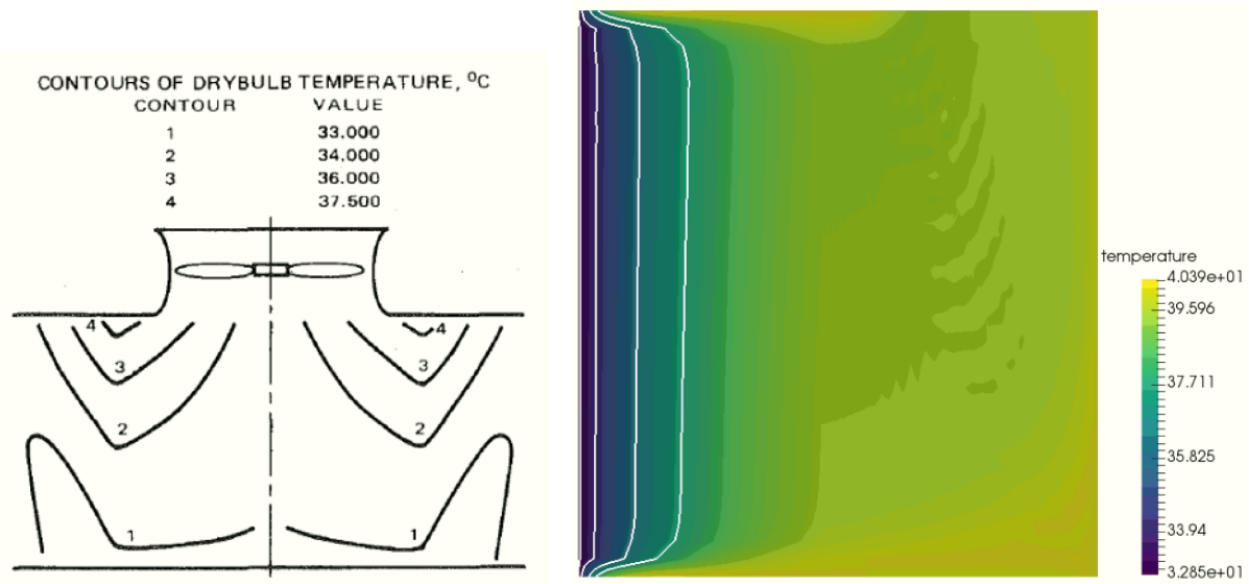

Figure 4.12 – Comparison of temperature profiles from reference [5] (left) and from our model (right) $Ka = 0.0013$ g/(cm^3 s)

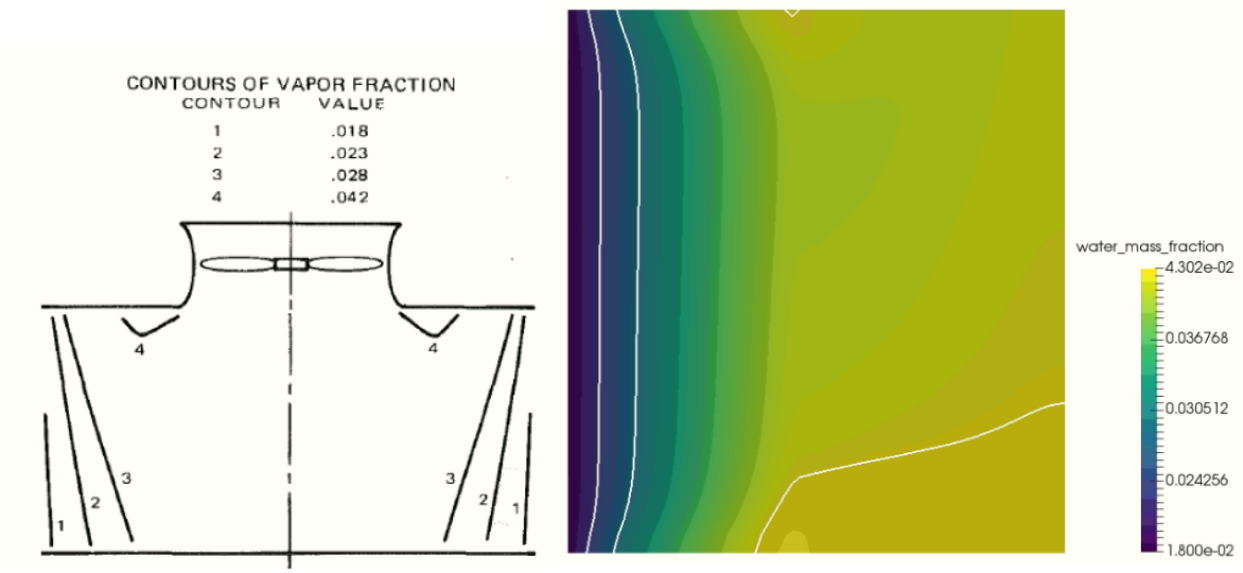

Figure 4.13 – Comparison of water mass fraction profiles from reference [5] (left) and from our model (right). $Ka = 0.0013$ g/(cm^3 s)

is compared with the temperature profile from the current model (right). The temperature gradually increases as it passes through the fill. The temperature profiles for the given temperatures have significant variations due to the constant hot water assumption considered in the study. The hot water drops from the top of the fill and cools down, achieving the lowest temperature at the bottom of the tower. The air entering the fill horizontally encounters

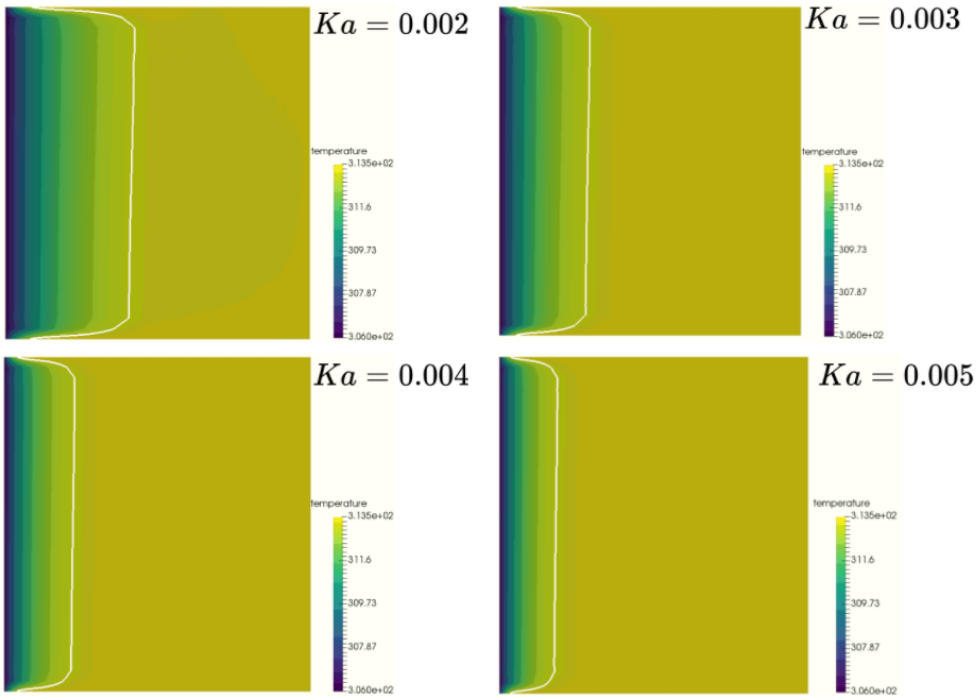

Figure 4.14 – Temperature distribution in cross flow tower with varying mass transfer coefficient. Contour line for $T = 323$ K

hot water at the top and relatively cold water at the bottom. Such a differential water temperature will result in a differential heat and mass flow along the vertical dimension, thus resulting in a higher air temperature at the top and relatively cold air at the bottom. In the current study, the variation of water temperature is not considered, and, hence, the air does not experience changes in the vertical direction.

The water mass fraction profiles are shown in Fig. 4.13 where the profile from reference [5] (left) is compared with the mass fraction profile from the current model. The mass fraction increases as the air pass through the fill due to the same reason noted for the temperature.

Both temperature and mass fraction in the tower is affected by the source terms used in the equations. Having a constant source term across the fill resulted in uniform profiles for both temperature and mass fraction, which otherwise would have resulted in a non-uniform profile across the fill cross-section. The transfer coefficients also play an important role in deciding the extent of heat and mass transfer occurring in the tower, and hence they need to be calibrated for better approximation. A parametric study on the mass transfer coefficient is shown in Fig. 4.14 and in Fig. 4.15. Upon increasing the mass transfer coefficient (heat transfer coefficient is also increased as it is connected to mass transfer coefficient

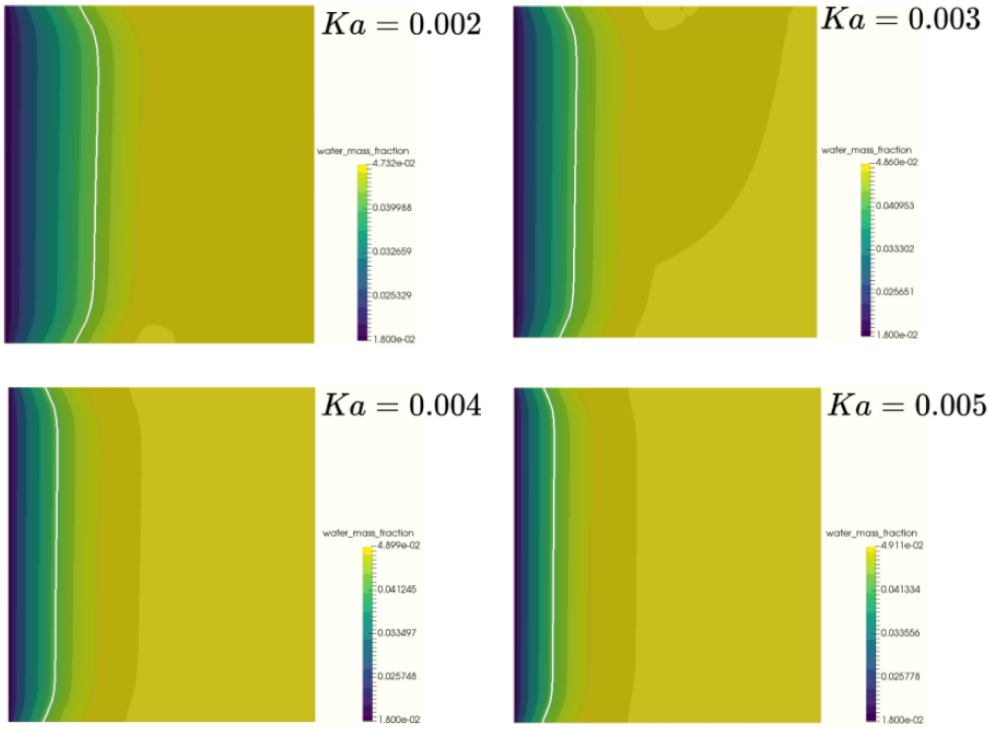

Figure 4.15 – Water mass fraction distribution in cross flow tower with varying mass transfer coefficient. Contour line $\omega = 0.042$

by Lewis factor), the maximum value of temperature and the mass fraction is attained faster.

Chapter 5

Conclusion and future work

The flow behaviour inside an empty cooling tower is studied in this thesis using an incompressible RANS fluid flow solver. Two and three-dimensional flow simulations are performed and validated against experimental data. The two-dimensional approach provides us with a reasonable estimation of pressure drop in the tower; however, it is not sufficient to understand the tower in totality due to the presence of three-dimensional effects like varying velocity profile at the inlet and wall effects in the tower.

To better estimate the flow profiles in the tower, three-dimensional simulations are performed. The fluid flow solver implemented in the in-house Open-source Fuel Cell Simulation Toolbox (OpenFCST) is utilized to perform these simulations. Ansys was also utilized to assess the validity of the obtained solutions and assess the algebraic model's accuracy. The simulation results obtained from different solvers are then compared with the experimental data.

Ansys simulations with a $k - \epsilon$ turbulence model were able to capture the critical features in the tower; however, they deviated from the experimental data compared to OpenFCST and Ansys with algebraic turbulence model. OpenFCST had a good agreement and matched with the Ansys results suggesting that the simulation with OpenFCST is appropriate.

To simulate the fluid flow of a cooling tower with a fill, the compressible RANS equations were solved with the algebraic turbulence model in a two-dimensional domain. The fill is treated as a porous media. The fill permeability value is calibrated using a parametric study, first using Darcy's approximation and then Forchheimer's approximation. Results showed that the calibrated fill permeability value with Darcy's approximation is not valid for the cooling tower as the flow is in a turbulent regime. Forchherimer's estimation for the resistance gave good predictions of pressure drop at measured experimental values. Therefore,

it is recommended that for a fill, when considered as a porous media, the Forchhermier estimation is used for better prediction of pressure drop.

The fluid flow in a mechanical tower is non-uniform at the tower inlet due to the abrupt change in the flow direction. Once inside the tower, the flow behaviour is majorly decided by the fill parameters like fill height, fill location in the tower, and overall flow rate. A parametric study of fill height and flow rate showed that the pressure drop in the tower increases with fill height and flow rate in the tower.

According to the experimental data, inlet effects can contribute to the overall pressure drop. To study this, the fill is raised in the tower, and the achieved pressure drop is compared with the normal case. The inlet effects result in a different pressure drop, especially at higher air velocities in the tower. However, the difference is still less compared to the overall pressure drop and needs further research into the inlet geometry to understand the extent of its significance. The velocity profile does not have much variation with fill height and flow rate. It, however, changes with fill location in the tower.

Advection-diffusion equations are also solved to achieve heat and mass transfer in the tower. The temperature gradually increases across the fill zone resulting in a uniform temperature across the cross-section with a higher temperature value near the wall region. However, the overall temperature value is higher at the fill exit due to the constant hot water temperature value considered in the heat source term. A similar analogy can be made to explain mass fraction distribution in the tower.

Two types of industrial towers, a counter-flow and a cross-flow tower, are studied to understand the application of the current model to different towers. A counter-flow tower with no fill offset at the inlet has no recirculation zone observed in the rain zone. If the fill is raised in the tower, the recirculation zone is observed; however, its reach is less than the ESDLab tower due to the large overall width of the industrial tower. Pressure drop increases with fill height and airflow rate. Raising fill in the tower has very little change in the pressure drop and can be attributed to the lower inlet effects for the given inlet geometry. Outlet air temperature and mass fraction reduce with increasing air velocity.

A cross-flow tower analyzed in the literature is simulated, and the obtained flow profiles are observed to be in good agreement with the profiles reported. The pressure drop is achieved across the fill with no recirculation zone due to the way the geometry is defined. The velocity is uniform in the fill zone with a smooth accelerating flow at the exit. The temperature and

mass fraction are also plotted, which are compared with profiles reported in the literature. They both show significant deviation from the literature owing to the assumption of constant hot water temperature considered in the current study.

The current study is focused on analyzing fluid flow behaviour in a cooling tower with the help of compressible RANS equations along with the advection-diffusion equations. The study of the cooling towers can be enhanced by :

- Solve for water in the domain and associated local heat and mass transfer coefficients
- Consider the effect of temperature and mass fraction on the density to incorporate the buoyancy effects
- Include fan model such that the flow behaviour at the tower exit imitates the flow arisen due to fan rotation
- More research on the influence of inlet effects on the pressure drop in the tower

References

[1] Johannes Christiaan Kloppers. *A critical evaluation and refinement of the performance prediction of wet-cooling towers*. PhD thesis, Stellenbosch: University of Stellenbosch, 2003.

[2] John C Hensley. *Cooling tower fundamentals*. Marley Cooling Tower Company, 1985.

[3] Elizabeth Clare. *The Design of an Experimental Model for the 3D Characterization of Airflow in Counterflow Cooling Towers*. Master's thesis, University of Alberta, 2020.

[4] Chad A Balen. A multi-component mass transport model for polymer electrolyte fuel cells. 2016.

[5] AK Majumdar, AK Singhal, HE Reilly, and JA Bartz. Numerical modeling of wet cooling towers—part 2: Application to natural and mechanical draft towers. *Journal of heat transfer*, 105(4):736–743, 1983.

[6] J Van der Merwe and C.G du Toit. Numerical simulation of a wet cooling tower. *R and D*, 18(2):23–30, 2002.

[7] N Williamson, M Behnia, and S Armfield. Numerical simulation of heat and mass transfer in a natural draft wet cooling tower. In *Proceedings of the 15 th Australasian Fluid Mechanics Conference*, pages 13–17, 2004.

[8] JE Terblanche and DG Kröger. Experimental evaluation of the aerodynamic inlet losses in cooling towers. *South African Institute of Mechanical Engineers R&D Journal*, 10 (2):41–44, 1994.

[9] AF Du Preez and DG Kröger. Experimental evaluation of aerodynamic inlet losses in natural draft dry cooling towers. Technical report, 1989.

[10] D.G. Kröger. *Air-Cooled Heat Exchangers and Cooling Towers: Thermal-Flow Performance Evaluation and Design*. Begell House, 1999. ISBN 9781567001402. URL `https://books.google.ca/books?id=OISIOwAACAAJ`.

[11] HCR Reuter and DG Kröger. Computational fluid dynamics analysis of cooling tower inlets. *Journal of Fluids Engineering*, 133(8):081104, 2011.

[12] D. G. Buys, J. D. Kröger. Cost-optimal design of dry cooling towers through mathematical programming techniques. *Journal of Heat Transfer*, 111(2):322–327, 1989. doi: 10.1115/1.3250680[doi].

[13] A. Klimanek and R.A. Białecki. Solution of heat and mass transfer in counterflow wet-cooling tower fills. *International Communications in Heat and Mass Transfer*, 36(6):547 – 553, 2009. ISSN 0735-1933. doi: https://doi.org/10.1016/j.icheatmasstransfer.2009.03.007. URL `http://www.sciencedirect.com/science/article/pii/S0735193309000712`.

[14] AK Majumdar, AK Singhal, and DB Spalding. Numerical modeling of wet cooling towers—part 1: mathematical and physical models. *Journal of heat transfer*, 105(4): 728–735, 1983.

[15] MNA Hawlader and BM Liu. Numerical study of the thermal–hydraulic performance of evaporative natural draft cooling towers. *Applied Thermal Engineering*, 22(1):41–59, 2002.

[16] Nenad Milosavljevic and Pertti Heikkilä. A comprehensive approach to cooling tower design. *Applied thermal engineering*, 21(9):899–915, 2001.

[17] E. Razafindrakoto, J. L. Grange, L. Fabre, H. Delabrière, and S. Delaroff. *3D Numerical Simulation of a Natural Draught Cooling Tower Flow*, pages 248–255. Vieweg+Teubner Verlag, Wiesbaden, 1996. ISBN 978-3-322-89838-8. doi: 10.1007/978-3-322-89838-8_33. URL `https://doi.org/10.1007/978-3-322-89838-8_33`.

[18] Rafat Al-Waked and Masud Behnia. Enhancing performance of wet cooling towers. *Energy Conversion and Management*, 48(10):2638–2648, 2007.

[19] Friedrich Merkel. *Verdunstungskühlung*. VDI-Verlag, 1925.

[20] M Poppe and H Rögener. Berechnung von rückkühlwerken. *VDI Wärmeatlas, pp. Mi*, 1991.

[21] H Jaber and RL Webb. Design of cooling towers by the effectiveness-ntu method. *Journal of Heat Transfer*, 111(4):837–843, 1989.

[22] E De Villiers and DG Kröger. Inlet losses in counterflow wet-cooling towers. *J. Eng. Gas Turbines Power*, 123(2):460–464, 2001.

[23] H Lowe and D Christie. Heat transfer and pressure drop data on cooling tower packings, and model studies of the resistance of natural draught towers to airflow, part v. international development in heat transfer. *American Society of Mechanical Engineers, New York*, 1961.

[24] Rafat Al-Waked and Masud Behnia. Cfd simulation of wet cooling towers. *Applied thermal engineering*, 26(4):382–395, 2006.

[25] N Williamson, S Armfield, and M Behnia. Numerical simulation of flow in a natural draft wet cooling tower–the effect of radial thermofluid fields. *Applied Thermal Engineering*, 28(2-3):178–189, 2008.

[26] G Gan and SB Riffat. Numerical simulation of closed wet cooling towers for chilled ceiling systems. *Applied Thermal Engineering*, 19(12):1279–1296, 1999.

[27] David C Wilcox et al. *Turbulence modeling for CFD*, volume 2. DCW industries La Canada, CA, 1998.

[28] Joel H Ferziger, Milovan Perić, and Robert L Street. *Computational methods for fluid dynamics*, volume 3. Springer, 2002.

[29] Jean-Luc Guermond, Richard Pasquetti, and Bojan Popov. From suitable weak solutions to entropy viscosity. In *Quality and Reliability of Large-Eddy Simulations II*, pages 373–390. Springer, 2011.

[30] Adam Klimanek, Michał Cedzich, and Ryszard Białecki. 3d cfd modeling of natural draft wet-cooling tower with flue gas injection. *Applied Thermal Engineering*, 91:824–833, 2015.

[31] B.R. Becker, W.E. Stewart, T.M. Walter, and C.S. Becker. A numerical model of cooling tower plume recirculation. *Mathematical and Computer Modelling*, 12(7):799 – 819, 1989. ISSN 0895-7177. doi: https://doi.org/10.1016/0895-7177(89)90135-0. URL `http://www.sciencedirect.com/science/article/pii/0895717789901350`.

[32] HF Burcharth and OK Andersen. On the one-dimensional steady and unsteady porous flow equations. *Coastal engineering*, 24(3-4):233–257, 1995.

[33] Rafat Al-Waked and Masud Behnia. The performance of natural draft dry cooling towers under crosswind: Cfd study. *International journal of energy and research*, 28: 147–162, 2004.

[34] F Bosnjakovic. Technical thermodynamics, holt, rinehart and winston. *Inc. Edition*, 1965.

[35] WE Ranz, W R_ Marshall, et al. Evaporation from drops. *Chem. eng. prog*, 48(3): 141–146, 1952.

[36] Wolfgang Rodi. *Turbulence models and their application in hydraulics*. Routledge, 2017.

[37] Stephen Whitaker. *The method of volume averaging*, volume 13. Springer Science & Business Media, 2013.

[38] Alex Jarauta, Valentin Zingan, Peter Minev, and Marc Secanell. A compressible fluid flow model coupling channel and porous media flows and its application to fuel cell materials. *Transport in Porous Media*, 134(2):351–386, 2020.

[39] Johannes C Kloppers and Detlev G Kröger. The lewis factor and its influence on the performance prediction of wet-cooling towers. *International journal of thermal sciences*, 44(9):879–884, 2005.

[40] Konrad Koeltzsch. The height dependence of the turbulent schmidt number within the boundary layer. *Atmospheric Environment*, 34(7):1147–1151, 2000.

[41] Thomas K Flesch, John H Prueger, and Jerry L Hatfield. Turbulent schmidt number from a tracer experiment. *Agricultural and Forest Meteorology*, 111(4):299–307, 2002.

[42] DB Spalding. Concentration fluctuations in a round turbulent free jet. In *Numerical Prediction of Flow, Heat Transfer, Turbulence and Combustion*, pages 41–53. Elsevier, 1983.

[43] BE Launder. Heat and mass transport. In *Turbulence*, pages 231–287. Springer, 1975.

[44] Yoshihide Tominaga and Ted Stathopoulos. Turbulent schmidt numbers for cfd analysis with various types of flowfield. *Atmospheric Environment*, 41(37):8091 – 8099, 2007. ISSN 1352-2310. doi: https://doi.org/10.1016/j.atmosenv.2007.06.054. URL `http://www.sciencedirect.com/science/article/pii/S1352231007006036`.

[45] ASHRAE Handbook et al. Hvac applications. *ASHRAE Handbook, Fundamentals*, 2007.

[46] DD Derksen, TJ Bender, DJ Bergstrom, and KS Rezkallah. A study on the effects of wind on the air intake flow rate of a cooling tower: Part 1. wind tunnel study. *Journal of Wind Engineering and Industrial Aerodynamics*, 64(1):47–59, 1996.

[47] Xi Chen, Sijia Du, Yu Zhang, Hongxing Yu, Songwei Li, Huanhuan Peng, Wei Wang, and Wei Zeng. Validation of cfd analysis for rod bundle flow test with vaned spacer grids. *Annals of Nuclear Energy*, 109:370–379, 2017. ISSN 0306-4549. doi: https://doi.org/10.1016/j.anucene.2017.05.055. URL https://www.sciencedirect.com/science/article/pii/S030645491631115X.

[48] Mohammadreza Shirzadi, Parham A. Mirzaei, and Mohammad Naghashzadegan. Improvement of k-epsilon turbulence model for cfd simulation of atmospheric boundary layer around a high-rise building using stochastic optimization and monte carlo sampling technique. *Journal of Wind Engineering and Industrial Aerodynamics*, 171:366–379, 2017. ISSN 0167-6105. doi: https://doi.org/10.1016/j.jweia.2017.10.005. URL https://www.sciencedirect.com/science/article/pii/S016761051730020X.

[49] Anthony D. Santamaria, Nathanial J. Cooper, Maxwell K. Becton, and Jae Wan Park. Effect of channel length on interdigitated flow-field pemfc performance: A computational and experimental study. *International Journal of Hydrogen Energy*, 38(36):16253–16263, 2013. ISSN 0360-3199. doi: https://doi.org/10.1016/j.ijhydene.2013.09.081. URL https://www.sciencedirect.com/science/article/pii/S0360319913023045.

[50] MS Ismail, T Damjanovic, K Hughes, DB Ingham, L Ma, M Pourkashanian, and M Rosli. Through-plane permeability for untreated and ptfe-treated gas diffusion layers in proton exchange membrane fuel cells. *Journal of fuel cell science and technology*, 7 (5), 2010.

[51] MS Ismail, T Damjanovic, DB Ingham, L Ma, and M Pourkashanian. Effect of polytetrafluoroethylene-treatment and microporous layer-coating on the in-plane permeability of gas diffusion layers used in proton exchange membrane fuel cells. *Journal of Power Sources*, 195(19):6619–6628, 2010.

[52] Prafful Mangal, Lalit M Pant, Nicholas Carrigy, Mark Dumontier, Valentin Zingan, Sushanta Mitra, and Marc Secanell. Experimental study of mass transport in pemfcs: Through plane permeability and molecular diffusivity in gdls. *Electrochimica Acta*, 167: 160–171, 2015.

[53] Hao Xu. *Experimental measurement of mass transport parameters of gas diffusion layer and catalyst layer in PEM fuel cell*. Master's thesis, University of Alberta, 2019.

[54] Alan S Foust, Leonard A Wenzel, Curtis W Clump, Louis Maus, and L Bryce Andersen. *Principles of unit operations*. John Wiley & Sons, 2008.

Appendices

Appendix A

Linearization and weak formulation

Similar to the fluid flow equations, the advection-diffusion equations are linearized and then multiplied with a test function and then integrated over the domain, Ω.

$$
\begin{aligned}
&-\int_\Omega u_v(\boldsymbol{v}\cdot\nabla\rho\delta\omega_{\boldsymbol{v}})\,d\Omega-\int_\Omega u_v(\rho\nabla\cdot\boldsymbol{v}\delta\omega_{\boldsymbol{v}})\,d\Omega-\int_\Omega u_v(\rho\boldsymbol{v}\cdot\nabla\delta\omega_{\boldsymbol{v}})\,d\Omega\\
&+\int_\Omega u_v(\mathcal{D}_{eff}\nabla\rho\cdot\nabla\delta\omega_{\boldsymbol{v}})\,d\Omega\\
&-\int_\Omega\nabla u_v\cdot(\rho\mathcal{D}_{eff}\nabla\delta\omega_{\boldsymbol{v}})\,d\Omega+\oint_\Gamma\boldsymbol{n}\cdot(u_v\rho\mathcal{D}_{eff}\nabla\delta\omega_{\boldsymbol{v}})\,d\Gamma-\int_\Omega u_vk_v\delta\omega_{\boldsymbol{v}}\,d\Omega=\\
&\quad\int_\Omega u_v(\boldsymbol{v}\cdot\nabla\rho\omega^k_{\boldsymbol{v}})\,d\Omega+\int_\Omega u_v(\rho\nabla\cdot\boldsymbol{v}\omega^k_{\boldsymbol{v}})\,d\Omega+\int_\Omega u_v(\rho\boldsymbol{v}\cdot\nabla\omega^k_{\boldsymbol{v}})\,d\Omega\\
&-\int_\Omega u_v(\mathcal{D}_{eff}\nabla\rho\cdot\nabla\omega^k_{\boldsymbol{v}})\,d\Omega\\
&+\int_\Omega\nabla u_v\cdot(\rho\mathcal{D}_{eff}\nabla\omega^k_{\boldsymbol{v}})\,d\Omega-\oint_\Gamma\boldsymbol{n}\cdot(u_v\rho\mathcal{D}_{eff}\nabla\omega^k_{\boldsymbol{v}})\,d\Gamma-\int_\Omega u_vk_v(\omega^{sat}-\omega^k_{\boldsymbol{v}})\,d\Omega
\end{aligned}
\tag{A.1}
$$

$$
\begin{aligned}
&-\int_\Omega u_t\frac{\partial c_p}{\partial T}T^k(\boldsymbol{v}\cdot\nabla\rho)\delta T\,d\Omega-\int_\Omega u_tc_p(\boldsymbol{v}\cdot\nabla\rho)\delta T\,d\Omega-\int_\Omega u_t\rho\frac{\partial c_p}{\partial T}(\boldsymbol{v}\cdot\nabla T^k)\delta T\,d\Omega\\
&-\int_\Omega u_t\rho c_p(\boldsymbol{v}\cdot\nabla\delta T)\,d\Omega-\int_\Omega\nabla u_t\cdot(\kappa_{eff}\nabla\delta T)\;d\Omega+\oint_\Gamma\boldsymbol{n}\cdot[u_t(\kappa_{eff}\nabla\delta T)]\;d\Gamma\\
&+\int_\Omega u_tk_t\delta T\,d\Omega=\\
&\quad\int_\Omega u_tc_p(\boldsymbol{v}\cdot\delta\rho)T^k\,d\Omega+\int_\Omega u_t\rho c_p(\boldsymbol{v}\cdot\delta T^k)\,d\Omega\\
&+\int_\Omega\nabla u_t\cdot(\kappa_{eff}\nabla T^k)\,d\Omega-\oint_\Gamma\boldsymbol{n}\cdot\left[u_t(\kappa_{eff}\nabla T^k)\right]\;d\Gamma-\int_\Omega u_tk_t(T_w-T^k)\,d\Omega
\end{aligned}
\tag{A.2}
$$

where u_v and u_t are the scalar weight functions multiplied to the mass transport and temperature transport equations respectively. The velocity and density in these equations are obtained from the previous iteration and are considered constant. These transport equations

are coupled in one way i.e., the velocity and density from the fluid flow are utilized to get the vapor and temperature distribution, however, the vapor and temperature distribution are not used to solve the density and velocity field. The variation in the density and velocity is only because of the compressibility and is in no way affected by the vapor and temperature distribution in the tower.

Appendix B

Compressibile and incompressible simulations with fill

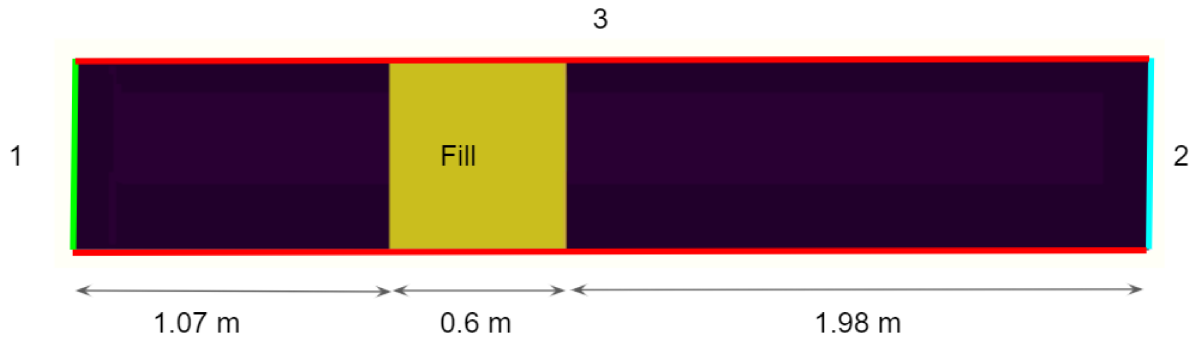

Figure B.1 – Chanel domain with porous media inside and width equal to ESDLab tower. i.e 0.645 m

Table B.1 – Cross flow tower dimensions

Boundary ID	Boundary condition
1	Dirichlet velocity - parabolic profile
2	Dirichlet pressure and normal stress free
3	no-slip

To check the simulations with porous media, test simulations were conducted on the domain shown in Fig. B.1 and the boundary conditions applied are shown in Table B.1. A parabolic velocity profile is applied at the inlet with a maximum velocity equal to 1.80 m/s ($u_{max} = \frac{3}{2}u_{avg}$ where u_{avg} is currently applied at the outlet). In the first set of simulations, the same permeability value is applied in both directions equal to 260 cm^2 and the porosity of media equal to 0.975. Both the compressible and the incompressible solvers resulted in

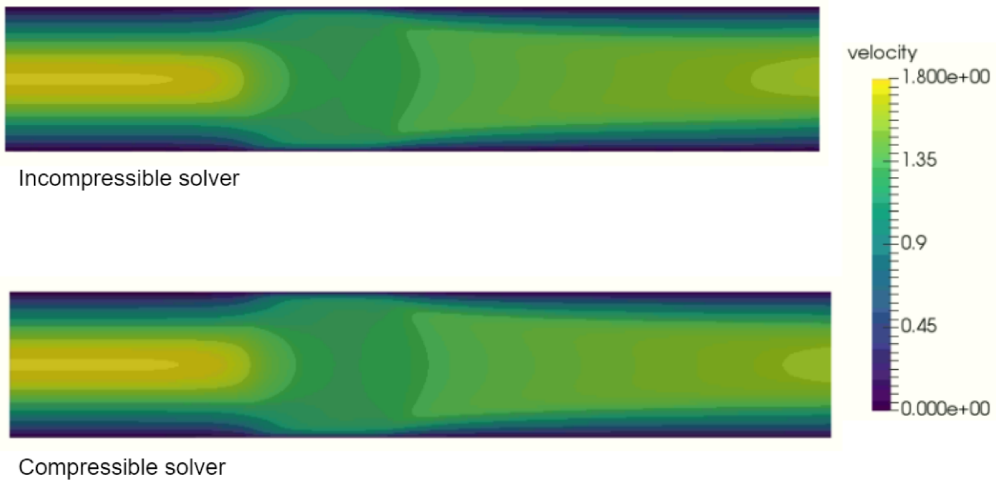

Figure B.2 – Film permeability same in both directions equal to 260 cm^2. Color map same for both solutions

a solution with the absolute residual tolerance on both solvers set to 10^{-6} (Incompressible solver readily resulted in a solution. A compressible solver needs parametric study over velocity for a better initial solution and thereby converged solution). The obtained velocity profiles for both are shown in Fig. B.2.

Both solvers have a similar velocity distribution until the flow reaches the fill, where it becomes uniform due to the same resistance provided in either direction. The compressible flow is observed to have more readily achieved the uniform flow profile than the incompressible solver. For the same conditions, the pressure distribution inside the domain is shown in Fig. B.3. The pressure prediction with the incompressible solver is higher than the analytical value, which is 6.2 Pa, where the compressible solver has a close prediction. Significant pressure loss happens in the fill with compressible solver; however, the incompressible solver has a pressure loss even after the fill zone as shown in Fig. B.4. Please note that X-axis is in m for the incompressible solver, and it is in cm for the compressible solver. As expected, the bulk of the pressure drop is observed across the fill zone with the compressible solver, while the incompressible solver has a significant pressure drop even after the fill zone. The mass flow rate is evaluated for the incompressible solver, and it is observed that it has an inlet flow rate of 0.774093 kg/s and an outlet flow rate of 0.776196 kg/s.

Another simulation where the fill is removed, and just Poiseuille flow is considered, in which case both solvers have predicted the same solution. Even fill with very high permeability in the X-direction, both have similar results; however, when the permeability is decreased, the incompressible solver deviated from the compressible solver due to the pressure drop in the

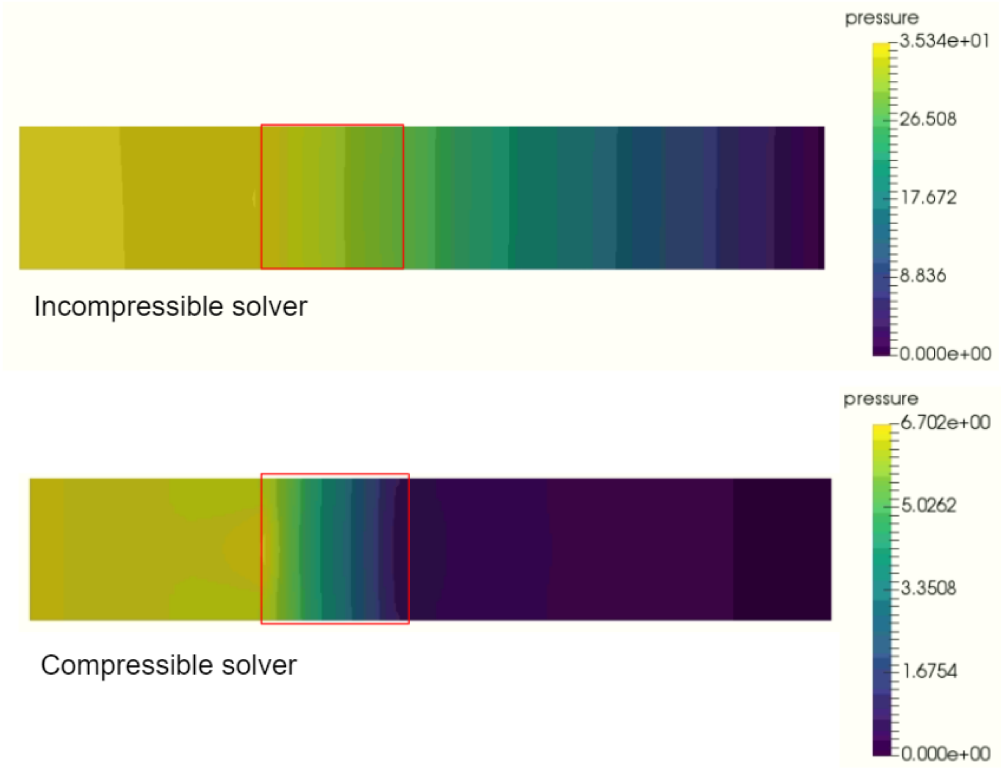

Figure B.3 – Film permeability same in both directions equal to 260 cm^2

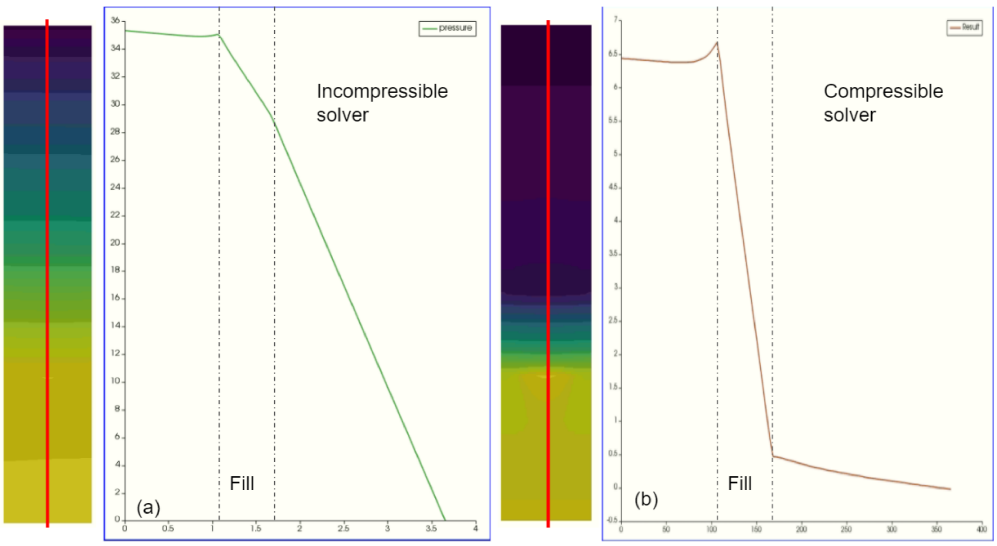

Figure B.4 – Pressure variation along length of the domain (a) Incompressible solver (b) Compressible solver.

channel after the fill.

The incompressible solver can provide results for equal permeability in both directions. However, the convergence is reduced when the permeability value is equal to or less than one cm^2 in at least one direction. The observed pressure prediction is not in accordance with the analytical value. The compressible solver provides the solution for higher Re with anisotropic permeability of the fill with the value lower to the order of 10^{-8} cm^2, which is not the case with the incompressible set of equations. Hence, the compressible set of equations was considered for the simulations in the current study, including a fill.